J/ψ Production in Pb-Pb Collisions with ALICE at the LHC

Dissertation

zur Erlangung des Doktorgrades der Naturwissenschaften

vorgelegt beim Fachbereich Physik
der Johann Wolfgang Goethe-Universität
in Frankfurt am Main

von Julian Book aus Oberursel im Taunus

Frankfurt am Main 2014

(D 30)

Vom Fachbereich Physik der Johann Wolfgang Goethe-Universität
als Dissertation angenommen.

Dekan: Prof. Dr. Rene Reifarth
Gutachter: Prof. Dr. Christoph Blume
                   Prof. Dr. Dr. h.c. Reinhard Stock
Datum der Disputation:

Zusammenfassung

Die Studie von ultra-relativistischen Schwerionenkollisionen verfolgt das Ziel, das Quark-Gluon Plasma (QGP), einen Zustand heißer, hochdichter und stark wechselwirkender Materie, zu erforschen. In diesem Plasma ist das sogenannte *Confinement*, der Einschluss von Partonen (Quarks und Gluonen) in Hadronen, aufgehoben, so dass sich diese quasi-frei in der sogenannten partonischen Phase bewegen können. In der Evolution des Universums hat bis etwa 1 µs nach dem Urknall ein solcher Zustand vorgeherrscht. In Folge der Ausdehnung und der damit verbundenen Abkühlung des Universums trat ein Phasenübergang von der partonischen Phase des QGPs zur hadronischen Phase ein. Seitdem sind die Quarks und Gluonen zu Hadronen gebunden und darin eingeschlossen. In Kollisionen von Blei-Blei-Kernen bei der derzeit höchst-möglichen Kollisionsenergie, die in der vorliegenden Arbeit untersucht werden, können nach derzeitigem Verständis, basierend auf bisher gewonnenen experimentellen Hinweisen, ausreichende Energiedichten erreicht werden, die solch einen Phasenübergang von der hadronischen zur partonischen Phase hervorrufen. Die kritische Temperatur für den Übergang zum QGP liegt laut diskreten Gitter-QCD-Berechnungen bei etwa $T_c \approx 155$ MeV. Innerhalb einer Zeitspanne von etwa 10 fm/c ist das System soweit expandiert und abgekühlt, dass die quasi-freien Partonen am Phasenübergang hadronisieren. Diese extrem kurze Lebensdauer erschwert den Nachweis und die Vermessung des Plasmas, was deshalb nur basierend auf den Reaktionsprodukten, nähmlich den entstandenen Hadronen, deren kinematischen Eigenschaften, Korrelationen und Häufigkeiten, erfolgen kann.

Das in der vorliegenden Arbeit untersuchte, seltene Hadron J/ψ bildet sich aus dem schweren *charm* Quark (c) und seinem Antiteilchen ($\bar{\text{c}}$) und zählt zur Gruppe der Charmonia. Charmonia gelten aus mehreren Gründen als vielversprechende Sonden für die Erforschung des Quark-Gluon Plasmas. Die sie bildenden schweren Quark-Antiquark-Paare werden bei den ersten, besonders harten Stößen der Blei-Kerne erzeugt, welche somit die gesamte nachfolgende Evolution des entstehenden Mediums durchlaufen. Die Bildung und der Zerfall von Charmonia kann daher durch das im Verlauf der Kollision entstehende Medium beeinflusst werden und die Messung von Charmonia bzw. ihrer

Zerfallsprodukte erlaubt somit Rückschlüsse auf die Eigenschaften des Mediums. Analog zur Debye-Abschirmung in der Elektrodynamik können die Farbladungen der quasifreien Quarks und Gluonen in einem Quark-Gluon Plasma das Bindungspotential der Charmonia schwächen und bei hinreichender Temperatur des Mediums auch ganz lösen. Die verschiedenen Zustände der Charmonia haben unterschiedliche Bindungsenergien und Schmelztemperaturen, die in Gitter-QCD-Rechnungen theoretisch bestimmt werden können. Das am stärksten gebundene System eines Charm- und eines Anti-Charm-Quarks ist das in dieser Arbeit untersuchte J/ψ. Massereiche Zustände können Kaskadenartig unter Bildung von J/ψ erfallen. Erfolgt jedoch eine Dissoziation von einem oder mehreren Charmonia-Zuständen durch das entstehende Medium, so dass deren Zerfall in J/ψ ausbleibt, erfolgt eine Unterdrückung der J/ψ-Produktion im Vergleich zu Proton-Proton-Kollisionen, bei denen keine Plasmaausbildung erwartet wird. Aber auch bereits in Messungen von Stößen von Protonen mit schweren Kernen (p-A) ist eine Unterdrückung des J/ψ Signals relativ zu Proton-Proton-Reaktionen beobachtet worden. Die in solchen Kollisionen relevanten Effekte sogenannter kalter Kernmaterie führen auch zu einer Unterdrückung der Charmonia-Produktion und müssen entsprechend in der Interpretation der Messungen in Pb-Pb-Stößen berücksichtigt werden. Laut theoretischen Vorhersagen kann bei der hier untersuchten Kollisionsenergie erstmals in signifikanter Ausprägung ein Effekt beobachtet werden, welcher der Unterdrückung der J/ψ Produktion im Quark-Gluon Plasma entgegenwirkt und diese sogar übertrifft. Dieser Produktionsmechanismus trägt den Namen „Rekombination" bzw. „Regeneration" und beschreibt die Bildung von J/ψ-Mesonen durch Koaleszenz freier Charm-Quarks bei ausreichender c$\bar{\text{c}}$-Dichte im QGP. In Transport-Modellen werden die Effekte der Dissoziation und der Koaleszenz durch Wirkungsquerschnitte realisiert, welche über den gesamten Ablauf der Schwerionenkollision modelliert werden, während in dem Statitischen-Hadronisierungs-Modell alle Teilchenmultiplizitäten erst beim Ausfrieren festgelegt werden. Die Ergebnisse beider Modelltypen sind stark mit der totalen Charm-Produktion korreliert, welche bei der hier untersuchten Kollisionsenergie noch nicht gemessen werden konnte und daher großen Spielraum in der Bewertung der Modelle zulässt.

Die Untersuchung von Schwerionenkollisionen bei einer Schwerpunktsenergie von $\sqrt{s_{\text{NN}}} = 2,76$ TeV erfolgte mit den aufgezeichneten Daten des ALICE Experiment, welches am CERN-LHC positioniert ist. Das Experiment wurde insbesondere für die Untersuchung des Quark-Gluon Plasmas in Blei-Blei-Reaktionen entworfen. Die hohen Anforderungen an die Genauigkeit der Impulsmessung und Identifikation der Teilchensorten bei besonders hohen Spurdichten waren bestimmende Aspekte beim Design von ALICE.

Das Experiment besteht aus zahlreichen Detektoren mit unterschiedlichen Aufgaben (Teilchennachweis, Spurvermessung, Online-Selektion), welche in verschiedenen Rapiditätsbereichen positioniert sind. Die Rekonstruktion des J/ψ-Zerfalls in Elektron und Positron, der in dieser Arbeit erforscht wird, erfolgt über das Inner Tracking System (ITS) und die Time-Projection Chamber (TPC), welche den Messbereich des J/ψ bei zentralen Rapiditäten ($|y| < 0,8$) festlegen. Die Teilchenidentifikation beruht auf dem spezifischen Energieverlust ($\mathrm{d}E/\mathrm{d}x$) der geladenen Teilchen, welche das Detektorgas der TPC entlang ihrer Trajektorie ionisieren. Die ausgelösten Elektronen driften mit konstanter Geschwindigkeit entlang der Feldlinien des angelegten elektrischen Feldes und werden an den Endkappen der TPC ausgelesen. Zusätzlich erfahren die geladenen Teilchen bei ihrer Bewegung eine Ablenkung durch das magnetische Feld, wodurch deren Spuren gekrümmt werden und eine Impulsmessung durchgeführt werden kann. Die Qualität der $\mathrm{d}E/\mathrm{d}x$- und Impulsmessung hängt dabei wesentlich von der Anzahl der gemessenen Spurpunkte ab und erfordet eine gründliche Kalibrierung und Korrektur der schwankenden Detektorbedingungen. Mit Hilfe des $\mathrm{d}E/\mathrm{d}x$-Signals können Elektron-Kandidaten selektiert werden, und durch die präzise Ortauflösung des ITS, einem System aus sechs Lagen Silizium-Detektoren, kann sowohl die Impulsmessung verbessert als auch der Teilchenursprung präzise bestimmt werden. Da J/ψ-Mesonen extrem nah am rekonstruierten Primärvertex der Kollision zerfallen, führt eine Selektion von Spuren mit Signalen in der dem Primärvertex nächstgelegenen ersten ITS-Lage zur deutlichen Reduzierung von Elektron-Kandiaten aus Konversionen oder sekundären Zerfällen anderer Teilchensorten. Eine weitere Möglichkeit, die Kontamination (durch größtenteils Pionen) der ausgewählten Kandidaten zu verringern, ist durch den Transition Radiation Detector (TRD) gegeben, welcher primär für die Trennung von Elektronen und Pionensignalen entworfen wurde. Bei diesem Detektor wird der Effekt der Übergangstrahlung von geladenen Teilchen beim Durchqueren von Übergängen zwischen Materialien mit unterschiedlichen Permittivitäten ausgenutzt, um Teilchen ähnlicher Masse zu unterscheiden. Zur Zeit der Datennahme waren jedoch erst sieben bzw. zehn der insgesamt und nunmehr vollzähligen 18 Detektormodule installiert. Um die Akzeptanz der Messung nicht zu beschränken wurde die Analyse daher ohne den TRD durchgeführt. In zuünftigen Strahlzeiten des LHC wird der Transition Radiation Detector aber zu einer Verbesserung der Elektronen-Identifikation und Impulsauflösung bei hohen Transversalimpulsen beitragen können. Zusätzlich bietet ein TRD-Trigger die Möglichkeit Reaktionen, welche Elektronen aus Charmonia-Zerfällen enthalten, mit erhöter Wahrscheinlichkeit online auszuwählen, um besonders viele derartige Ereignisse aufzeichnen zu können.

Für die Verwendung des TRD in physikalischen Analysen ist eine stetige Kalibration

der Detektormodule und dessen Kontrolle notwendig. Im Rahmen dieser Arbeit wurde das vorhandene Kalibrationsschema um die Überprüfung der Datenqualität in den Auslesekammern erweitert. Die Beurteilung kann sowohl online als auch nach Beendigung der Datennahme erfolgen und basiert auf der mittleren Anzahl der zugewiesenen Ladungsansammlungen der Spurstücke jeder Auslesekammer. Des Weiteren wurden die Kalibrationsparameter der Driftgeschwindigkeit, der Signalverstärkung und der Verzerrung durch $E \times B$-Effekte in die Bewertung eingebunden. Um die Qualität der Kalibration und Rekonstruktion der TRD-Daten zu überpüfen, sowie deren zeitliche Veränderungen zu verfolgen, wurde eine nahezu vollautomatische Prozedur entwickelt, welche die einzelnen Schritte der Datenaufbereitung überwacht und darstellt.

In dieser Arbeit wurde der Zerfall des J/ψ in Elektron und Positron im Rapiditätsbereich $|y| < 0,8$ untersucht. ALICE ist derzeit das einzige Experiment am LHC, welches diese Messung bei zentralen Rapidiäten herab bis zu Transversalimpulsen $p_\mathrm{T} = 0$ durchführen kann. Die Auswertung der experimentellen und simulierten Daten erfolgte innerhalb einer gemeinsamen Softwareumgebung (dem *dielectron package*), welches von der ALICE-J/$\psi \to$ e$^+$e$^-$-Analysegruppe und zum Teil im Rahmen dieser Arbeit entwickelt wurde und innerhalb des ALICE Analyse Systems agiert. Alle technischen Komponenten, Definitionen und Routinen sind in einem von allen Elektron-Positron-Studien verwendeten „Analyse-Task" zusammengefasst. Das *dielectron package* bietet sowohl die Infrastruktur für den Datentransfer und den Output, als auch verschiedene Module zur Selektion von Triggern, Ereignissen, Spuren und deren Kombinationen. Weiterhin, wurden verschiedenste Methoden zur Bestimmung des Untergrunds und des Signals oder zur Berechnung von Effizienzen und Anwendung von Korrekturen entwickelt, welche einer effektiven Auswertung dienen.

Zunächst wurde der Nukleare Modifikationsfaktor (R_AA) für inklusive J/ψ-Produktion für verschiedene Zentralitäten von Blei-Blei-Kollisionen (Pb-Pb) bei einer Schwerpunktsenergie von $\sqrt{s_\mathrm{NN}} = 2,76$ TeV bestimmt. Dieser Faktor gibt das Verhältnis zwischen Kern-Kern (A-A) und Proton-Proton-Kollisionen (pp), skaliert mit der Anzahl binärer Nukleon-Nukleon-Stöße, wieder und ist dadurch sensitiv auf Effekte und Eigenschaften kalter und heißer Kernmaterie. Im Zentralitätsbereich $0 - 90\%$ konnte keine signifikante Änderung von R_AA gemessen werden, jedoch gibt es im Vergleich zu Messungen der PHENIX-Kollaboration bei geringer Schwerpunktsenergie eine deutlich geringere J/ψ Unterdrückung. Dies deutet auf eine Zunahme der J/ψ-Produktion aufgrund der höheren Kollisionsenergien hin. Ein Vergleich der vorliegenden Ergebnisse mit den Ergebnissen, die bei Vorwärtsrapidität ($2,5 < y < 4$) gemessen wurden, zeigt eine schwächere J/ψ

Unterdrückung bei mittleren Rapiditäten, welches im Szenario der J/ψ Rekombination durch eine erhöhte Charm-Quark-Dichte begründet werden kann. Aufgrund der großen Unsicherheit des pp-Wirkungsquerschnittes in der Berechnung von R_{AA} und der zurzeit noch nicht gemessenen, totalen Charm-Produktion, welche für die verschiedenen Modell-Vorhersagen essentiell ist, wird kein Modell gegenüber den anderen von den Daten bevorzugt. Anzumerken ist jedoch, dass alle Modelle, welche den Rekombinationsmechanismus enthalten, den in den Daten erkennbaren Trend beschreiben können. Einige Teile dieser Arbeit konnten zur ersten Publikation der Messung des J/ψ-Zerfalls in e$^+$ e$^-$ in Pb-Pb Kollisionen durch die ALICE Kollaboration beitragen. Die Grundlagen der J/ψ-Rekonstruktion und Resultate dieser Studie werden in Kapitel 4 vorgestellt und ausführlich diskutiert.

Im zweiten Teil der vorliegenden Arbeit wurde die Abhängigkeit der J/ψ-Produktion in Pb-Pb-Kollisionen vom Transversalimpuls untersucht. Laut theoretischen Vorhersagen ist gerade bei geringen Transversalimpulsen eine besonders deutliche Unterscheidung zwischen J/ψ-Dissoziation und Rekombination möglich, da dort der geringere relative Impulsunterschied zwischen den Charm-Quarks den Prozess der Koaleszenz begünstigt. Die Anzahl an aufgezeichneten Pb-Pb-Kollisionen erlaubt eine Berechnung von R_{AA} in zwei p_{T}-Intervallen. Wegen der fehlenden Referenzmessung für die J/ψ-Produktion bei $|y| < 0,8$ als Funktion des Transversalimpulses in Proton-Proton-Kollisionen bei $\sqrt{s} = 2,76$ TeV, wurde eine Interpolation basierend auf J/ψ-Messungen bei verschiedenen Energien durch die PHENIX-, CDF- und ALICE-Kollaborationen entwickelt. Mit Hilfe des mittleren Transversalimpulses ($\langle p_{\mathrm{T}} \rangle$) sowie des Produktions-Wirkungsquerschnittes ($\mathrm{d}\sigma/\mathrm{d}y$) wurde ein universales Verhalten der Transversalimpulsverteilung inklusiver J/ψ gefunden, welches die Form des Transversalimpulsspektrums ($\mathrm{d}^2\sigma/\mathrm{d}y\mathrm{d}p_{\mathrm{T}}$) festlegt und eine Berechnung von R_{AA} als Funktion von p_{T} zulässt. Die größte Unsicherheit dieser Konstruktion ergibt sich aus der Normierung durch $\mathrm{d}\sigma/\mathrm{d}y$. Die in dieser Arbeit durchgeführte Messung zeigt eine Erhöhung von R_{AA} hin zu geringen p_{T}, wie durch Transport-Modelle im Rahmen von Rekombination vorhergesagt wurde. Weiterhin wird ein deutlicher Unterschied der J/ψ-Produktion bei geringen Transversalimpulsen im Vergleich zu den Ergebnissen der PHENIX- und STAR-Kollaborationen beobachtet, was als weiteres Indiz für eine Erhöhung der J/ψ Produktion durch den Effekt der Rekombination interpretiert werden kann. Im weiteren Verlauf der Transversalimpuls-Studie, welche in Kapitel 5 der vorliegenden Arbeit beschrieben ist, wurde das erste ($\langle p_{\mathrm{T}} \rangle$) und zweite Moment ($\langle p_{\mathrm{T}}^2 \rangle$) der p_{T}-Verteilung durch Fits im vollständig korrigierten invarianten Massenspektrum der $\langle p_{\mathrm{T}} \rangle$- und $\langle p_{\mathrm{T}}^2 \rangle$-Verteilungen ermittelt. Für drei verschiedene Zentralitätsklassen konnten Resultate ermittelt werden. Diese zeigen keine signifikante Systemgrößenabhängigkeit.

Aus dem Vergleich der Resultate zu den deutlichen größeren $\langle p_\mathrm{T} \rangle$- und $\langle p_\mathrm{T}^2 \rangle$-Werten, die aus der pp-Interpolation gewonnen wurden, kann entweder eine Reduzierung der J/ψ-Produktion mit hohem Transversalimpuls oder eine Erhöhung im Bereich niedriger J/ψ-p_T abgeleitet werden. Transport-Modelle sind in qualitativer Übereinstimmung mit den Resultaten dieser Arbeit, zeigen jedoch systematisch größere Werte, was auf eine stärkere Beteiligung von c$\bar{\mathrm{c}}$-Koaleszenz in den Kollisionsdaten verglichen zur Theorie hinweisen könnte. Die Ergebnisse dieser Studien sind gegenwärtig auf dem Weg der Publikation.

Eine deutliche Signatur für c$\bar{\mathrm{c}}$-Rekombination ist durch den Fluss der J/ψ-Mesonen vorhergesagt. J/ψ-Mesonen, welche in den ersten, harten Nukleon-Nukleon-Stößen in Schwerionenkollisionen erzeugt werden, besitzen keine Information über den geometrischen Anfangszustand der Kollision. Der elliptische Fluss (v_2) beschreibt die Richtungsabhängigkeit der Teilchen im Impulsraum einer typischerweise halb-zentralen Kern-Kern-Kollision, welche in den Ortsraum transformiert werden kann.

Teilchen, welche im Verlauf der Kollision entstehen und zahlreiche Wechselwirkungen vollführen, erfahren eine Anpassung vorzugsweise in Richtung der Reaktionebene. Während J/ψ-Mesonen aus dem Anfangszustand nur ein geringes v_2 aufgrund des Pfadlängen-abhängigen Energieverlustes erfahren können, erben J/ψ aus c$\bar{\mathrm{c}}$-Koaleszenz den v_2 des Charm- und Anti-Charm-Quarks, welches dem v_2 geladener Hadronen entspricht. In Kapitel 6 dieser Arbeit wurde eine Machbarkeitsstudie für die Signalbestimmung des elliptischen Flusses durchgeführt. Ein elliptischer Fluss des J/ψ konnte über zwei unterschiedliche Methoden und mit Hilfe verschiedener Detektoren zur Bestimmung der Reaktionsebene für halb-zentrale Pb-Pb Kollisionen im Bereich $2 < p_\mathrm{T} < 6$ GeV/c ermittelt werden. In diesem Bereich wird die höchste Signifikanz für ein positives v_2 erwartet. Im Ergebnis der Analyse ist der elliptische Fluss konsistent mit Null. Die Messung ist jedoch mit einer großen statistischen Unsicherheit behaftet und erlaubt daher keine qualitative Aussage über den elliptischen Fluss des J/ψ. Im Folgenden wurde deshalb die integrierte Luminosität für eine Messung mit ähnlicher Präzision zu der veröffentlichten Messung durch ALICE in $2,5 < y < 4$ abgeschätzt. Bei leicht verbesserter Leistungsfähigkeit der TPC und basierend auf den Ergebnissen der aktuellen Daten kann eine qualitative Messung des v_2 des J/ψ bereits bei einer integrierten Luminosität von $\mathscr{L}_{int} = 15$ µb^{-1}, etwa dem Dreifachen der bislang aufgenommenen Pb-Pb-Kollisionen, erfolgen. Mit einer solchen Messung könnte der Mechanismus der J/ψ-Produktion, etwa durch Rekombination, präzise studiert werden.

Contents

Contents 1

Chapter 1.

Introduction

In 1969, deep-inelastic scatterings of electron and nucleons revealed the inner structure of the nucleon [1,2], that was interpreted as a scattering of an electron with a point-like elementary particle inside the nucleon [3]. The gauge theory for strong interactions, the Quantum Chromodynamics (QCD), and the static quark model proposed by Gell-Mann and Zweig [4,5] assigned the *quarks* and *antiquarks* to these elementary particles. In total six different types of quarks (up u, down d, strange s, charm c, bottom b, top t) and their antiquarks have been identified through experimental measurements in the following three decades. The evidence for antiquarks in nucleons was demonstrated by the Drell-Yan process ($q\bar{q} \rightarrow \gamma^* \rightarrow \ell^+\ell^-$) in nucleon-nucleon scattering [6]. In nature these quark and antiquarks seem to exist only as bound states of quark-antiquark pairs (mesons) or triplets of quarks/antiquarks (baryons). They are coupled through the strong force mediated via *gluons* that, in contrast to the exchange particle γ of the electromagnetic force, can interact with themselves. As a consequence, this leads to a small coupling between quarks and gluons in the case of large momentum transfers or small distances, the so-called *asymptotic freedom*, and increases for large distances or small momentum transfers, leading to the behaviour of *confined* particles. Due to the weak coupling of quarks and gluons, it is possible to calculate interactions with a large momentum transfer with pertubative QCD. In Lattice QCD, the non-pertubative part of QCD, resp. large distance interactions, can be calculated by computational techniques resulting in a phase transition from the confined medium to a hadron gas at a temperature $T_c \approx 155$ MeV [7,8], as depicted in Fig. 1.1.

In order to reach conditions where quarks and gluons behave essentially free, either large densities or high energies are necessary. In [9,10] it is argued that these conditions
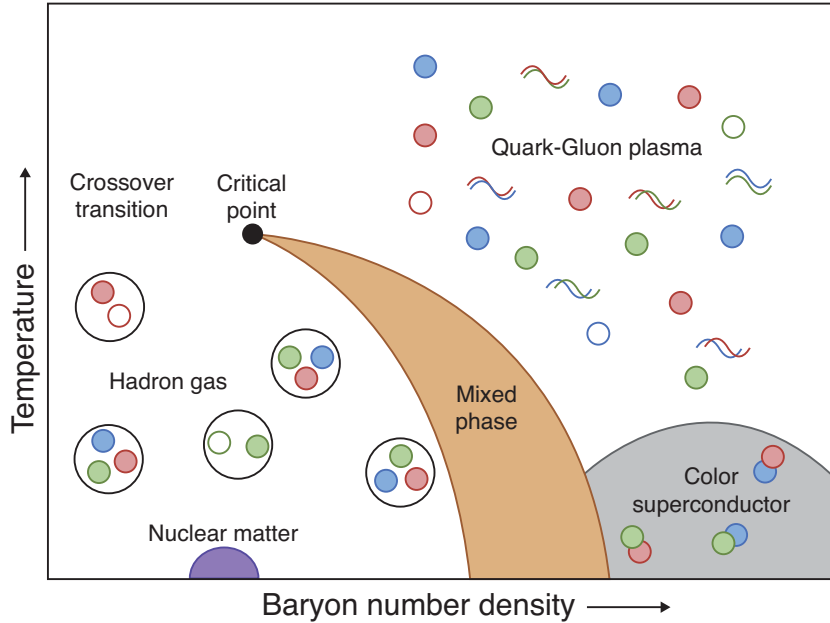
Figure 1.1.: A sketch of the phase diagram of strongly interacting matter.

are satisfied in high-energy nucleus-nucleus interactions, leading to the formation of a collective state of strongly interacting matter, the Quark-Gluon Plasma (QGP).

Fig. 1.2 illustrates the space-time evolution of a heavy-ion collision with the subsequent stages of the collision: (i) two nuclei with almost the speed of light move towards on each other (ii) at the initial stage $\tau = 0$, the first hard-scatterings with high momentum transfer happen and the nuclei start passing through each other (iii) multiple interactions and the production of the bulk of particles lead to a medium in thermal equilibrium (*fireball*), the QGP. (iv) the system expands and cools down until the phase boundary is crossed and hadronization happens (*chemical freeze-out*). (v) no more collisions between the hadrons occur and their kinematics is fixed when the system passes the *thermal freeze-out* boundary.

Due to the confinement, only hadrons as final states can be observed experimentally. The study of the QGP can only be performed indirectly by the distribution of the final hadrons and their decay products. Several different tools and signatures for the existence of the QGP can be studied. They can be categorized into (i) bulk-properties (spectra, collective flow, fluctuations, correlations and anisotropy flow) that are affected by the phase transition and characterize the medium properties (wquation of state, speed of sound, shear viscosity) (ii) jets and high-p_T particles that probe the medium via energy-loss and result in modifications or quenching of the particle momenta/energy,
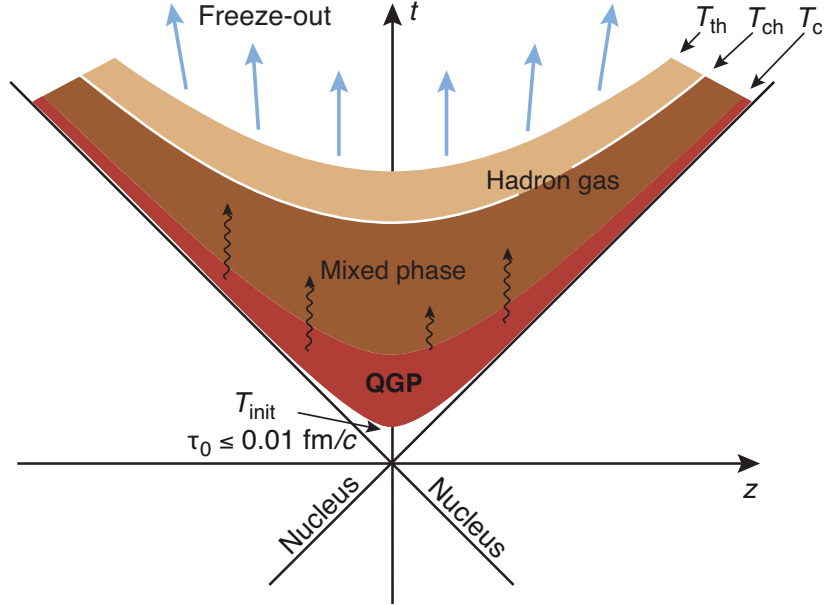
Figure 1.2.: Space-time evolution of a heavy-ion collision with the subsequent stages of the collisions.

depending on path-length and the evolution of the medium. (iii) electromagnetic probes (γ,ℓ) that do not interact strongly with the medium and thus can provide information about the entire history of the collision. (iv) the behaviour of heavy-flavour particles in a deconfined medium can result into production suppression or enhancement relative to the production in absence of a QGP. The observables of J/ψ production are part of this thesis and introduced in detail in the next chapter.

Chapter 2.

Charmonia
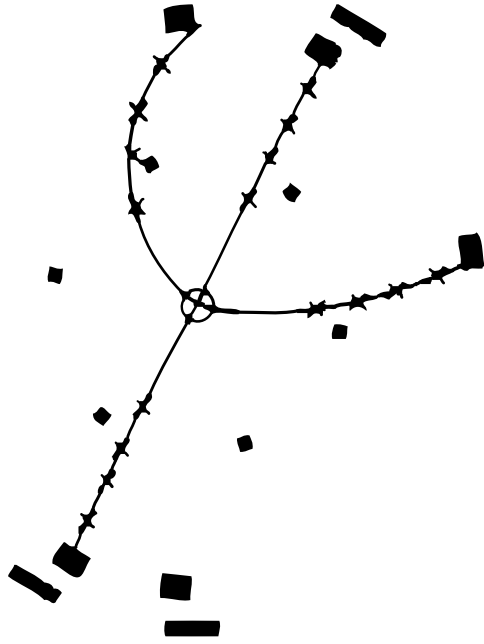
The discovery of the J/ψ meson [11, 12], a bound state of a charm quark (c) and its antiquark ($\bar{c}$) with photon quantum numbers $J^{PC} = 1^{--}$ [13], in 1974 was the first time when heavy quarks showed up experimentally. Their existence was predicted in [14] in 1970 within the GIM[1] model. Charm quarks can also bind with normal light quarks, such as u, d, s, to so-called open charm mesons (D). In contrast to light, non-strange hadrons, the masses of bound c$\bar{c}$ states (*hidden* charm) are largely determined by the bare charm mass $m_c = 1.27$ GeV/c^2 and non from the interaction energy of their constituent quarks. This implies that many properties of the c$\bar{c}$ states, e.g. the average spatial size r_0, can easily be calculated using the non-relativistic potential theory [15, 16]. Besides the initially discovered vector ground state J/ψ(1S), there a four other quasi stable bound states of different quantum numbers, the scalar η_c(1S), the three 1P states χ_c (scalar,vector and tensor) and the vector state ψ(2S). They are stable under strong interaction, meaning decays into open charm are forbidden, because their masses are below than that of two open charm mesons, $m_{c\bar{c}} < 2m_D = 3.739$ GeV/c^2. As a consequence a decay of the c$\bar{c}$ state with continuous quark lines in the OZI[2] picture is not preferred, resulting in the long life times ($\tau = \hbar/\Gamma$) and a more probable decay into a pair of leptons via the electromagnetic force. In [18], the first observation of the radiative J/ψ decay, J/$\psi \to e^+e^-\gamma$, was reported. In contrast to the well-known 'detector' or 'external' bremsstrahlung, the photon is not emitted from real electrons at a later stage due to the environment (magnetic or atomic field), but it comes directly from the decay vertex, hence from a virtual electron ('intrinsic' or 'internal' bremsstrahlung). The effect on the invariant mass of charmonia is studied in

---

[1]GIM stands for the authors Glashow, Iliopoulos and Mainani

[2]Since gluons carry color charge and hadrons are neutral, interactions with one single gluon connecting the initial and final states are suppressed. The OZI rule was proposed and generalized by Zweig, Iizuka and Okubo [17].

[19]. The invariant mass of the stable $c\bar{c}$ states, their binding energies $\Delta E = m_{D\bar{D}} - m_{c\bar{c}}$, quantum numbers and spatial sizes are listed in Tab. 2.1.

$c\bar{c}$ state		J/ψ(1S)	χ_{c0}(1P)	χ_{c1}(1P)	χ_{c2}(1P)	ψ(2S)
J^{PC}		1^{--}	0^{++}	1^{++}	2^{++}	1^{--}
Mass m	(MeV/c^2)	3096.9	3414.8	3510.7	3556.2	3686.1
Decay Width Γ_{tot}	(MeV/c^2)	0.093	10.3	0.86	1.97	0.303
Branching Ratio $\Gamma_{e^+e^-}/\Gamma_{\text{tot}}$	(%)	5.97	-	-	-	0.78
Feeddown $\Gamma_{J/\psi+X}/\Gamma_{\text{tot}}$	(%)	-	1.3	34.8	< 22.1	60.3
Binding Energy ΔE	(MeV)	642	324	228	183	53
Average Radius r_0	(fm)	0.43-0.50		0.67-0.72		0.87-0.90
Formation Time τ_f	(fm/c)	0.15		0.28		0.39

Table 2.1.: Stable $c\bar{c}$ states and their quantities [20]. Radii are taken from [16, 21] and formation times are calculated accordingly.

In particular the J/ψ(1S) is very tightly bound and of very small spatial size, compared to typical hadrons. $c\bar{c}$ pairs can be created either via *hadroproduction* through a hard nucleon-nucleon collision in the first stage of the interaction, or they can occur in electromagnetic interactions of the two colliding nuclei via a virtual photon γ^* (*photoproduction*). Since the mass of the $c\bar{c}$ states are well above the typical medium temperature, they cannot be produced thermally. Due to their long life times and their very early production the $c\bar{c}$ resonances are excellent probes for all stages of the collisons and any medium created in the collisions will not affect the decay products, but the bound states themselves. In the hadronic charm production, the formed $c\bar{c}$ in most cases is a color octet state, carrying color charge, and then neutralizes by interaction with the surrounding color field to physical resonances (J/ψ,χ_c,...) within a time scale of $\tau \sim \, \geq 1/\sqrt{2m_c \Lambda_{\text{QCD}}} = 0.25$ fm/c [23], where $\Lambda_{\text{QCD}} \approx 200$ MeV/c. At lower energies the dominant process for $c\bar{c}$ production is quark-antiquark annihilation, see Fig. 2.1c, while at higher collision energy the $c\bar{c}$ is formed via gluon fusion processes, e.g. Figs. 2.1a and 2.1b, since the probability for gluons g in the parton distribution functions (PDFs) at lower Bjorken $x_B = Q^2/2m_{p,n}\nu$ is much larger than for quarks q, for details see [24]. The total amount of inclusive J/ψ produced directly via partonic interactions is about $\approx 65\%$ for centre-of-mass energies up to $\sqrt{s} = 1.8$ TeV. Other charmonia states can feed-down into J/ψ with contributions of $(25 \pm 5)\%$ for χ_c(1P) and $(8.1 \pm 0.3)\%$ for ψ(2S) (world averages according to [25]). Furthermore the inclusive J/ψ production origin can be separated into the prompt and

the non-prompt part. Non-prompt J/ψ mesons are produced via the weak decay of b hadrons into J/ψ + X with a fraction of $f_{\mathrm{B}} = 0.149 \pm 0.037(\mathrm{stat.})^{+0.018}_{-0.027}(\mathrm{syst.})$ of the inclusive J/ψ for $p_{\mathrm{T}} > 1.3$ GeV/c at mid-rapidity [26].

In nuclear collisions the coherent photoproduction of the J/ψ, see Fig. 2.1d, happens through a "photon-gluon fusion" mechanism, where one incoming nucleon acts as a photon source and the other as a target that releases a colorless two-gluon system. This interaction is sensitive to the gluon distribution in the target nucleon in square $(x\mathrm{g}(x, Q^2))^2$, when the vector meson originating from the c$\bar{\mathrm{c}}$ is produced exclusively.

(a) gluon fusion   **(b)** gluon fusion

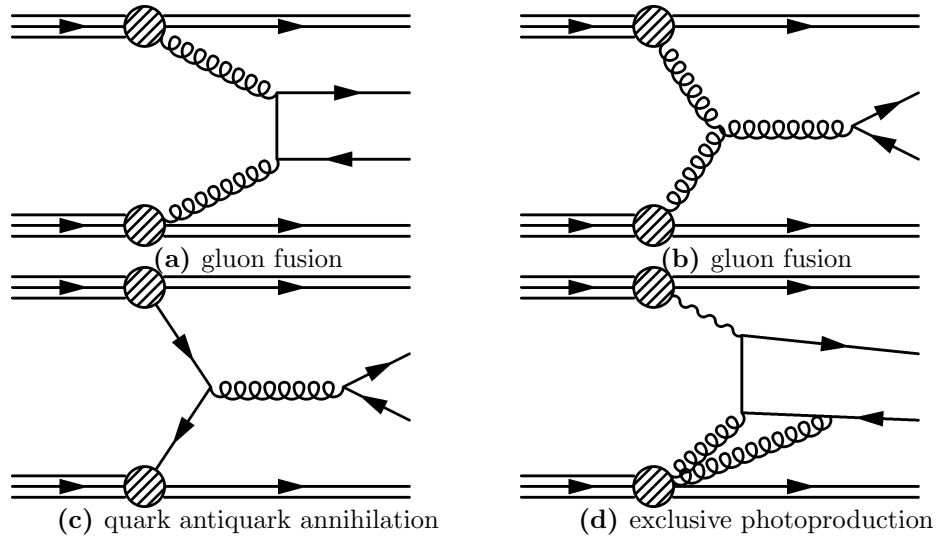**(c)** quark antiquark annihilation   **(d)** exclusive photoproduction

Figure 2.1.: Basic Feynman diagrams for c$\bar{\mathrm{c}}$ production in hadronic collisions, through gluon fusion, quark-antiquark annihilation and photoproduction.

Due to the long lifetimes of the formed bound c$\bar{\mathrm{c}}$ state, compared to that of the QGP (see Tab. 2.2), several interactions can happen. The different effects and their origins are described in the following. They can be categorized into initial and final state effects.

2.1. Initial State Effects

The J/ψ meson was simultaneously discovered in nucleon-nucleus (p-A) collisions through the channel p + Be $\rightarrow \gamma^* \rightarrow$ J/ψ [11] and through e$^+$ + e$^- \rightarrow \gamma^* \rightarrow$ J/ψ [12], where only one single reaction at a well defined center-of-mass energy occurs. In the case of pp collisions at LHC energies a dependency on the underlying event multiplicity was found [37,38]. One interpretation of this result is, that so-called multiple partonic interactions (MPI) [39] can occur in a single collision leading to the observed linear correlation of J/ψ to charged

Accelerator		SPS	RHIC	LHC
$\sqrt{s_{\mathrm{NN}}}$	(GeV)	17.3	200	2760
x_{B}		$(0.7 - 4.9) \times 10^{-1}$	$(1.1 - 2.2) \times 10^{-2}$	$(0.5 - 2.8) \times 10^{-3}$
τ_c	(fm/c)	$(0.2 - 1.1) \times 10^{-1}$	$(3.2 - 6.5) \times 10^{-2}$	$(0.5 - 3.0) \times 10^{-2}$
$\sigma_{c\bar{c}}$	(µb)	-	$148 \pm 15 \pm 19$	-
$\mathrm{d}N_{c\bar{c}}/\mathrm{d}\eta$		0.173	3.4 ± 0.6	-
ϵ_0	(GeV/fm^3)	3.2	5.4 ± 0.6	14
τ_f (QGP)	(fm/c)	6	7	$10 - 11$

Table 2.2.: Characteristic properties of $c\bar{c}$ production in A-A collisions for different energies and experiments. Bjorken x_{B} values correspond to mid-rapidity J/ψ production at $p_{\mathrm{T}} = 0$ (calculated for the acceptances of NA50, PHENIX and ALICE according to [27]). The initial Bjorken energy density $\epsilon_0 = (\mathrm{d}E_T/\mathrm{d}\eta)/(\tau A_T)$ [28] for the 5% most central collisions are taken from [29–31]. The QGP lifetimes τ_f [32–34] are based on the π HBT radii R_{long} and scale with $\langle \mathrm{d}N_{\mathrm{ch}}/\mathrm{d}\eta \rangle^{1/3}$. The number of produced $c\bar{c}$ pairs per unit of rapidity in the 10% most central collisions are taken from [35, 36].

particle production. The measurements of J/ψ pair production at the LHC [40, 41] and at the Tevatron [42] further support this scenario. The transversal distribution of quarks and gluons is described by so-called generalized partion distributions functions (GPD) and depends strongly on the impact parameter [43, 44]. Due to this, the probability for MPI in pp collisions increases towards smaller impact parameters. Thus, already in pp collisions at high centre-of-mass energy the J/ψ production is affected by changes of the parton density and might be further modified by quantum-mechanical density fluctuations at the corresponding small Bjorken x_{B} of the gluons. In the framework of parton saturation or string interaction models [45] it is argued that the rise of J/ψ production with charged particle multiplicity may be a consequence of the formation of a high density medium.

In general, the impact of additional normal nuclear matter, such as in hadron-nucleus interactions, is associated to initial state effects. The presence of other nucleons in a nucleus can modify the PDFs, see Fig. 2.2. The probed x_{B} range depends on the centre-of-mass energy per nucleon pair $\sqrt{s_{\mathrm{NN}}}$, the rapidity range covered by the measurement and the momentum of the bound $c\bar{c}$ state. Calculations are done according to Eq. (2.1) and their values for A-A collisions are quoted in Tab. 2.2.

$$x_{\text{B}} = \frac{m_{\text{J}/\psi}}{\sqrt{s_{\text{NN}}}} \exp(\pm y_{\text{J}/\psi}) \quad \text{(for symmetric collisions and p}_{\text{T}} = 0\text{)} \qquad (2.1)$$

For lower (higher) x_{B}, the PDF is suppressed (enhanced) inside the nucleus. This effect is called shadowing, respective anti-shadowing, and increases with collision energy. In addition to the modification of the parton density, quarks and gluons can experience multiple scatterings with the target nucleons while traversing the nucleus before the hard scattering, i.e. the Cronin effect [46]. This might shift the transverse momentum of the J/ψ to lower values and would result in a decrease of the $\langle p_{\text{T}} \rangle$ w.r.t. pp collisions. The second moment of the p_{T} distribution, $\langle p_{\text{T}}^2 \rangle$, would then rise monotonically, since it is a function of the history of the projectile gluon and therefore depends on the traveling length in the nuclei [47]; this effect it called p_{T}-broadening. Both initial state effects are intrinsic to the nuclear target.

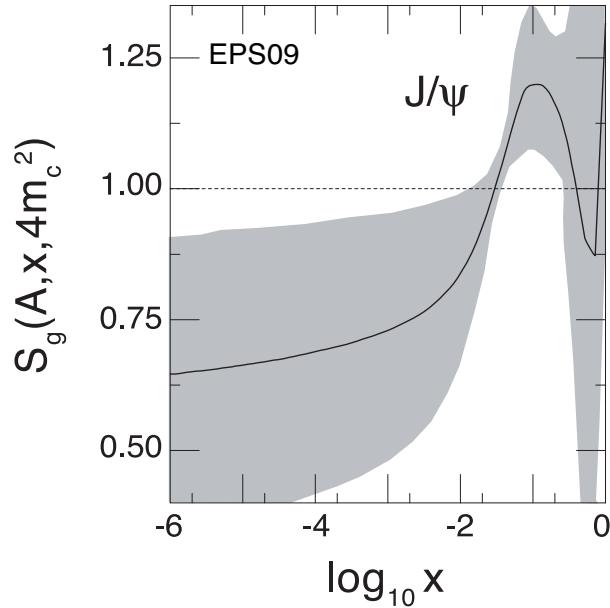**Figure 2.2.:** The gluon distribution function of a nucleon in a Pb nucleus normalized to that of a free nucleon as a function of x_{B} for EPS09 calculations [48, 49]

2.2. Final State Effects

Any effects happening to the pre-resonant stage, bound $c\bar{c}$ state or to the finally formed charmonium after the first hard interactions of the collisions are associated to final state

effects. They can be divided into so-called Cold-Nuclear-Matter effects (CNM)[3], where no formation of a hot and dense matter plays a role, and QGP-induced effects. The former should be determined from p-A collisions and serve as baseline for the interpretation of the quarkonium production in heavy-ion collisions.

2.2.1. Cold-Nuclear-Matter Effects

The produced $c\bar{c}$ pair can be dissociated by interactions with the nucleons of the target nucleus or the produced particles surrounding the $c\bar{c}$ (comovers). These two mechanisms happen in hadron-nucleus collisions are described in the following:

Nuclear Absorption   Depending on the system properties (A, $\sqrt{s_{\mathrm{NN}}}$) and the momentum of the $c\bar{c}$, the traversal through the nucleus can lead to multiple scattering with the nuclear matter and cause the absorption of the $c\bar{c}$. The survival probability for the $c\bar{c}$ depends on the nucleon density in the nucleus A (as parametrized by a Woods-Saxon density distribution [50]). In Monte Carlo Glauber simulations [51] the average length of the nuclear $\langle L \rangle \propto A^{1/3}$ crossed by the pair is evaluated for the calculation of the time τ_c the $c\bar{c}$ spends in the CNM, see Eq. (2.2).

$$\tau_c = \frac{\langle L \rangle}{\beta_z \cdot \gamma}, \text{ with}$$
$$\beta_z = \tanh(y_{c\bar{c}}^{rest}) \text{ and } \gamma = E_{c\bar{c}}/m_{c\bar{c}} = m_{\mathrm{T}}\cosh(y_{c\bar{c}}^{rest})/m_{c\bar{c}} \tag{2.2}$$

The break-up of the resonance becomes only relevant if the formation time τ_f (see Tab. 2.1) is smaller than τ_c. The crossing times were calculated for the energies and acceptances of the different experimental measurements in A-A for $p_{\mathrm{T}} = 0$ and are quoted in Tab. 2.2. According to this nuclear absorption plays an important role at SPS energies and becomes negligible at LHC energies.

Comover Interaction   The charmonium created in a primary nucleon-nucleon collision can be dissociated through the interaction with the constituents of the sourrounding medium, so-called comovers. In a confined, hadronic medium (cold matter) the formed constituents are mostly pions. Therefore the cross section for comoving particles is

---

[3]The initial state effect of gluon (anti-)shadowing is also part of the CNM effects.

dominated by $\pi + J/\psi \rightarrow D\overline{D}$ processes. It was fixed from fits to low-energy experimental results to $\sigma_{co} = 0.6$ mb [52]. The interaction of comoving particles with the J/ψ happens preferably at low p_T, leading to a rise of the J/ψ $\langle p_T \rangle$ and $\langle p_T^2 \rangle$ with increasing charged particle density as illustrated in Fig. 2.3. Furthermore, a J/ψ produced with high transverse momentum may escape the interaction with the comovers (leakage effect) and consequently lead to an additional increase of $\langle p_T^2 \rangle$ [53]. For low particle densities comover absorption is irrelevant. In UrQMD simulations for pp collisons at $\sqrt{s} = 7$ TeV it was found that the charged particle density is sufficiently high enough (similar multiplicity to A-A collisons at SPS) and that up to 20% suppression of the initially produced J/ψ can be accounted to comover interactions [54].
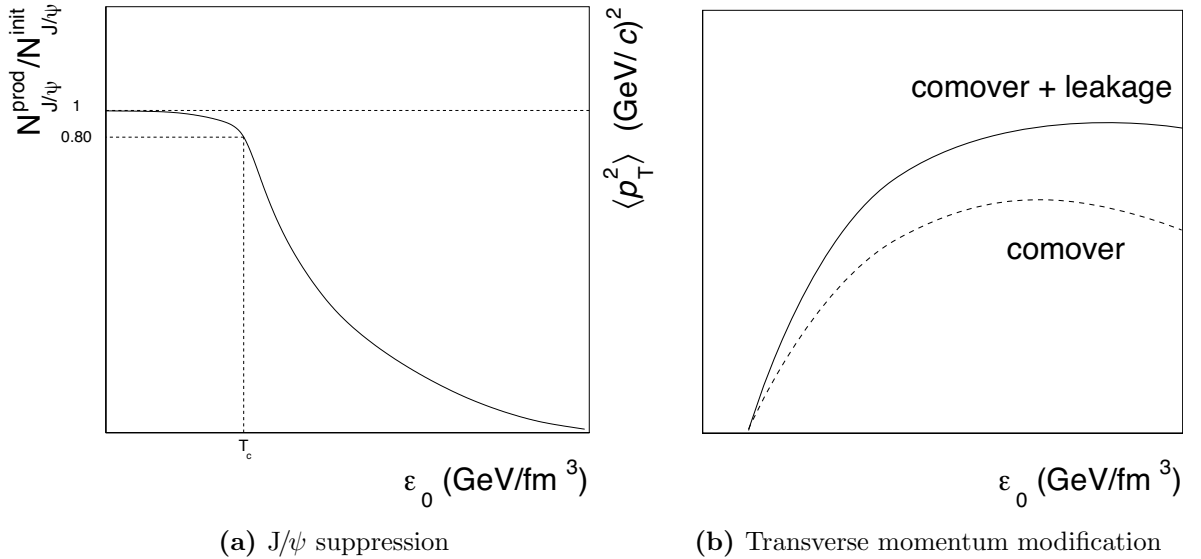

(a) J/ψ suppression

(b) Transverse momentum modification

Figure 2.3.: Schematic scenario of J/ψ suppression by comover collisions and the leakage effect versus energy density.

2.2.2. QGP-induced Effects

Color Screening   The dissociation of the charmonium states in a hot and dense QGP by Debye-like color screening was proposed as a signature for the formation of a deconfined medium [55] in 1986. In such a medium color charges are unbound; because the color field between the c and the $\bar{c}$ becomes modified, analogous to the well-known Debye screening in electro-dynamic plasmas described by Quantum Electrodynamics (QED). Accordingly the effective QCD potential is [56]:

$$V_{q\bar{q}}(r,T) \sim -\frac{4}{3}\frac{\alpha_{\mathrm{S}}}{r}\exp(-r/r_{\mathrm{D}}(T)) \qquad (2.3)$$

where the Debye radius r_{D}, depends on the medium temperature T and particle density n_0:

$$r_{\mathrm{D}} = \sqrt{\frac{kT}{4\pi n_0 \mathrm{e}^2}} \qquad (2.4)$$

As a consequence of the inverse proportionality to the color charge density, the color screening radius r_{D} decreases with increasing temperature. If r_{D} becomes smaller than the binding radius of the $c\bar{c}$, then the c and $\bar{c}$ can no longer see each other. The separated quark and anti-quark will bind with the surrounding quarks and form color neutral hadrons when the system freezes out. Since the $c\bar{c}$ states have different binding radii (respective dissociation temperatures, see Fig. 2.4), their sequential disappearance provides a way to measure the temperature of the medium [57] and is a crucial feature of deconfinement. This construct was established by the results of lattice calculations [58,59].

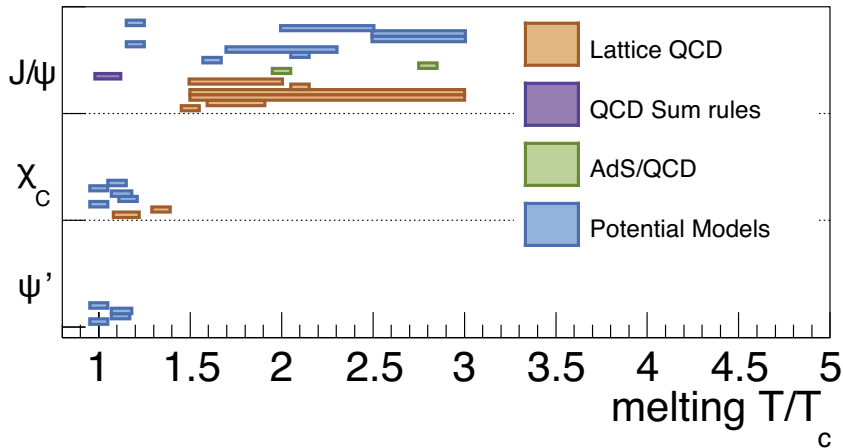**Figure 2.4.:** The dissociation temperatures of the charmonia states as calculated for several models. Modified version of [60].

The dissociation of the loosest bound $c\bar{c}$ state, the $\psi(2S)$, happens first and directly affects the yield of J/ψ due to the absence of the feed-down contribution, see Fig. 2.5a. The transverse momentum distributions suffer also from this feature and result in a

change of $\langle p_T^2 \rangle$ with increasing centrality [61]. Fig. 2.5b shows the $\langle p_T^2 \rangle$ of inclusive J/ψ versus energy density. The longer formation times τ_f of the higher $c\bar{c}$ states, hence more interactions and larger $\langle p_T^2 \rangle$, causes an interruption of the overall monotonic increase, when they start to disappear. When the higher states are gone and the dissociation temperature of the J/ψ is reached again a change of $\langle p_T^2 \rangle$ due to the dissociation, starting at low p_T and counteracting the p_T-broadening, happens.
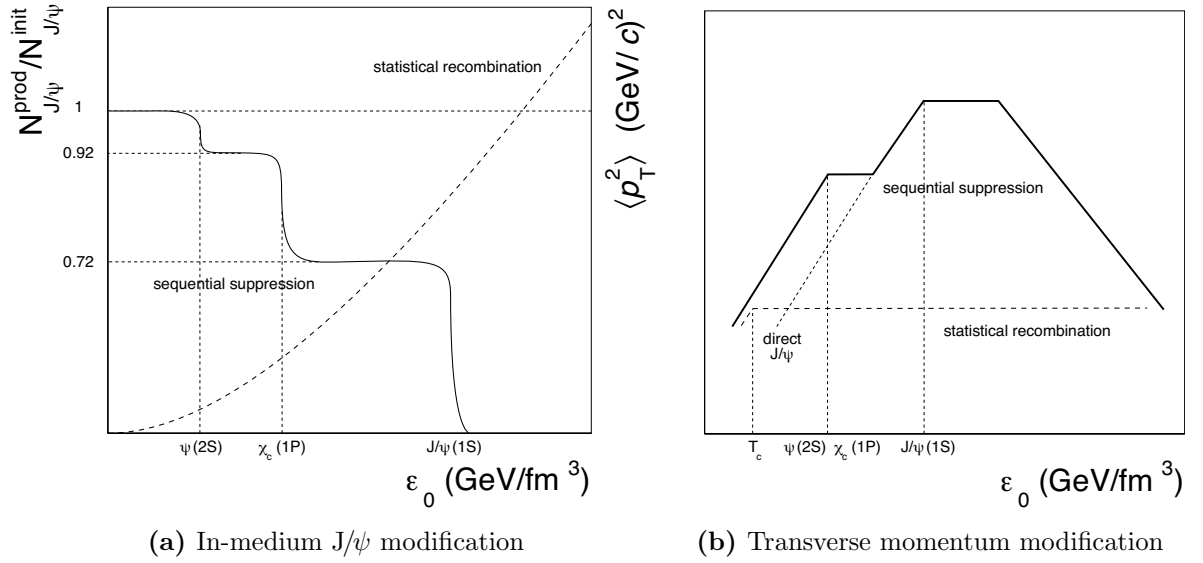

(a) In-medium J/ψ modification

(b) Transverse momentum modification

Figure 2.5.: Sequential J/ψ suppression by color screening and the effect of statistical recombination.

(Re)combination At higher energies, such as at RHIC and the LHC, the number of produced $c\bar{c}$ in one collision is sufficiently high (see Tab. 2.2), such that a different production mechanism might set in. Quarks of a dissociated $c\bar{c}$ originating from one hard interaction can in principle combine with those from other collisions or even recombine to a bound $c\bar{c}$ state. Such a processes can happen if the charm density of the medium at hadronization is adequate and requires a strong binding potential of random quarks into charmonia. The idea of $c\bar{c}$ (re)combination[4] (often called regeneration) was first formulated in [35, 62] and assumes that either all particles are produced at the chemical freeze-out at the phase boundary or (re)combination can happen during the whole evolution of the system. Since the number of NN collisions grows with increasing centrality, and thus the number of $c\bar{c}$ pairs $N_{c\bar{c}} \propto N_{\text{coll}}$, this approach predicts an enhancement of J/ψ production with the squared number of initially produced $N_{c\bar{c}}$, as sketched in

---

[4]The statistical hadronization process does not recover the initial, small fraction of correlated $c\bar{c}$ pairs from dissociated resonances.

Fig. 2.5a. This model implies that there is no thermal charm production and further that the initial chemical non-equilibrium persists throughout the evolution. The thermal charm production rate relative to that of light quarks for a hadronization temperature $T_c = 150 - 170$ MeV [63] is approximately $\sigma_{\mathrm{c}}^{therm}/\sigma_{\mathrm{u,d}}^{therm} \simeq \exp(-m_{\mathrm{c}}/T_c) \simeq 7 \times 10^{-4}$ and therefore negligible [64].

Recombination influences the momentum distribution of J/ψ. In contrast to the linear p_{T}-broadening pattern via initial state gluon scattering (g $-$ N), nuclear absorption (J/ψ $-$ N) and comover interaction (J/ψ $-$ h), J/ψ formed only at the hadronization point would show an almost flat $\langle p_{\mathrm{T}}^2 \rangle$ behaviour [65], since the different partners come from different collisions, see Fig. 2.5b. Recombination is the only effect so far that could explain an increase of the J/ψ production in heavy-ion collisions relative to pp collisions and/or to open-charm production. The contribution of such a mechanism would lead to a larger amount of J/ψ production at low p_{T} and since it is strongly correlated to the charm density this should be reflected in the mid-to-forward rapidity ratio (> 1) of J/ψ production. Further, if charm quarks do thermalize and participate in the collective motion of the QGP, then the azimuthal anisotropy should be transferred to the J/ψ, resulting in a measurable elliptic flow $0.02 < v_2 < 0.2$ [66, 67]. In addition if the formation of J/ψ happens through statistical recombination this effect should lead to an increase of v_2.

Corona effect   In [68, 69] the corona effect has been discussed in the context of J/ψ suppression. In all A-A collisions there is a rim region in the transverse plane where no formation of a QGP is expected, since the nuclear density (Woods-Saxon) of heavy-ions is low at the edges. This region, is called corona (see Fig. 2.6), and all observed effects should be similar to those in pp, p-A collisions. While in the core of the collisions, it is assumed that the formation of the QGP leads to full dissociation of all charmonia states. If this is true and only bound c$\bar{\text{c}}$ states from the corona survive, then this would lead to the same centrality dependence for J/ψ suppression at SPS, RHIC and the LHC energies (for same A and rapidity). As a consequence the transverse momentum distribution in A-A collisions should converge to that in pp interactions in the absence of charm flow.

Theoretical Conclusion

Charmonia, and in particular the J/ψ(1S) state, are excellent probes to study the properties of NN and A-A collisions. Due to their early formation and long lifetimes they are
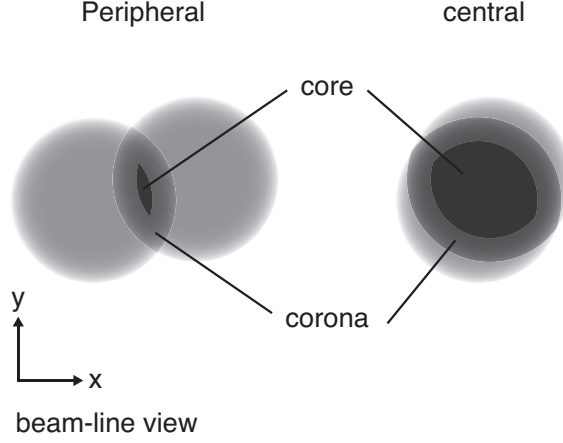
Figure 2.6.: The beam-line view a peripheral and central collision in the corona picture.

sensitive to the whole evolution of any created system and provide unique observables to study different types of interactions, such as comover, normal and hot matter interactions at different time scales. In all cases, the predictions for J/ψ modification are the cleanest for the ratio of hidden to open charm production, since in this case, the initial-state effects largely cancel. For J/ψ dissociation a unique suppression pattern is expected that could provide a clear indication for QGP formation. Further, the transverse momentum behaviour and elliptic flow of produced J/ψ can serve as an additional possibility to differentiate between various production scenarios.

2.3. Experimental Status of Charmonium Production

In this section, the experimental status of charmonium production is given with focus on heavy-ion collisions. Results are usually given in terms of ratios to the Drell-Yan dileptons ($q\bar{q} \to \gamma^* \to \ell^+\ell^-$) at SPS energy and to results of pp collisions scaled by the number of binary collisions ($N_{\text{coll}} \times \mathrm{d}N_{\text{pp}}/\mathrm{d}y$) at RHIC and LHC energies. The validation of both references is shown in Fig. 2.7. The Drell-Yan production is compared to the theoretically computed values from pp to Pb-Pb collisions and exhibits no nuclear dependence, thus is proportional to the number of NN collisions. At higher $\sqrt{s_{\text{NN}}}$, such as at RHIC or LHC, there is no invariant mass interval where Drell-Yan production dominates. Therefore a scaling with N_{coll} in the definition of the nuclear modification

factor $R_{\mathrm{AA}} = \mathrm{d}N_{\text{A-A}}/\mathrm{d}y/(N_{\mathrm{coll}} \times \mathrm{d}N_{\mathrm{pp}}/\mathrm{d}y)$ is favoured and was (finally) proven to work in results of the PHENIX [70] and CMS [71, 72] collaborations for electro-weak bosons, γ, W, Z^0. Their leptonic decay products ($\tau \approx 0.1$ fm/c) can pass the formed medium without interacting strongly and therefore serve as a reference measurement.

(a) Ratio of measured and theoretical Drell-Yan production.

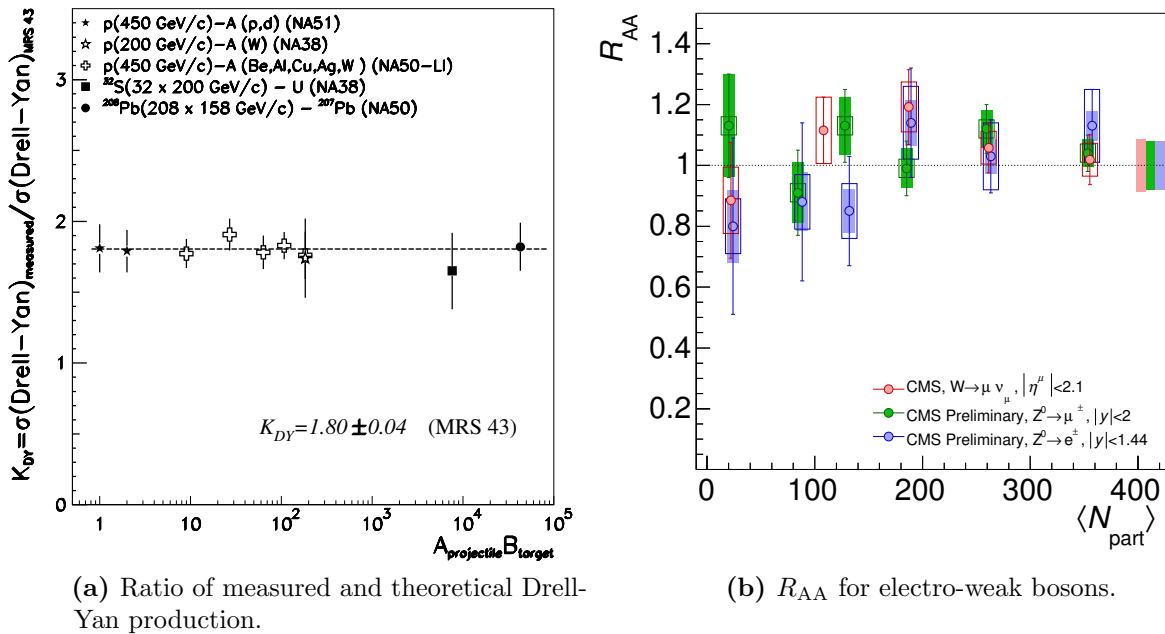**(b)** R_{AA} for electro-weak bosons.

Figure 2.7.: Validation of the scaling of hard production with the Drell Yan process and the number of binary collisions.

At SPS, the fixed target experiments NA38, NA50, NA51 and NA60 have measured J/ψ production for various systems (pp, p-A and A-A) and energies. An *anomalous suppression* of J/ψ(1S) and ψ(2S) production is observed when comparing measured results to expectations that include *normal* dissociation cross-sections $\sigma_{\mathrm{abs}}^{\mathrm{J}/\psi} = 4.2 \pm 0.5$ mb and $\sigma_{\mathrm{abs}}^{\psi(2\mathrm{S})} = 7.7 \pm 0.9$ mb [73], see Fig. 2.8a. They are found in nuclear absorption measurements by comparison to MC Glauber calculations. Usually this observable is expressed in units of the average crossing length $\langle L \rangle$ of the c$\bar{\mathrm{c}}$ pair, as described in Sec. 2.2.1. A stronger absorption is observed and was expected for the looser bound c$\bar{\mathrm{c}}$ state ψ(2S) leading to speculations of the observation of sequential suppression. However, a clear confirmation of this scenario is still due. On the other hand, a sequential dissociation pattern was discovered for the heavier quarkonia family (Υ(1S), Υ(2S), Υ(3S)) at the LHC see Fig. 2.8b.

Fig. 2.9 summarize the experimental results obtained for a broad range of centre-of-mass energies, where the J/ψ production was measured in the mid- and forward-rapidity region
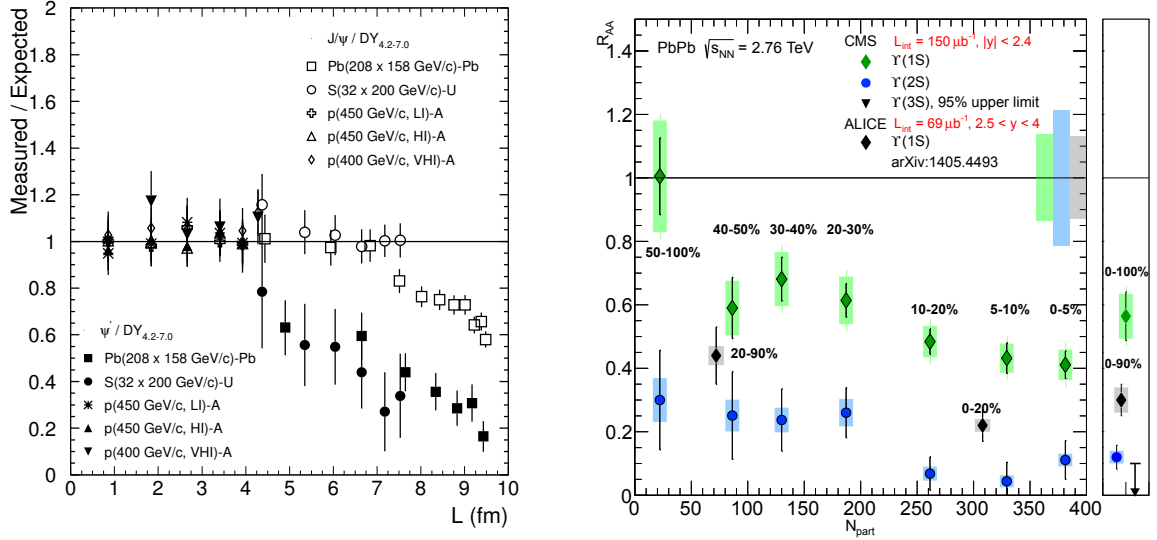
(a) Anomalous J/ψ, ψ(2S) suppression [73].

(b) Sequential Υ suppression [74, 75].

Figure 2.8.: Sequential charmonia and bottomonia suppression at the SPS and LHC.

and CNM effects are not taken into account. Compared to the SPS results a similar J/ψ suppression was reported by PHENIX and STAR collaborations for an order of magnitude larger $\sqrt{s}$ and correspondingly larger c$\bar{\text{c}}$ multiplicities. In the sequential suppression approach, the full suppression of the excited states (ψ(2S), χ_c(1P)) is expected, which would result in larger suppression of inclusive J/ψ(1S) due to disappearance of feed-down contributions. This additional suppression might be recovered by statistical recombination of c and $\bar{\text{c}}$. Qualitatively, this would be in agreement with the larger suppression observed in the PHENIX forward rapidity measurement [76] compared to mid-rapidity. An increasing contribution of J/ψ production through recombination might explain the smaller suppression observed in ALICE at the maximal centre-of-mass energy so far.

A compilation of J/ψ collectivity measurement is given in Fig. 2.10a. At the LHC, ALICE has measured the elliptic flow of inclusive J/ψ in semi-central nucleus-nucleus collisions for the first time[77]. This observation is confirmed and extended in transverse momentum by the CMS collaboration [78]. Model comparison e.g. [79] suggest a significant contribution from recombination and can qualitatively describe the data. The sizeable v_2 at high p_T, might be explained by contributions from thermalized b-quarks. In contrast to these observation, the STAR collaboration has measured an elliptic flow compatible with zero [80]. Already in 2008, the NA50 and NA60 collaborations had a preliminary look into this type of measurement and found indication for non-zero J/ψ v_2 at very low $\sqrt{s}$
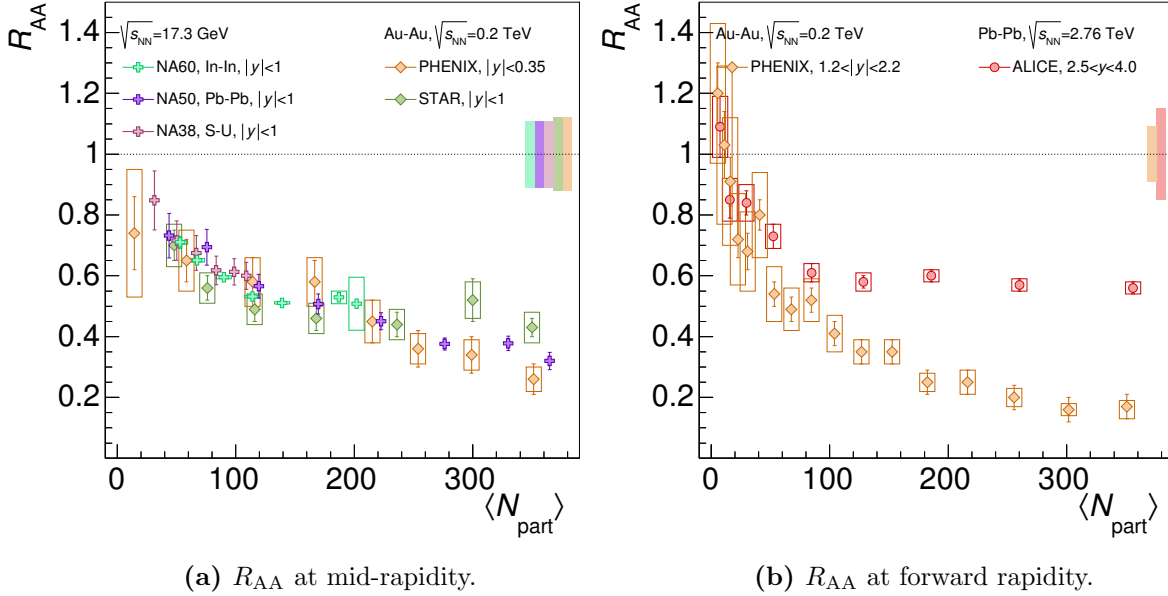
(a) R_{AA} at mid-rapidity. **(b)** R_{AA} at forward rapidity.

Figure 2.9.: Compilation of SPS, RHIC and LHC results on the nuclear-modification factor R_{AA} at mid- and forward rapidity.

[81, 82]. However, these analysis were never finished and therefore did not receive to much attention from the community.

The transverse momentum spectra of J/ψ have been studied by various experiments at all collision energies. At lower energy, the second moment of the p_T-distribution $\langle p_T^2 \rangle$ exhibits a linear increase with centrality for all colliding systems up to the onset of "anomalous suppression", see Fig. 2.10b at $N_{part} \approx 260$. Within the uncertainties, the PHENIX collaboration has observed a flattish behaviour of $\langle p_T^2 \rangle$ at $\sqrt{s_{NN}} = 0.2$ TeV [83].

Scheme of this Work

After the theoretical concepts and the experimental status have been introduced in this chapter, the scheme of this thesis is briefly explained. In the next chapter, the experimental device with the main parts used for charmonia analysis are presented. In Chapter 4 the details and results on the analysis of nuclear modification, the kinematics of J/ψ production and elliptic flow are described and their impact on the field of charmonia research discussed.
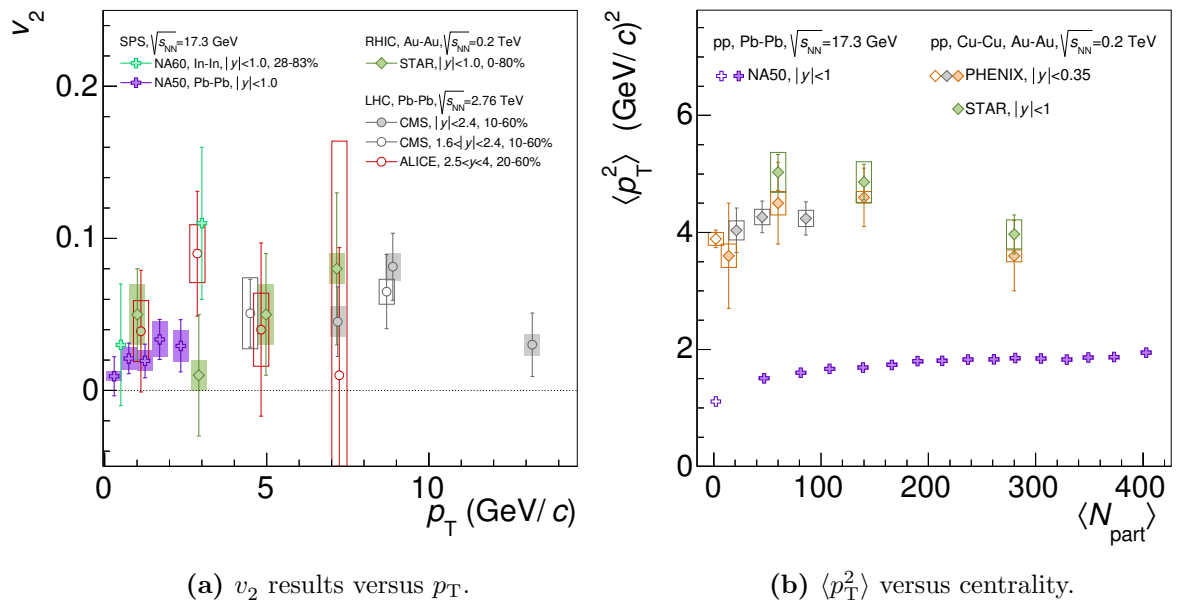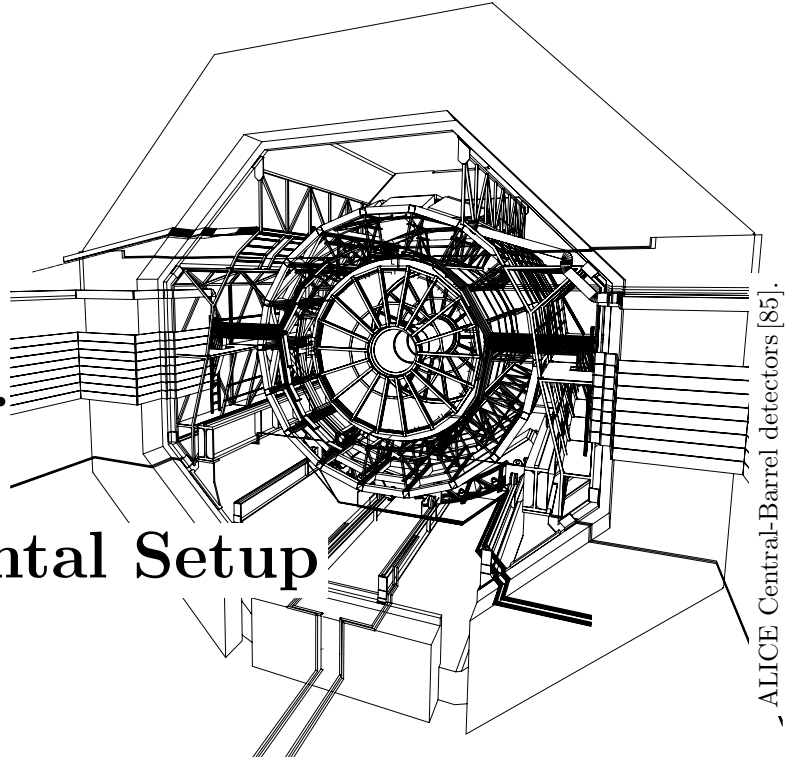
(a) v_2 results versus p_{T}.

(b) $\langle p_{\mathrm{T}}^2 \rangle$ versus centrality.

Figure 2.10.: Compilations of the elliptic flow v_2 and transverse momentum $\langle p_{\mathrm{T}}^2 \rangle$ measurements.

Chapter 3.

Experimental Setup

3.1. The Large Hadron Collider

The Large Hadron Collider (LHC)[84] is a superconducting hadron accelerator and collider located at CERN[1]. It was built 45 to 170 m below the surface in the 26.7 km circular tunnel, that was constructed between 1984 and 1989 for the Large Electron-Positron Collider (LEP). On the 16th of December 1994, the CERN Council approved the project to build today's most powerful accelerator ever constructed, the LHC machine. 25 years later, on November 23rd 2009, pp collisions at a centre-of-mass energy of $\sqrt{s} = 0.9$ TeV were recorded for the first time. The nominal centre-of-mass collision energy for this machine is 14 TeV and will be reached in the near future. In order to achieve these energies, the collider relies on several acceleration cavities, superconducting dipole magnets, two beam lines and further instruments for beam handling and diagnostics. Due to the limited space in the LEP tunnel, twin bore magnets are used. They consist of two sets of coils and beam channels within the same mechanical structure and cryostat. The field of the bending magnets has a maximum of $B = 8.33$ Tm operated at temperatures of 1.8 K through super-fluid helium cooling. With these magnetic bending, collisions of fully stripped lead ions $^{208}\mathrm{Pb}^{82+}$ are possible at a maximum beam energy of 2.76 TeV per nucleon. Using the LHC as an ion collider provides furthermore the possibility of proton-nucleus collisions, as recorded first end of 2012 with 4 TeV proton and 1.58 TeV per nucleon lead beam energies. Proton-lead (p-Pb) and lead-lead (Pb-Pb) collisions

---

[1]CERN, the European Laboratory for Particle Physics, in Geneva.

are provided to the four large experiments, ATLAS, CMS, LHCb[2] and ALICE[3], the dedicated heavy-ion experiment. The ALICE detector is located at the Interaction Point 2 (IP2) of the LHC ring, see Fig. 3.1, where, among others, the beam crossing angle is changed and beams are displaced in order to reduce the instantaneous luminosity $\mathscr{L}$ to the required level. The luminosity $\mathscr{L}$, a measure for the beam intensity, is given by the number of particles per bunch[4] and beam N_1, N_2, the accelerator revolution frequency f_{rev} and the effective transverse beam widths $\sigma_{x,y}$:

$$\mathscr{L} = \frac{N_1 N_2 f_{\text{rev}}}{4\pi \sigma_x \sigma_y} \tag{3.1}$$
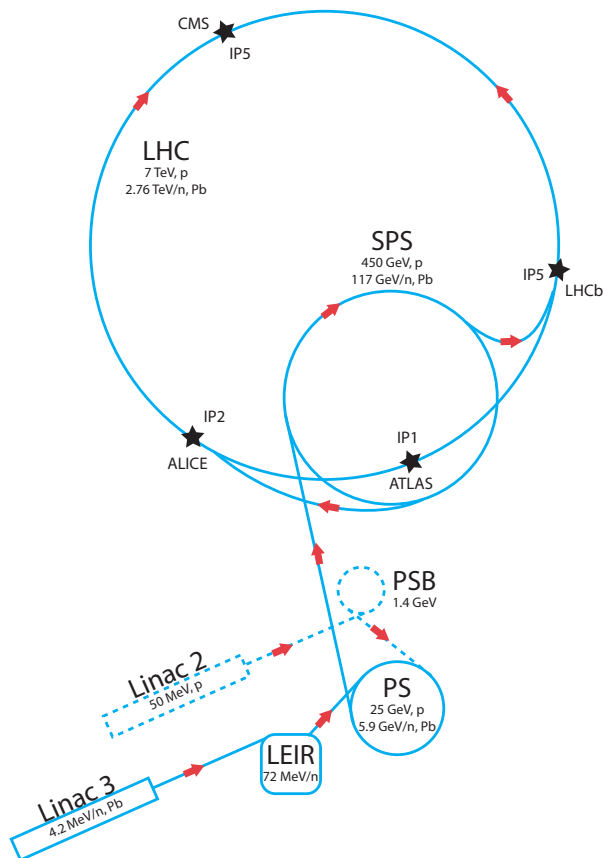
Figure 3.1.: The LHC accelerator complex for the different pre-acceleration steps of protons (dashed) and lead ions (solid).

---

[2]LHCb did not participate in the heavy ion program of LHC, since their detector was not designed for the corresponding high charge particle multiplicities. For p-Pb collisions at $\sqrt{s_{\text{NN}}} = 5.023$ TeV charge particle multiplicity is moderate enough.

[3]ALICE stands for A Large Ion Collider Experiment

[4]A bunch is the collection of accelerated particles captured within a longitudinally confined region provided by the Radio Frequency focusing system (one bucket).

Depending on the colliding system, a different chain of particle accelerators is passed, see Fig. 3.1. First electrons are detached from gaseous hydrogen and the linear accelerator (LINAC2) accelerates the protons to an initial energy of 50 MeV. Then they are injected into the Proton Synchrotron Booster (PSB), where they reach an energy of 1.4 GeV. In the following they join the standard acceleration section, that is common for protons and heavy ions. Gaseous lead, with an temperature of $\approx$ 820 K, is ionized by an electron current to mostly Pb^{29+}, which is then accelerated by the LINAC3 to energies of 4.2 MeV/n. After it passed a carbon foil, the Pb^{54+} are accumulated in the Low Energy Ion Ring (LEIR) and further boosted to 72 MeV/n. The transfer to the Proton Synchrotron (PS) completes the heavy-ion specific sequence. After further acceleration, bunches of protons or (finally) fully stripped lead ions are then injected into the Super Proton Synchrotron (SPS), before they reach the LHC. Tab. 3.1 summarizes the details of the ALICE data taking in Run1 for the years from 2009 to 2013.

system	$\sqrt{s_{NN}}$ (TeV)	$\mathscr{L}_{int}$	σ_{inel} (pp), σ_{vis} (p-Pb), σ_{tot} (Pb-Pb)
pp	0.9	0.33 nb^{-1}	not measured
pp	2.36	0.87 μb^{-1}	not measured
pp	2.76	0.18 pb^{-1}	$62.8 \pm 1.2 (vdM)^{+2.4}_{-4.0} (MC)$ mb
pp	7	5.4 pb^{-1}	$73.2 \pm 2.6 (vdM)^{+2.0}_{-4.6} (MC)$ mb
pp	8	9.7 pb^{-1}	not measured
p-Pb,Pb-p	5.02	31.2 nb^{-1}	$2.21 \pm 0.1 (stat.) \pm 0.05 (syst.)$ b
Pb-Pb	2.76	0.15 pb^{-1}	$7.7 \pm 0.1 (stat.)^{+0.6}_{-0.5} (syst.)$ b

Table 3.1.: The different LHC running configurations, delivered integrated luminosity [86] for mixed trigger modes and obtained inelastic, visible and total cross sections for the various collision systems [87, 87, 88] obtained by several van-der-Meer-scans [89]. The visible cross section σ_{vis} seen by e.g. the V0 detector for a certain trigger condition is the fraction of the total inelastic interaction cross section $\sigma_{inel} = \sigma_{vis}/\epsilon$, where ϵ is the fraction of inelastic events which meet the trigger condition [88].

3.2. A Large Ion Collider Experiment

The ALICE experiment is the dedicated general-purpose heavy-ion detector at the LHC. It was designed to study strongly-interacting matter created in nucleus-nucleus collisions at very high track densities and temperatures. High precision measurements down to very

low transverse momenta and excellent particle identification capabilities are its unique characteristic. Therefore the material budget and the magnetic field of 0.5 T is the lowest among the four big experiments (4 T in CMS, 2 T in ATLAS, 4 Tm in LHCb). Fig. 3.2 shows an schematic representation of the experiment. It consists of 18 detectors that can be divided into three parts: the Central-Barrel detectors, the muon spectrometer and the forward detectors. In the following sections they will be introduced.
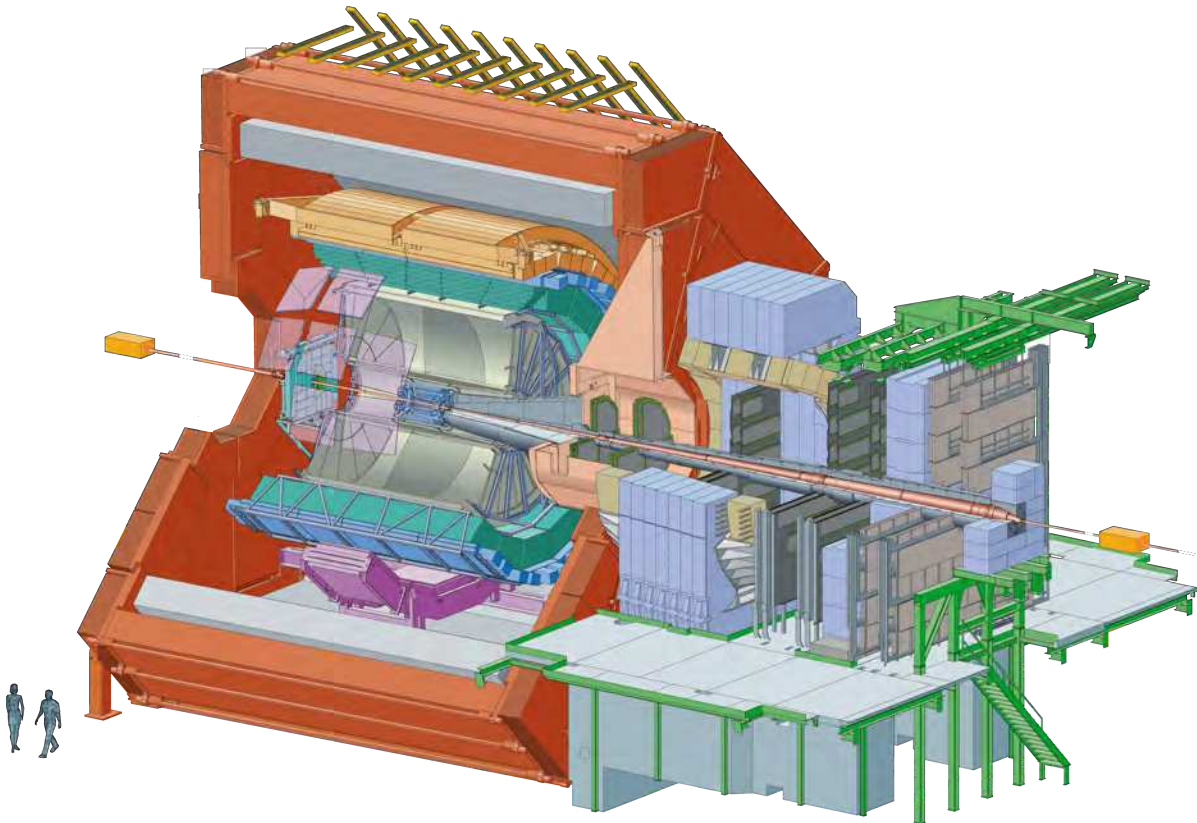

Figure 3.2.: Schematic layout of the ALICE experiment [90].

3.2.1. Central-Barrel Detectors

The Central-Barrel of the ALICE experiment provides an excellent particle identification in the pseudo-rapidity range from -0.9 to 0.9. A separation of pions, kaons, protons and electrons over a large transverse momentum range is possible thanks to the variety and interplay of the different detectors. The good track and vertex resolutions allow the separation of primary[5] and secondary particles[6] and the reconstruction of e.g. charmonia

---

[5]In the ALICE definition for primary particles, all charged particles produced in the collision and their decay products are considered, that do not originate from weak decays of strange hadrons.

[6]Secondary particles have a displaced vertex, that is separated from the interaction point.

from b-hadron decays. Important detectors in the analysis of J/ψ production, see Chapter 4, are the Inner Tracking System (ITS), the Time-Projection Chamber (TPC) and the Transition Radiation Detector (TRD). They are described in the following in more detail.

Inner Tracking System

The Inner Tracking System [91] was build in order to precisely reconstruct the primary interaction vertex and consequently allows the identification of secondary particles. The vertex resolution scales with the number of charged particles $\sigma_{x,y,z} \propto 1/\sqrt{\mathrm{d}N_{ch}/\mathrm{d}\eta}$. For 5% most central Pb-Pb collision the vertex resolution in beam direction is approximately 9.0 ± 0.3 µm. In addition, the ITS improves the angle and momentum resolution of particles by a factor of ≈ 3 (at high p_T [86]) and has the capability to do particle identification via a $\mathrm{d}E/\mathrm{d}x$ measurement. The ITS consists of 3×2 cylindrical layers of silicon detectors as illustrated in Fig. 3.3. Three different technologies with different polar acceptances and purposes are combined: Silicon Pixel Detector (SPD), Silicon Drift Detector (SDD) and Silicon Strip Detector (SSD). The tracking component is common for all detectors. The SPD focuses on vertex reconstruction and since its the fastest detector in the Central-Barrel. It can provide a multiplicity and topology based L0 trigger signal to other detectors. The hit multiplicity in the SPD allows a precise determination of the collision centrality as done in [92]. The four outer most layers of the ITS have analogue readout and therefore provide a $\mathrm{d}E/\mathrm{d}x$ measurement for the non-relativistic ($1/\beta^2$) region, see Fig. 3.4a. The geometrical dimensions of the various sub-detectors are summarized in Tab. 3.2.
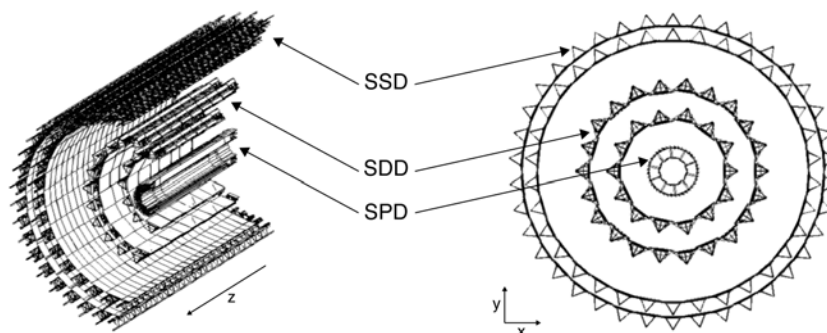

Figure 3.3.: Layout of the Inner Tracking System.

(a) The ITS dE/dx distribution versus momentum.

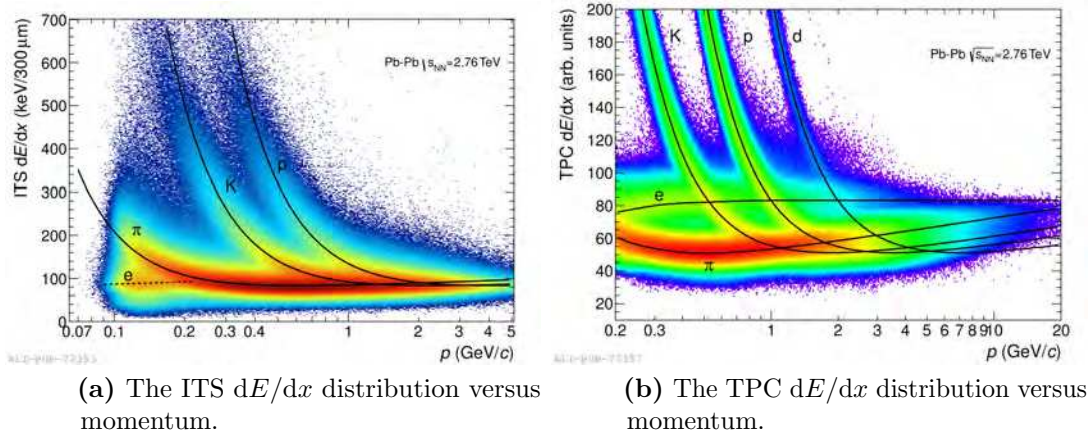**(b)** The TPC dE/dx distribution versus momentum.

Figure 3.4.: The PID performance of the ITS and TPC in Pb-Pb collisions at $\sqrt{s_{NN}} = 2.76$ TeV versus momentum [86]. Lines show the parametrizations of the expected mean energy loss.

detector	layer	modules	position (cm)		acceptance	
			radial	longitudinal	azimuth	polar
SPD	1	80	3.9	± 14.1	full	$|\eta| < 2.0$
	2	160	7.6	± 14.1		$|\eta| < 1.4$
SDD	3	84	15.0	± 22.2	full	$|\eta| < 0.9$
	4	176	23.9	± 29.7		
SSD	5	748	37.8	± 43.1	full	$|\eta| < 1.0$
	6	950	42.8	± 48.9		

Table 3.2.: The kinematical acceptance, geometrical dimension and segmentation of the ITS sub-detectors [86, 90].

Time-Projection Chamber

The Time-Projection Chamber [85] is the main tracking device of the Central-Barrel. The detector is composed of a large cylindrical field cage and has an active volume of ≈ 88 m^3 filled with a gas mixture of Neon (Ne), Carbon dioxide (CO$_2$) and Nitrogen[7] (N$_2$) in proportions 90/10/5. By a central high-voltage electrode the 5 m long field cage is separated into two readout volumes with drift fields in opposite orientations. The longitudinal acceptance (in beam-direction) is defined by the inner ($r_{min} = 84.8$ cm)

---

[7]Nitrogen was removed after 2010 data taking, in order to test its potential negative influence on the magnitude of discharges in the gas (*Streamer*).

and outer radius ($r_{\text{max}} = 246.6$ cm) of the cylinder to $|\eta| < 0.9$ ($|\eta| < 1.5$ for reduced (1/3) radial track length). According to this the TPC collects up to $N_{\text{ch}} = 5000$ primary particles per event, which is motivates the granularity of the detector. As depicted in Fig. 3.5, the full azimuth is divided into 18 segments, while there are two (inner and outer) read-out chambers in the radial direction. In addition to the track reconstruction of particles in the range $0.1 < p_{\text{T}} < 100$ GeV/c, the TPC allows to identify particles with high resolution ($\sigma_{\text{d}E/\text{d}x} = 6.5\%$ for 5% most central collisions [86]). If a fast particle traverses gas, it excites and ionizes gas atoms along its flight path. As a consequence, it looses an amount of energy per unit path length ($\text{d}E/\text{d}x$) which is specific for each particle. The energy loss (stopping power) of a particle is described by the Bethe-Bloch equation [20],

$$-\left\langle \frac{\text{d}E}{\text{d}x} \right\rangle = Kz^2 \frac{Z}{A} \frac{1}{\beta^2} \left[\frac{1}{2} \ln\left(\frac{2m_{\text{e}^-}c^2\beta^2\gamma^2 E_{\text{max}}}{I^2} \right) - \beta^2 - \frac{\delta(\beta\gamma)}{2} \right], \qquad (3.2)$$

where these medium parameters enter: mean excitation energy I, the atomic Z and mass A number and the maximum energy transfer to an electron in a single interaction E_{max}. The velocity of the particle β and the Lorentz factor γ are the usual relativistic variables. K is a constant and $\delta(\beta \gamma)$ is the density effect correction to ionization energy loss at high projectile energies. For a given momentum, the $\langle \text{d}E/\text{d}x \rangle$ of a particle depends only on the mass and charge z of the particle.
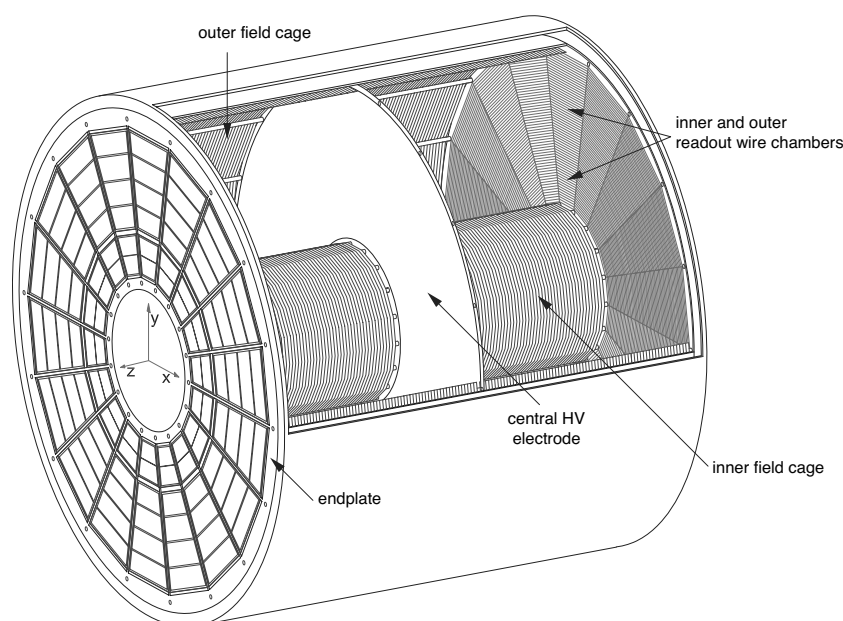

Figure 3.5.: Layout of the Time-Projection Chamber [93].

The TPC is a particle detector which allows for the three dimensional reconstruction of particle tracks by collecting their ionization electrons drifting in an electric field towards the readout planes, see Fig. 3.5. Two dimensions (x and y) are accessible via the induced signals (cluster) on the pads of the two readout plates. The drift velocity is constant due to the fact that the acceleration along the field lines is compensated by collisions with the gas molecules. Therefore the drift time provides the z-coordinate of the trajectory. Thanks to the homogeneous magnetic field in the Central-Barrel, a momentum and charge measurement of the particles traversing the TPC is possible. The bending radius and its sign provide the necessary information that is used further on in the track reconstruction algorithm [27] where the clusters are associated to tracks. In Fig. 3.4b the mean energy loss per track length $\mathrm{d}E/\mathrm{d}x$ for given particle momentum is shown and demonstrates the particle separation power of the TPC.

Transition Radiation Detector

The main purpose of the Transition Radiation Detector [94] is to improve the particle identification, in particular the separation of electrons and pions (hadrons) for momenta above 1 GeV/c. It is situated around the TPC and covers a pseudo-rapidity range $|\eta| < 0.84$. Fig. 3.6 shows the different reconstruction steps starting in 2009. In fall 2014 the last five supermodules where installed and full azimuthal coverage was achieved.

The TRD is divided into 522 individual readout chambers DET, which are arranged into 18 super modules SM (in ϕ), each containing five stacks in beam direction with six layers in radial direction, see Fig. 3.7. Depending on the position, a chamber contains 12 to 16 pad rows with 144 pads each, that are read out by eight Multi-Chip Modules (MCM). The entire readout electronics and their water cooling system are directly mounted on the back panel of the chamber.

The readout chambers are made of Multi-Wire Proportional Chambers (MWPC) extended by a 3 cm long drift volume to allow for fast reconstruction of track segments and by a carbon fibre laminated Rohacell/polypropylene fibre sandwich radiator mounted in front. Due to its high photo absorption cross section for X-rays and quenching capabilities a gas mixture of 85% Xenon (Xe) and 15% carbon dioxide (CO_2) is chosen for the drift volume. The time evolution of the signal (drift time of ≈ 2 µs) is sampled in 24(30) time bins[8] and allows for better electron/hadron separation. Signals are collected by the cathode pads at the end of the amplification region with high granularity in order to

---

[8]The number of time bins were gradually reduced in order to gain time for the TRD trigger.
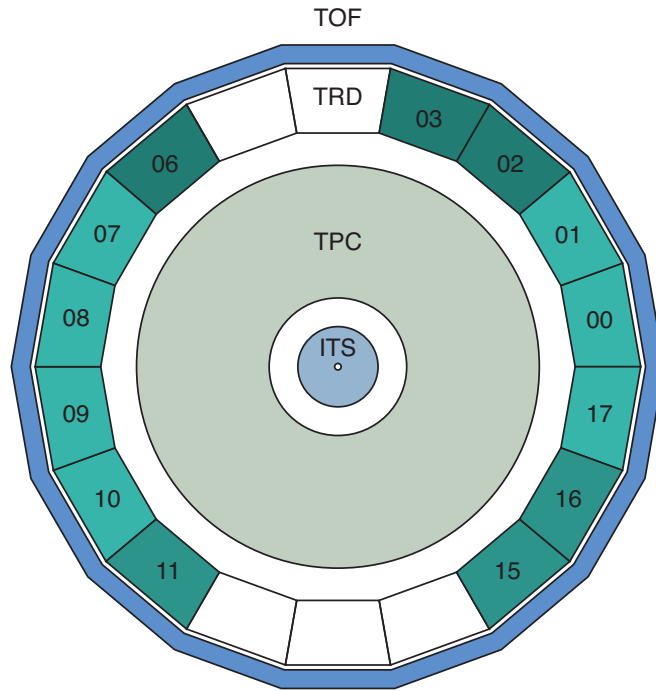
Figure 3.6.: Schematic layout of the Transition Radiation Detector and the operational super modules in 2009 (light) to 2012 (dark green).
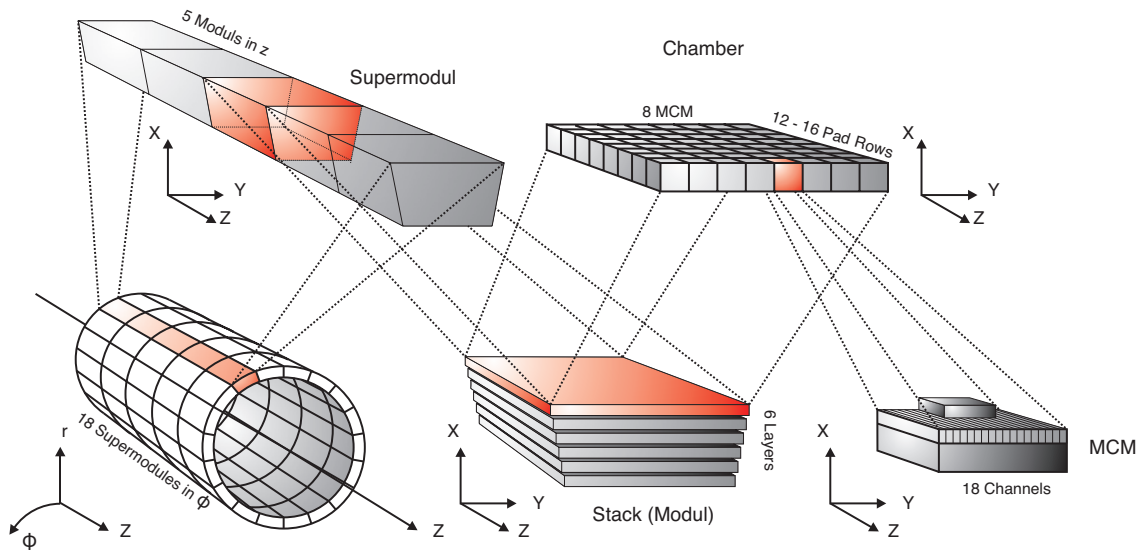
Figure 3.7.: The segmentation of the TRD in cartesian coordinates.

achieve high tracking resolution and a sufficient track matching to the TPC and TOF. Ultra-relativistic particles with a $\gamma \gtrsim 10^3$ traversing the radiator, made of many interfaces of two media with different dielectric constants, produce transition radiation (TR) with an energy of $1 < E_\gamma < 30$ keV that is absorbed in the detector gas, see Fig. 3.8a. Since the mass ratio of hadrons to electrons is larger than 10^2 TR is dominantly produced

for electrons and allows for separation of electrons and hadrons. In addition the TRD combines the specific energy loss (dE/dx) of the particles as described in Sec. 3.2.1 with the TR information to identify particles as illustrated in Fig. 3.8b.
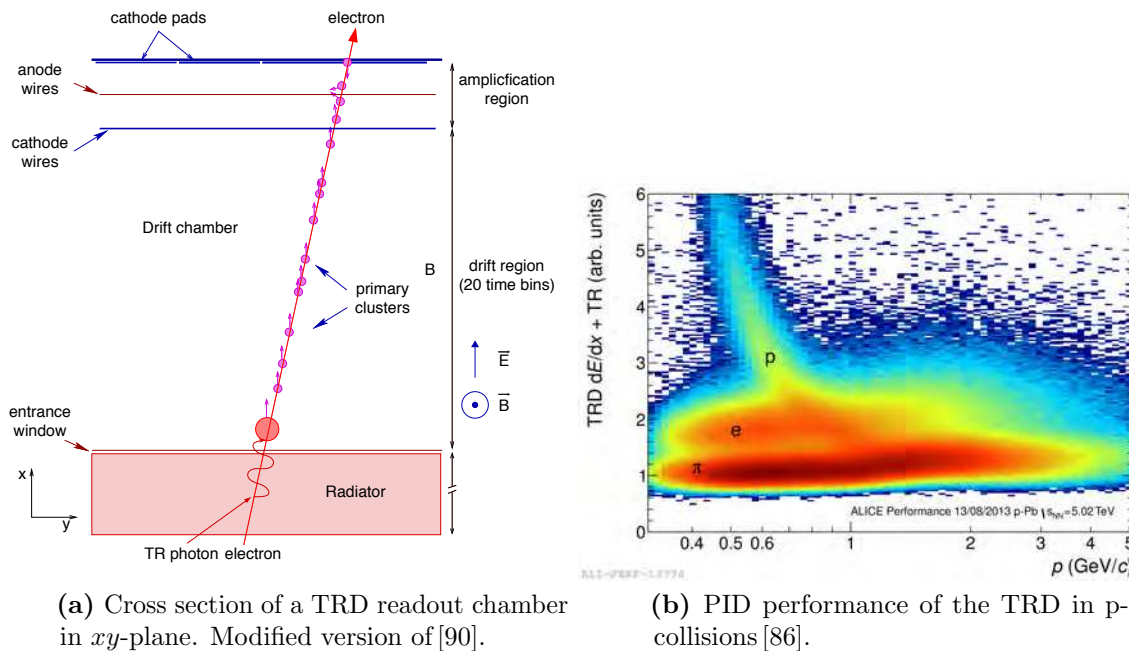
(a) Cross section of a TRD readout chamber in xy-plane. Modified version of [90].

(b) PID performance of the TRD in p-Pb collisions [86].

Figure 3.8.: Cross sectional view of a readout chamber and the PID signal measured in p-Pb collisions at $\sqrt{s_{NN}} = 5.02$ TeV.

In addition to the particle identification, the TRD extends the tracking capabilities in transverse momentum and improves the p_T resolution of the Central-Barrel for high-p_T particles ($6 \to 4\%$ for $p_T \approx 100$ GeV/c). Furthermore, the TRD can provide a L1-trigger based on online reconstructed TRD tracklets and the PID information, which was first tested in 2012 and 2013 with jet and heavy-quark trigger configurations.

Calibration   As any other detector, the TRD needs to be calibrated in order to produce meaningful results. In this work the calibration procedures [95] for the TRD were extended by the so-called *chamber status* calibration. The chamber status (*good, bad, not calibrated* and *no data A-,B-side*) depend on the calibration of the drift velocity v_D, the gain G and the $E \times B$ shift. In general, variations of these calibration parameters can occur due to time-dependent fluctuations of the temperature, pressure and the gas mixture or variations of geometrical imperfections such as alignment and the time-offset t_0 in electronic components. v_D and t_0 calibration parameters are obtained from the signal

distribution as function of time, where the time window corresponds to the drift length of 3 cm. The gain factor calibration is done relative to all other chambers and based on the average of the collected charge integrated over all time bins. Since the magnetic field $\vec{B}$ and the drift field $\vec{E}$ are orthogonal, the ionization electrons do not drift in the direction of $\vec{E}$, but according to the Lorentz angle α_{L}. This results in a bias of the y-position of clusters leading to a false ϕ angle of the reconstructed track that needs to be corrected for. The status of any readout chamber is related to the number of clusters N_{cls} associated to the online-tracks of the TRD. Half-chambers that do not satisfy the requirement of $N_{\mathrm{cls}}(\mathrm{DET}) > 5\% \cdot \langle N_{\mathrm{cls}} \rangle$ are treated as chambers without data or with problems. Optionally this calibration algorithm can be applied without tracking information. The number of active and successfully calibrated chambers enters into MC simulations and guarantees a proper calculation of the acceptance, reconstruction and PID efficiency of tracks propagated to the TRD. In the online version of this calibration algorithm the chamber status is compared and updated by the Detector Control System (DCS) at the end of the run. The status of the half-chamber is related to the global state of the half-chamber merger MCM and problems are propagated to the final status.

Monitoring and Quality Assurance In order to assure a good quality of the data by the TRD in physics analyses, several checks on the calibration and reconstructed raw data are necessary. The data taking in ALICE is divided into periods in which the detector configurations and the most important beam parameters such as collision system and energy are foreseen to be stable. The data taking periods consists of several runs, where the start/end of the run is defined by either an activity in the LHC (e.g. new fill, beam dump, ...) or a problem in the detectors or the DAQ[9]. In the first step a small fraction of the raw data of each run is used to perform the calibration (*cpass0*), then this part of the data is reconstructed (*cpass1*) and analyzed by a central organized Quality Assurance (QA) group, where each detector provides feedback on the quality of the data and the detector performance in terms of vertex finding, tracking and track matching, PID etc.. Afterwards a validation production with the updated calibration parameters starts and the data quality is judged based on a larger amount of statistics. After successful validation a sufficient quality of the calibration and reconstruction is assured and the actual full raw data production (*pass1,2,...,N*) can start. In the course of this thesis an automatic procedure was developed that monitors the time dependence of the calibration parameters [96] and the outcome of all reconstructions steps in all aspects of

---

[9]DAQ stands for the central data acquisition system of ALICE.

the detector performance [97]. Fig. 3.9 shows some examples on the monitoring interface
of the calibration and reconstruction QA. In addition, a self-updating web-interface [98]
was created for expert-QA that covers all details of the detector performance obtained
in the offline processing of TRD data. Furthermore the system is equipped by an mail
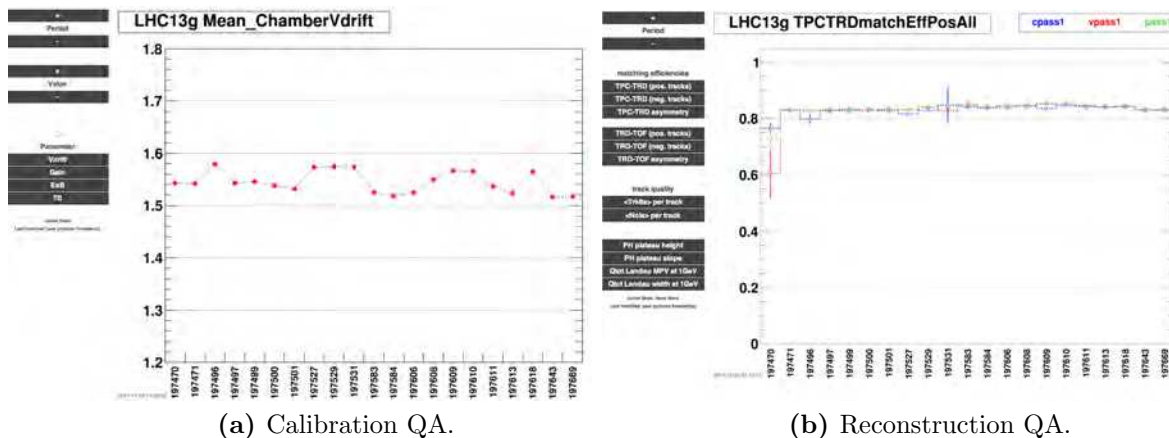warning system that operates on limits for calibration parameters set by the experts[10].

(a) Calibration QA.   (b) Reconstruction QA.

Figure 3.9.: The web-interfaces of the trending web-pages for calibration and recon-
struction QA.

3.2.2. Muon Spectrometer

Together with a limited number of the forward detectors (ZDC, PMD, FMD[11], T0, V0)
and the SPD detector, described in Sec. 3.2.1, the muon spectrometer [99] can provide
excellent muon measurements taking into account all event characteristics and at a
higher trigger rate than the general ALICE Central-Barrel rate. With this configuration
the complete dimuon spectrum including the low- and higher mass resonances in the
pseudo-rapidity region $-2.5 < \eta < -4$ can be measured with an improved counting
rate. The muon spectrometer, located between $-17.1 < z < -0.9$ m, consists of a
frontal photon and hadron absorber ($\approx 10\lambda_{\mathrm{int}}$) made of carbon, concrete and steel, a
large dipole magnet (B=0.67 T), a sequence of ten high-granularity tracking planes,
followed by an iron wall ($\approx 7.2\lambda_{\mathrm{int}}$) that protects the four muon trigger chambers (muon
$p > 4$ GeV/c). Over the whole spectrometer an inner beam shield made of tungsten, lead
and stainless steel was installed around the beam pipe for protection against primary
and secondary particles produced at large rapidities. Due to the thick frontal absorber

---

[10]This alarm system is optional and not longer maintained.

[11]ZDC, PMD and FMD stands for Zero Degree Calorimeter, Photon Multiplicity Detector,
   Forward Multiplicity Detector.

particles experience multiple scattering which leads to an reduced momentum resolution. However, it guarantees very high muon purity and much lower detector occupancies than in the Central-Barrel detectors.

3.2.3. Forward Detectors

The forward detectors have limited acceptances and therefore either provide complementary measurement to Central-Barrel results, e.g. FMD extends the η range of the $dN_{ch}/d\eta$ measurement [92], or serve as trigger detectors. For the analysis of charmonia, only the V0 detector, T0 detector and the ZDC are of use. They are described briefly in the following.

Zero Degree Calorimeter

Zero Degree Calorimeters are used since a long time in heavy-ion experiments. They provide information on the collision centrality by collecting spectator nucleons of p-A and A-A collisions. A L1-trigger based on this information can also be used to suppress the electromagnetic interactions between the lead ions. Since the ZDC is further sensitive to the distribution of the spectators in x and y it can give an estimate on the reaction plane of the collision. ALICE has two sets of hadronic ZDCs located $z = \pm 116$ m away from the nominal interaction point. Due to the deflection of protons by the magnetic dipoles and quadrupoles of the LHC, neutron and proton spectators are detected separately. In addition to the hadronic ZDCs, two small electromagnetic calorimeters (ZEM) are placed at $z = \pm 7$ m for the energy measurement of particles emitted at forward rapidity. Since in very peripheral A-A collisions the spectators remain in the beam pipe, a correlation between ZDC and ZEM signal allows to disentangle central from very peripheral events.

V0 Detector

The V0 detector [100] is a very powerful, small angle detector consisting of two arrays of scintillators counters (V0A,V0C), each with 32 cells. They are located asymmetrically around the interaction point, and are therefore sensitive to different phase space regions of the collision. A coincidence between the two arrays (or to the SPD) serves as the standard minimum bias trigger in pp, p-Pb and Pb-Pb collisions and the measured amplitude can be used to configure a centrality trigger. Due to the segmentation (4×8

in r, ϕ) a reaction plane can be estimated and used for flow analyses. Furthermore, the V0 detector contributes to the cross section measurements in pp and p-Pb collisions [87, 88] and gives the best resolution in the determination of the collision centrality [92].

T0 Detector

The T0, a Cherenkov detector, is separated into two arrays (12 counters each) and situated in radial $r = 6.5$ cm and longitudinal positions $z = -72.7, +375$ cm. It was designed to generate a start time signal (T0) for the Time-Of-Flight detector (TOF) with 21 ps resolution [86] and additionally provides a pre-trigger 'wake-up' signal to the TRD. With the time information of both arrays the position of the primary collision vertex can be determined online with a resolution of ≈ 1.5 cm [90].

3.3. The ALICE Analysis Environment

The analysis environment in ALICE is based on the ROOT system [101]. ROOT is an object oriented framework written in C++, that was developed for handling of the large amount of data collected by the LHC experiments. It contains a huge arsenal of software tools for data analysis, simulations and I/O operations, which allow to efficiently access and write large data objects. Furthermore it contains a C++ Interpreter CINT which can process C/C++ macros in the command line without the need of a full compilation. With CINT frequent code development can fast and easily be tested. AliRoot [90] is the software package used in ALICE and exploits a large number of elements offered by ROOT. It is complemented by the ALICE-developed AliEn system [102] which gives access to the Worldwide LHC Computing Grid (WLCG) [103], a virtual super computer. AliRoot contains the functionalities to simulate, reconstruct and analyze data and is integrated into almost all parts of ALICE. Several interfaces to external Monte Carlo (MC)[12] tools such as event generators (Pythia [104, 105], DPMJET [106] or HIJING [107]) and detector simulations (FLUKA [108] and GEANT3 and GEANT4 [109, 110]) are provided.

---

[12]Monte Carlo simulations is a stochastic approach, where a process is randomly sampled many times to obtain a numerical results.

3.3.1. Analysis Train Framework

The large amount of collected[13] and simulated data in ALICE requires organized data processing. For physics analyses a common train system was developed in AliRoot. One or several individual analysis tasks are grouped into wagons, that can participate in a train. Such trains run centrally on a large computing site for a defined dataset. In a train run the code of all participating train wagons is executed consecutively on each event of the dataset. This reduces the number of I/O operations dramatically and easily allows to exploit synergies.

The analysis train framework used in this work is the LEGO[14] train system [111]. The train operator combines several wagons (requested by the users) for a given dataset in a web-based GUI environment. In an automatic way functionality and consumption in terms of computing resources of all user wagons are validated. Afterwards, the LEGO train system organizes the submission of the analysis train and the merging of the output. The LEGO train system is operating since 2012 and was continuously extended in functionality and operability. Besides user analysis, the system is used for QA, low scale MC production and re-filtering of data. Currently, $\approx 70\%$ of all analysis activities within ALICE are done via the LEGO train framework.

3.3.2. Dielectron Package

Several packages (FLOW, HFE, D2H, MUON) which address different analysis topics are built inside AliRoot. The main advantage of a common analysis package is that the code development only has to be done once, resulting in low redundancy and high quality. In the course of this thesis a joined framework for all dielectron studies was developed: the dielectron package. It provides high flexibility in the configuration for the end-users needs. All technical components, definitions and routines are put together in a generic analysis task. In the following the layout of the dielectron package and its structure is described.

The current version of the framework contains 43 classes that can be categorized into the following elements:

---

[13]In Run1 of the ALICE data taking 5.185 PB of raw data were recorded [86].
[14]Lightweight Environment for Grid Operators

Architecture: This part of the software package provides the infrastructure for data transfer and the definition of the output structure, e.g. container, histograms and trees.

Methods: Components and routines used for the selection of runs, triggers, events, tracks, V0s and pairs are defined. All kind of calculations (pairing, rotation, fitting, etc.), corrections (event-plane, PID and efficiency), as well as the buffering for event mixing are implemented in these classes. The final content of the analysis is defined by this module.

Processes: The main steering class in this element is AliDielectron. Here all parts of the analysis are executed and the data is posted to the output containers.

Tools: A large set of well tested tools for the production of analysis results, e.g. any kind of signal extraction, efficiency calculation and their graphical representation is offered. These classes can be utilized by the end-user in smaller scripts that are then processed within ROOT.

A central class of the dielectron package is the AliDielectronVarManager, which holds continuously all used information for a given particle and event through the whole framework. This manager is connected to all elements described above and is decoupled from the event type (ESD, AOD, MC).

Fig. 3.10 shows the schematic structure of the dielectron framework. In the first part of the analysis, the user chooses one of the available analysis tasks. Then the output structure and its content is defined, before the analysis techniques (any kind of selection, background estimation or correction) and their sequence are configured. After the configuration part is done, the type of data format is selected and the submission of the analysis can start. In the last step of the analysis, the output is either post-processed by e.g. making use of several verified analysis tools or, in case of a new data production through filtering/skimming, it can be utilized in a second iteration.
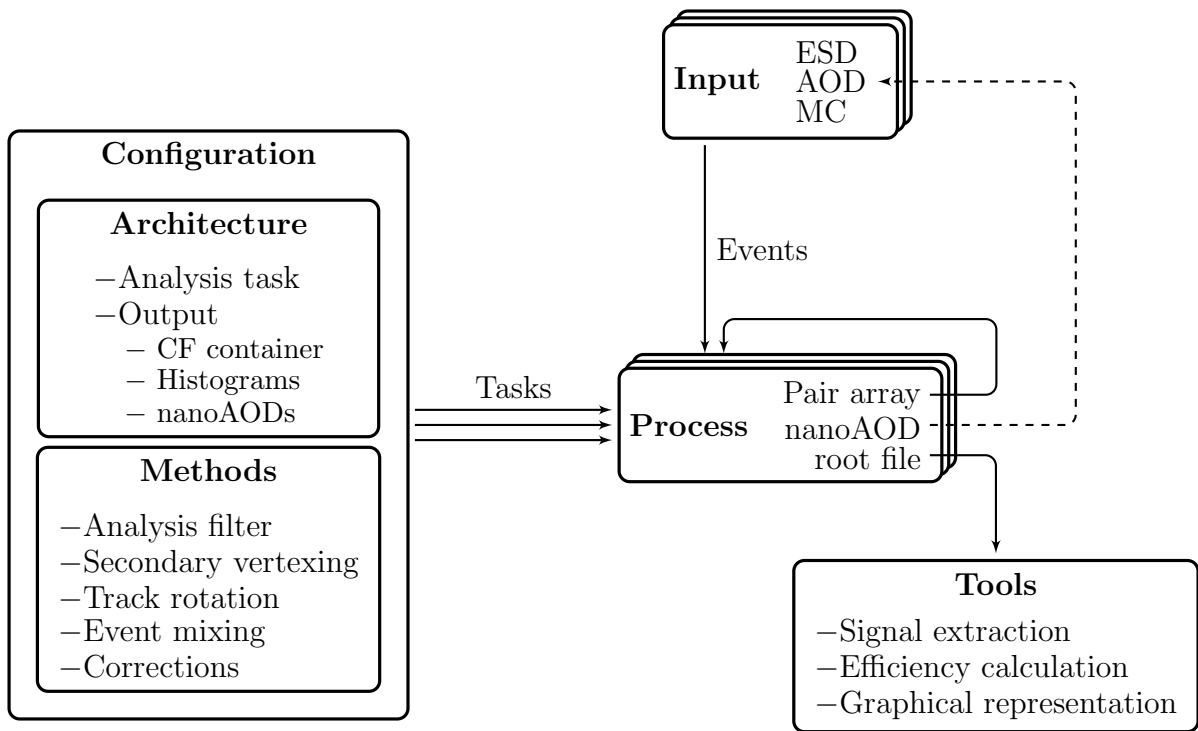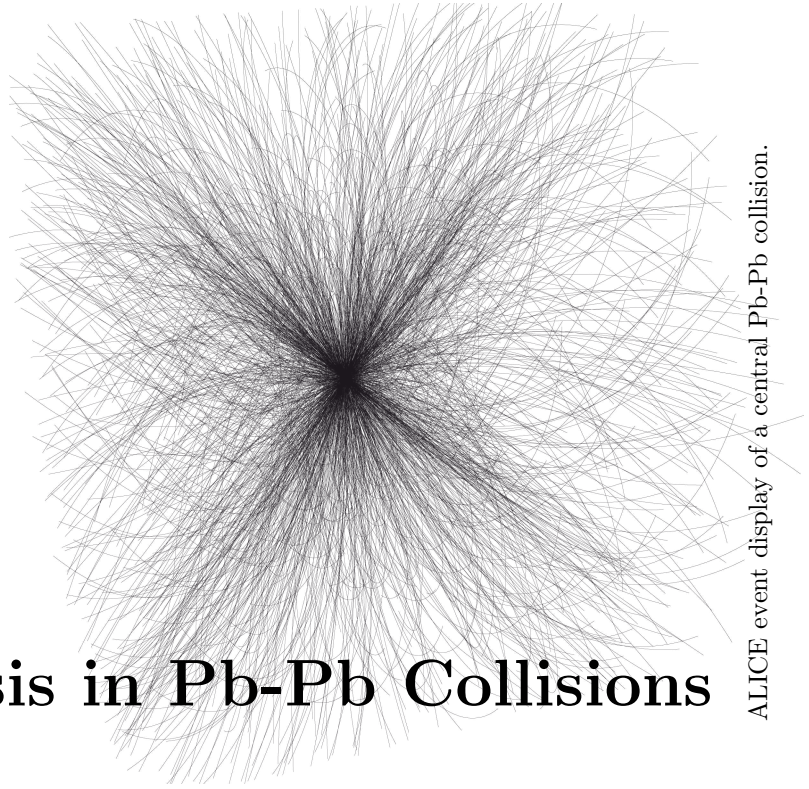
Figure 3.10.: The layout of the dielectron framework.

Chapter 4.

J/ψ Analysis in Pb-Pb Collisions

4.1. Data Samples

In ALICE the raw data collected by the detectors are stored in .root files. They are calibrated and reconstructed in a first reconstruction pass. The produced output, Event Summary Data files (ESD), has a dedicated structure and contains all necessary information for analysis and further tuning of the reconstruction. At the same time, a first set of Analysis Object Data files (AOD) with reduced content is produced. The AOD format is the recommended input for final analyses and approximately five times smaller in size. In this thesis, first an additional filter task with loose selection criteria is applied to the existing AOD data in order to reduce the input size even more (see Tab. 4.1) and speed up the train execution by reducing I/O operations and avoiding analysis of tracks and events of no interest. With these, so-called, nanoAODs one major technical problem in the background description with the event-mixing technique, see Sec. 4.3.3, was solved.

	Raw data	ESD	AOD	nanoAOD
Size (TB)	767.41	367.86	83.55	0.16

Table 4.1.: Different data formats in ALICE and their total size for Pb-Pb data taking period LHC11h.

4.1.1. Pb-Pb Data Sample

The data samples analyzed in this work are based on Pb-Pb collisions at $\sqrt{s_{\mathrm{NN}}}$ = 2.76 TeV provided by the LHC in fall 2011 and 2010. The integrated luminosity (see Eq. (3.1)) of these beam periods, LHC11h and LHC10h, correspond to $\mathscr{L}_{int}$ =24.34 ± 0.32(stat.) ± 1.89(syst.) and 2.04 ± 0.03(stat.) ± 0.16(syst.) µb^{-1}. In ALICE the 2011 data taking period contained three different trigger scenarios used in the Central-Barrel analysis. The two centrality triggers, *kCentral* and *kSemiCentral*, impose a minimum multiplicity threshold recorded by the V0 detector, while the minimum bias trigger, *kMB*, is a requirement based on the logical AND of the three following conditions:

- a signal in two readout chips in the outer layer of the SPD

- a signal in V0A

- a signal in V0C

Fig. 4.1 shows the event statistics versus multiplicity measured in the TPC collected by the different triggers after event quality cuts as described in Sec. 4.2.
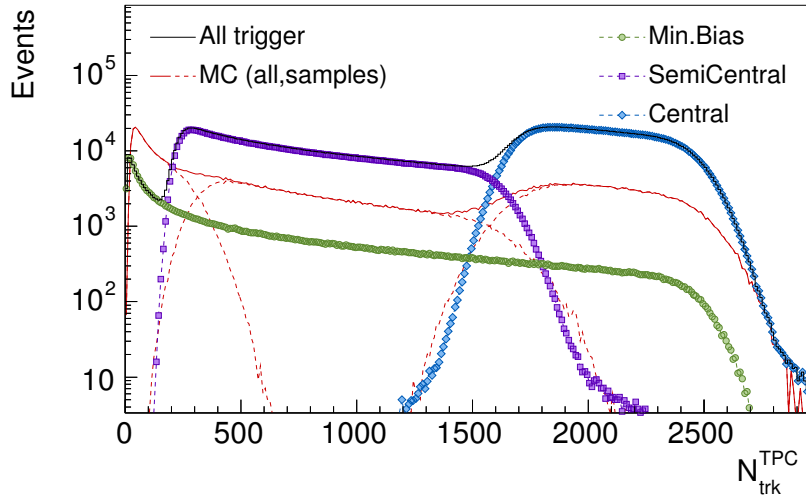

Figure 4.1.: The multiplicity distributions for the different trigger conditions in LHC11h compared to Monte Carlo simulations.

4.1.2. Monte Carlo Data Samples

There are several Monte Carlo simulations that can be used in the following analyses. The main differences between the MC simulations in ALICE are variations in the

kinematical distributions for the different particle species and further enrichments of certain, most often rare particles and decays. The MC productions are essential for the understanding of various detector effects and serve for the calculation of corrections, as described in Sec. 4.4. In each production exactly the same detector setup and configurations as in the anchor production LHC11h are applied in order to reproduce the running conditions and their effect on the corrections. The MC simulation used in this analysis (LC12a17g,h,i)[1] is divided into three sub-productions with the following centrality intervals: $(0 - 10\%),(10 - 50\%)$ and $(50 - 90\%)$. The multiplicity distributions are compared to the same in collision data in Fig. 4.1 and show a similar fractions of central, semi-central and peripheral events.

4.2. Run and Event Selection

The performance of ALICE during the 2011 Pb-Pb data taking is slighlty reduced due to hardware problems in the ITS and the inner and outer readout chambers (IROC and OROC) of the TPC. This results in unstable running conditions within beam period LHC11h, see Fig. 4.2. The operation efficiency obtained from clusters associated to tracks in the ITS and TPC as a function of the azimuthal angle ϕ and radius are shown in Fig. 4.3.

The Quality Assurance group provides a pre-selection of runs that are recommended for physics analyses based on their quality checks done in several steps of the reconstruction as described in Sec. 3.2.1. General issues of the calibration, alignment, track matching and particle identification are detected and tagged in the run condition table[112]. Corrections done in the offline reconstruction might not be accurate enough for analyses which rely on a high dE/dx resolution. Therefore, additional checks on the PID performance of the TPC are done, using a clean electron sample of photon conversion electrons, see Sec. 4.3.2. Eleven out of 108 runs were identified having a worse resolution and cannot be used properly without recalibration.

In this analysis only events were analyzed that are single Pb-Pb collision candidates at $\sqrt{s_{\mathrm{NN}}} = 2.76$ TeV. In order to ensure a good reconstruction quality and the rejection of background and pileup events, the centrally provided event selection was applied. Collision candidates were selected for the configured trigger mask mentioned above.

---

[1]In the analysis of 40-90% most central events of the data taking period LHC10h, the MC production LHC11a10*b*bis is analyzed.
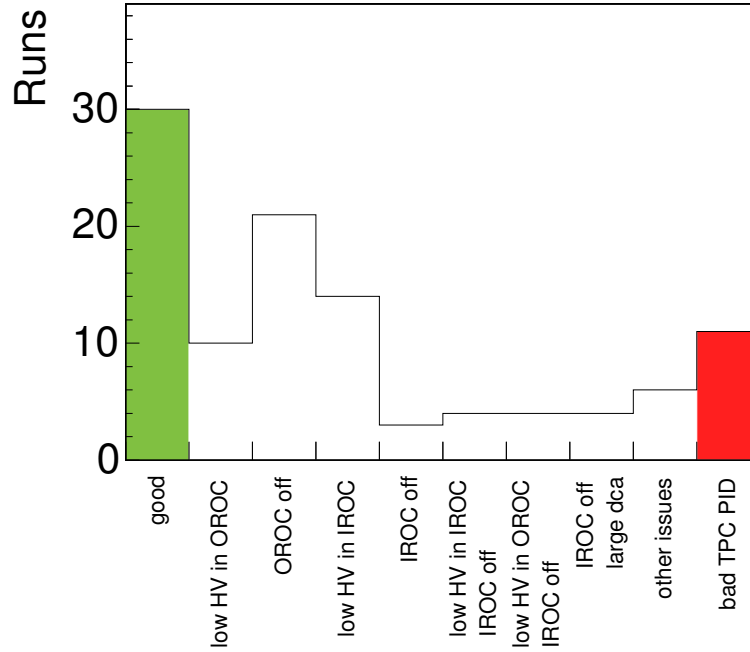
Figure 4.2.: The different running conditions of TPC in the Pb-Pb data taking period LHC11h.

(a) Inner Tracking System   **(b)** Time-Projection Chamber
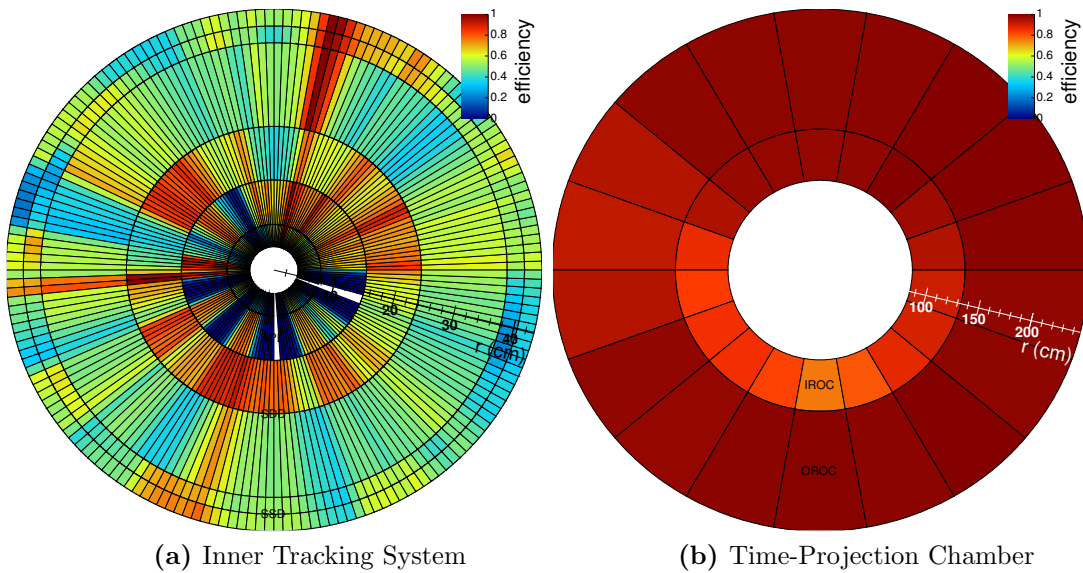
Figure 4.3.: The operation efficiency of the ITS and TPC in LHC11h as a function of the azimuthal angle and radius.

Furthermore only events with a well reconstructed primary vertex position along beam-axis ($\mathrm{vtx}_z < \pm 10$ cm) were accepted to avoid asymmetric geometrical acceptances for

detectors close to the nominal interaction point. The vertex distribution in Fig. 4.4b is centered at $\langle z \rangle = -0.13$ cm with a $\sigma_z = 5.09$ cm as expected from $\sigma_z = \sigma_b/\sqrt{2} = 5.34$ cm, where $\sigma_b = 7.55$ cm is the nominal bunch length provided by the LHC. The distributions for the central and semi-central triggers feature a drop outside the selected region. For these two triggers an online selection of the z-position of the primary vertex, provided by the T0 detector, was applied after $\approx 50\%$ of the data taking period. By this the storage and reconstruction of events that will be anyhow discarded at the analysis level was avoided. The vertex distributions in all cartesian coordinates are compared to Monte Carlo simulations, see Fig. 4.4. In MC, the primary vertex smearing for the transversal coordinates was calculated with outdated beam conditions[2], therefore the beam size is not correctly reproduced. The structure seen in the y-coordinate is related to the change of the magnet field polarity during the data taking and is well described by a double Gaussian.
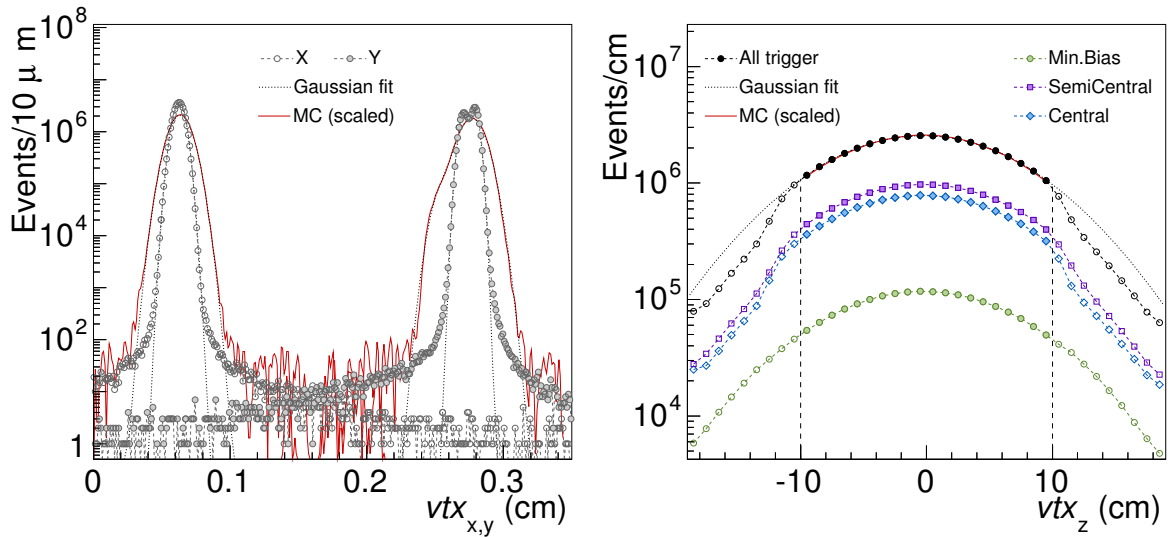
(a) Transversal coordinates, vtx_x and vtx_y, after vtx_z-selection.

(b) The vertex position in beam direction for the different trigger conditions. The vertical, dashed lines indicate the selection criterion.

Figure 4.4.: The distribution of the primary vertex position in data and MC after physics selection for the three cartesian coordinates.

---

[2]The beam size can be expressed in terms of the transverse emittance, ϵ_n and the amplitude function β^* at the IP. In the heavy-ion run during fall 2010, the LHC provided beams with $\epsilon \approx 3.75$ mm and $\beta^* \approx 3.5$ m, while for LHC11h it was reduced to $\epsilon_n \approx 1.5$ mm and $\beta^* \approx 1.5$ m.

4.2.1. Centrality Determination

The geometry of heavy-ion collisions can be characterized by the collision centrality determined via the impact parameter b as illustrated in Fig. 4.5. The collision centrality $\mathscr{C}$ is defined as the percentage of the total hadronic interaction cross-section $\sigma_{\text{A-A}}$ given in Tab. 3.1 and calculated by integration over the impact parameter distribution.
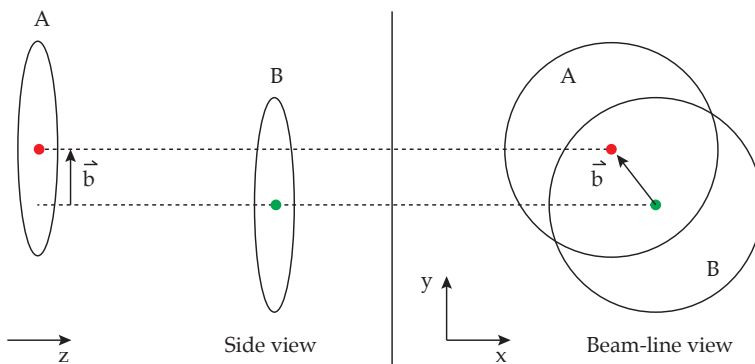

Figure 4.5.: Schematic view of a semi-central heavy-ion collisions.

$$\mathscr{C}(b) = \frac{1}{\sigma_{\text{A-A}}} \int_0^b \frac{\mathrm{d}\sigma_{\text{A-A}}}{\mathrm{d}b'} \mathrm{d}b' \tag{4.1}$$

In this work the globally provided centrality determination is utilized, which is described in detail in [92]. The charged particle multiplicity distribution measured at mid-rapidity, the longitudinal energy carried by the beam spectators detected by the zero-degree-calorimeters or any hit multiplicity recorded by a detector is connected to the nuclear overlap of two colliding nuclei T_{AA} calculated in a MC Glauber simulation. As a consequence, the measured multiplicity $\mathrm{d}N_{\text{ch}}/\mathrm{d}\eta$ can be related to an average impact parameter $\langle b \rangle$, number of binary collisions $\langle N_{\text{coll}} \rangle$ and number of participants $\langle N_{\text{part}} \rangle$. Tab. 4.2 summarizes the results of the centrality analysis in the intervals of interest for this work, together with the amount of data analyzed. The centrality distribution used in this analysis is shown in Fig. 4.6 for the different multiplicity trigger and corresponds to the estimation via the V0 amplitude that has the best resolution (0.5% (central) to 2% (peripheral)) [92].
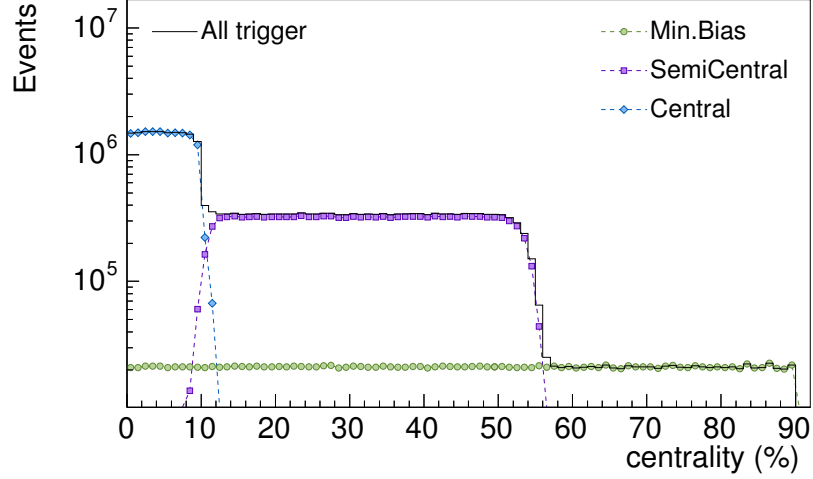
Figure 4.6.: Centrality distribution obtained with the V0 detector for the different trigger conditions in LHC11h.

Centrality $\mathscr{C}$	$\mathrm{d}N_{\mathrm{ch}}/\mathrm{d}\eta\,|_{|\eta|<0.5}$	$\langle N_{\mathrm{part}}\rangle$	$\langle T_{\mathrm{AA}}\rangle$ (mb^{-1})	$N_{\mathrm{evt}}(\times 10^6)$	$\mathscr{L}_{int}$ ($\mathrm{\mu b}^{-1}$)
0-10%	1447.5 ± 54.8	356 ± 4	23.5 ± 0.8	18.7	24.34 ± 1.92
10-40%	680.3 ± 26.6	192 ± 3	9.38 ± 0.37	14.0	6.04 ± 0.48
40-90%	$>130.2\pm5.9$	37.9 ± 1.2	0.985 ± 0.051	7.8	2.04 ± 0.16
0-40%	872.1 ± 35.8	233 ± 4	12.88 ± 0.46	32.7	24.34 ± 1.92

Table 4.2.: The charged-particle density [113], number of participating nucleons, average T_{AA}, number of events and the corresponding integrated luminosity for the centrality ranges used in this analysis.

4.2.2. Event-Plane Reconstruction

The spatial anisotropy of the initial energy density distribution in heavy-ion collisions translates into azimuthal anisotropies of the charged particle emission in the momentum space due to different pressure gradients. The azimuthal particle distribution $\mathrm{d}N/\mathrm{d}\phi$ w.r.t. the reaction plane Ψ^{R} can be expressed by a Fourier series as introduced in [114, 115]:

$$\frac{\mathrm{d}N}{\mathrm{d}\phi} = \frac{N_0}{2\pi}\left(1 + 2\sum_{n=1}^{\infty} v_n \cos(n(\phi - \Psi_{\mathrm{n}}^{\mathrm{R}}))\right), \tag{4.2}$$

where N_0 is the average particle yield, v_n is the flow magnitude and $\Psi_{\mathrm{n}}^{\mathrm{R}}$ the corresponding angle of the reaction plane of n-th order anisotropy. The flow moments depend on p_{T}, y

and collision centrality, and are usually referred to as radial v_1, elliptic v_2, triangular v_3 flow, as well as higher harmonics. An estimation of the reaction-plane orientation, was thought to be given by the event-plane method formulated by [114]. By construction, the event-plane angle Ψ points towards the maximum p_T and in presence of fluctuations does not necessarily coincide with the real reaction-plane. In the event-plane method, jet biases are significantly reduced by a transverse momentum limit in the track based reconstruction of Ψ and further biases due to fluctuations are taken into account in the calibration, see Sec. 4.2.2. The event plane angle is calculated from the flow vector $\overrightarrow{Q_n}$ for the n-th order harmonic:

$$\overrightarrow{Q_n} = \begin{pmatrix} X_n \\ Y_n \end{pmatrix} = \begin{pmatrix} \sum_i^{N_{\mathrm{ref}}} w_i \cos(n\phi_i) \\ \sum_i^{N_{\mathrm{ref}}} w_i \sin(n\phi_i) \end{pmatrix}, \tag{4.3}$$

where N_{ref} corresponds to the number of reference particles or detector readout pads and the weights w_i are set to unity in the ideal case of infinite N_{ref} and a high, uniform angular resolution. The weighting used in this work is described in the following calibration section. According to [115], the event plane orientation of the n-th order anisotropy can be calculated from the flow vector, see Eq. (4.4). Usually, the same harmonic n is used in the event-plane determination and in the flow measurement.

$$\Psi_n = \frac{1}{n} \tan^{-1} \left(\frac{Y_n}{X_n} \right) \tag{4.4}$$

In this work several detectors have been used for the determination of the event plane. Their different pseudo-rapidity coverages are summarized in Tab. 4.3 and can be used for comparison and event plane resolution calculations.

detector	η range	position resolution $\sigma(r\phi)$	$N_{\mathrm{ch}}/N_{\mathrm{ch}}\big|_{|\eta|<y_{\mathrm{beam}}}$
TPC	$|\eta| < 0.8$	$0.8 - 1.1$ mm	$\approx 15\%$
V0C	$-3.7 < \eta < -1.7$	$4.83 - 21.57$ cm	$\approx 18\%$
V0A	$2.8 < \eta < 5.1$	$4.97 - 27.11$ cm	$\approx 16\%$

Table 4.3.: Event-plane detectors with their corresponding pseudo-rapidity ranges, position resolutions and the fraction of charged particles seen by the detector [90, 92].

For Central-Barrel analyses the event plane obtained via the V0 detectors are preferred since non-flow contributions are significantly suppressed due to the separation in pseudo-rapidity by at least one unit. The event plane measured via the TPC was corrected for auto-correlations by removing the flow vector $\overrightarrow{Q}$ contributions of tracks coming from reconstructed J/ψ candidates. For the analysis of particles coming from the fireball the determination of the TPC event plane angle and magnitude might be favorable since they see the same phase space.

Even though the charged particle multiplicity in Pb-Pb collisions it approximately the same for the three event plane detectors a difference in the resolution of the event plane orientation is expected due to their position resolutions (see Tab. 4.3).

Event-Plane Calibration

The event plane orientation Ψ_n is calculated via the flow vector $\overrightarrow{Q}_n = (X_n, Y_n)$ according to the definitions given in Eqs. (4.3) and (4.4). While the V0 event planes are reconstructed via the average of the transverse position of each scintillator array weighted by its amplitude, the TPC event plane is calculated from the ϕ angle of tracks passing several quality cuts. For a full acceptance detector which is perfectly calibrated and has a high-granularity in the azimuth, the Q-vector components X_n, Y_n should be symmetrically distributed around zero and therefore the event plane should be uniform. All non-uniformities arise from azimuthal efficiency and acceptance effects in the detector and are corrected in the following steps.

In the TPC, reconstruction inefficiencies, due to imperfect calibration or dead zones, are corrected run-wise by weighting each track according to its ϕ and p_T, see Eq. (4.5). These weights are determined from the inverse of the azimuthal distribution of reference particles with given charge and pseudo-rapidity (positive or negative). Tracks with $p_T > 20$ GeV/c are excluded from the event-plane calculation in order to avoid biases by jets. Further fluctuations by high-p_T tracks are reduced by assigning a common weight:

$$w(\phi, p_T) = \left(\frac{N_{\text{ref}}(\phi)}{\langle N_{\text{ref}} \rangle} \right)^{-1} \cdot \begin{cases} p_T & p_T < 2 \text{ GeV}/c \\ 2 & 2 < p_T < 20 \text{ GeV}/c \\ 0 & p_T > 20 \text{ GeV}/c \end{cases} \quad (4.5)$$

Fig. 4.7a shows the mean position and RMS of the X_n and Y_n components after reweighting as a function of the collision centrality. Clearly, the distributions are not symmetric

around zero, which is reflected in the TPC event plane distribution shown in Fig. 4.7b for almost 30% of all runs. As a consequence a recentering according to Eq. (4.6) is applied leading to a flat distribution as is necessary.

$$\overrightarrow{Q_n}^{\text{corr}} = \begin{pmatrix} X_n^{\text{corr}} \\ Y_n^{\text{corr}} \end{pmatrix} = \begin{pmatrix} (X_n - \langle X_n \rangle)/\text{RMS}(X_n) \\ (Y_n - \langle Y_n \rangle)/\text{RMS}(Y_n) \end{pmatrix}, \qquad (4.6)$$
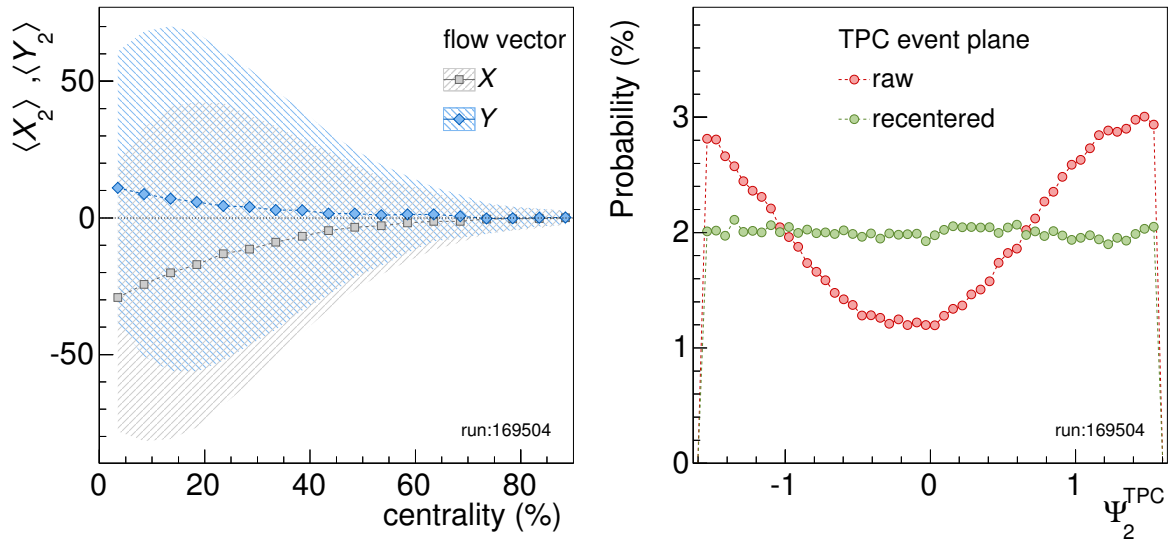
(a) $\langle X_n \rangle$, $\langle Y_n \rangle$ and RMS (X_n), RMS (Y_n).

(b) Ψ_2^{TPC} distribution.

Figure 4.7.: Left: The average (position) and RMS (errors) of the X_n-,Y_n-distributions as a function the collision centrality for run 169504. Right: The TPC event plane angle distribution, before and after recentering integrated over all centralities.

Signals in each cell of a given V0 ring were normalized to the average signal over all cells in the corresponding ring. By this, equal multiplicities in the azimuth were obtained on a run-by-run basis. The equalization is not fully sufficient in order to obtain a flat event plane distribution, since its does not take into account misalignment and acceptance-related effects between the cells of different V0 rings. Therefore further flattening of the V0 event plane was done following multiple techniques (recentering, twisting, rescaling) discussed in the approach by [116]:

$$\overrightarrow{Q_n} = \begin{pmatrix} \langle X_n \rangle + A_n^+ (\cos(n\Psi_n) + \Lambda_n^+ \sin(n\Psi_n)) \\ \langle Y_n \rangle + A_n^- (\sin(n\Psi_n) + \Lambda_n^- \cos(n\Psi_n)) \end{pmatrix} \qquad (4.7)$$

The flattening parameters $\langle X_n \rangle, \langle Y_n \rangle$, A_n^+, A_n^-, Λ_n^+ and Λ_n^- were extracted from the mean and RMS of the X_n, Y_n and $X_n \cdot Y_n$ distribution. These parameters show a small centrality dependence which was taken into account. Finally, residual fluctuations in the event plane distribution, which arise from the azimuthal segmentation of the V0 sectors, were corrected by the so called Fourier flattening technique [117]. There the 4th Fourier moment of the event plane distribution, $\langle \sin(2 \cdot 4\Psi_2) \rangle$ is used as a single parameter. This part of the correction exhibits significant impact only at centralities $> 60\%$.

Event-Plane Resolution

Any measured event anisotropy is smeared out by the dispersion χ of event plane estimate. The event plane resolution can either be determined analytically via the relation between resolution and dispersion using Bessel functions I of the first and second order [114, 118]:

$$R_n(\chi) = \frac{\sqrt{\pi}}{2} \chi \exp\left(-\frac{\chi^2}{2}\right) \times \left(I_0\left(\frac{\chi^2}{2}\right) + I_1\left(\frac{\chi^2}{2}\right)\right) \tag{4.8}$$

or, as done in practice, the resolution is determined via two or three (sub)detectors. If the two detectors A, B are identical in terms of N_{ref} and pseudo-rapidity range (symmetric around mid-rapidity), then the resolution is given by:

$$R_n^A = \sqrt{\langle \cos(n(\Psi_n^A - \Psi_n^B)) \rangle} \tag{4.9}$$

For the case, one of the two conditions is not fulfilled, a third detector C is needed and the resolution for A can be calculated via the correlations between the detectors:

$$R_n^A = \sqrt{\frac{\langle \cos(n(\Psi_n^A - \Psi_n^B)) \rangle \langle \cos(n(\Psi_n^A - \Psi_n^C)) \rangle}{\langle \cos(n(\Psi_n^B - \Psi_n^C)) \rangle}} \tag{4.10}$$

The event plane resolution varies for the event plane detectors due to their differences in the position resolution and geometrical acceptance, see Tab. 4.3. A large event plane resolution factor, shown in Fig. 4.8, corresponds to a better resolution, being perfect for $R = 1$. The best resolution is reached with the TPC, followed by the V0C and the V0A detectors. Furthermore a change with the event centrality can be seen, since the event plane angle can be best determined for semi-central collisions where the elliptic flow is largest. The more isotropic the azimuthal event shape is, the more difficult is the extraction of the event plane angle. Qualitatively, the observed shape can be explained

by the dispersion $\chi = \langle v_2 \rangle \sqrt{N_{ch}}$, where the measured charged particle v_2 [119] and the average number of tracks per centrality in the pseudo-rapidity range was used.
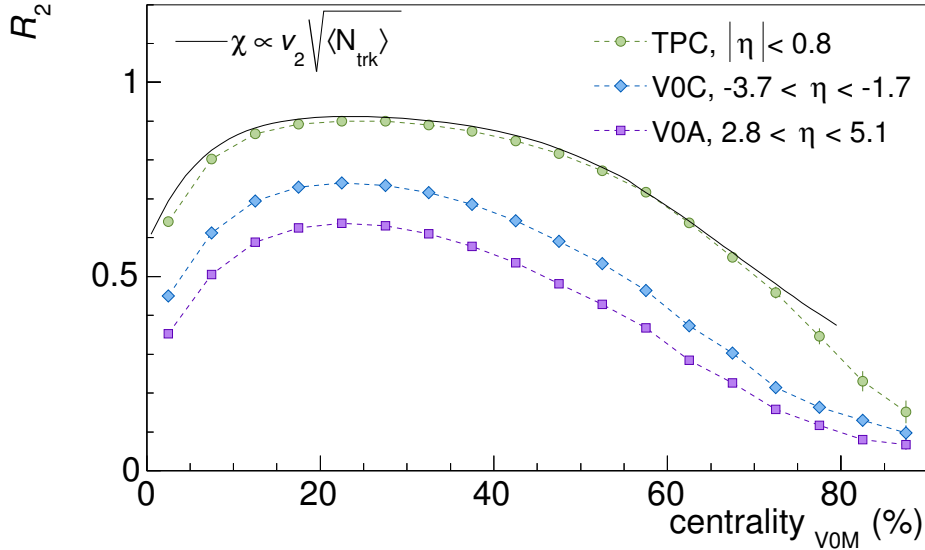

Figure 4.8.: The centrality dependence of the second-order event plane resolution from three-detector subevent correlations for the different detectors used in the analysis. The solid curve corresponds to the resolution obtained via the dispersion relation using existing measurements of the charged-particle v_2 and the mean multiplicity.

4.3. J/ψ Reconstruction

In the following sections all events are used to reconstruct the particle candidates for the electromagnetic decay channel $J/\psi \to e^+e^-$. Several kinematical and quality selections as well as particle identification procedures are applied in order to select primary electron candidates. In particular for Pb-Pb collisions it is important to reduce the background by efficiently rejecting misidentified electrons and secondary electrons from photon conversions in the detector material. The invariant mass for all electron-positron pairs of the remaining candidates is reconstructed. In the obtained spectrum the J/ψ yield can be extracted using various methods for the description of the background.

4.3.1. Track Selection Quality Criteria

The total amount of tracks can be significantly decreased by selecting only tracks with a minimum transverse momentum $p_T > 0.85$ GeV/c. Such a kinematical rejection reduces the amount of electrons originating from an low momentum photon or π^0 and Bremsstrahlung. Since the J/ψ decay into electrons leads to relatively large daughter momenta in the laboratory frame, only little J/ψ signal is lost. A geometrical limitation for the tracks is given by the particle identification coverage of the TPC. Tracks within the polar angle $48^o < \theta < 132^o$, corresponding to a pseudo-rapidity interval $|\eta| < \pm 0.8$, provide the highest tracking and PID efficiency for electrons, since they traverse the full volume of the TPC.

The following track cuts were applied in order to ensure a good quality of the reconstructed tracks. Secondary J/ψ from beauty decays are produced on average ≈ 0.5 mm away from the production vertex. Thus, the removal of secondary particles has to be loose enough to not exclude the non-prompt part of the inclusive J/ψ measurement. However, the rejection of secondary particles and tracks from background and potential pileup collisions is crucial, because the combinatorical background scales with $\binom{n}{2}$.

Impact Parameter: The impact parameters in the transversal and longitudinal direction can be calculated for each track as the distance of closest approach (dca) to the primary vertex. An upper limit was defined as $|dca_{xy}| < 1.0$ cm and $|dca_z| < 3.0$ cm in order to predominantly select primary particles. Here the worse impact parameter resolution in the z-coordinate (≈ 170 µm at $p_T = 1$ GeV/c) compared to the transverse plane ($\Delta dca_{xy} = 65$ µm) was taken into account, see [90, 120]. Fig. 4.9 shows the dca distributions for all electron candidates in collision data with their origin obtained via MC simulation. The fraction of primary particles is about 90%, while there is still 10% secondary particle contamination from material and weak decays of strange particles.

SPD Hit Requirement: A very powerful cut to reduce the contribution from secondary electrons is the requirement of having at least a single cluster in one of the first two layers of the SPD associated to the track. In the Pb-Pb data taking period only $57.5 - 65\%$[3] of the SPD modules were operating which prevents an improved background reduction without significant loss of J/ψ signal. Fig. 4.10a shows the first hit in the ITS detector layer of all tracks in positive and negative pseudo-rapidity. A weak dependence is found that can be explained by the difference in the number of

---

[3]For LHC10h the fraction of active supermodules was $70 - 77.5\%$.

(a) Transversal impact parameter   **(b)** Longitudinal impact parameter
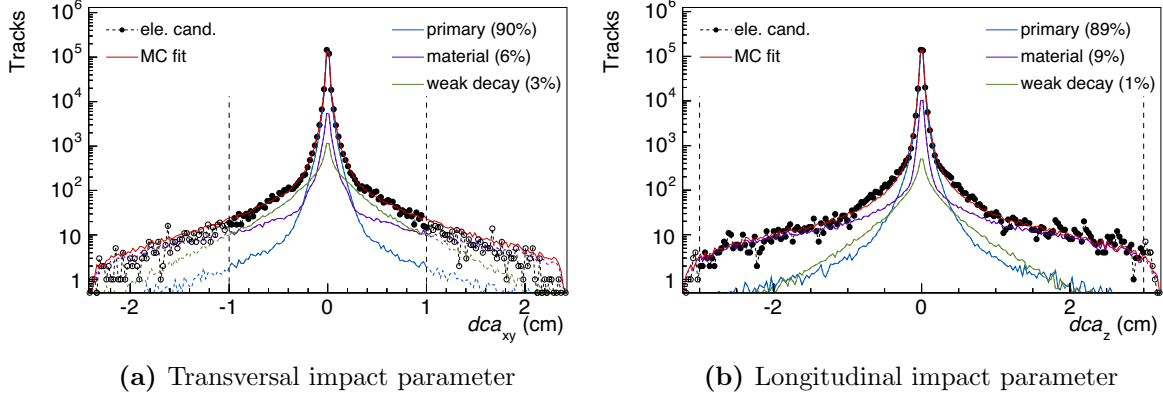
Figure 4.9.: The impact parameter distributions for data and MC.

active SPD modules. A requirement only based on SPD would reduce the statistics and lead to strong event deformity in the azimuth and polar angle, which could bias e.g. elliptic flow measurements. According to this a multidimensional requirement (ϕ,η and time (run number)) based on the three innermost layers of the ITS was applied to the tracks to obtain the best background rejection by largest acceptance. Since the SPD is the fastest detector used in the Central-Barrel, a requirement can also minimize the contribution of tracks belonging to other events (pileup).

ITS Tracking: For all particles the tracking status bit ITSrefit evaluated in the track reconstruction is required. The bit is enabled when the final inward fit by the Kalman filter was successful. This naturally implies a minimum numbers of two clusters in the six silicon layers of the ITS.

TPC Tracking: A good track reconstruction in the TPC can be ensured by the number of cluster associated to the track $N_{cls}^{TPC} > 70$ and an upper limit of the fit quality[4], expressed in terms of $\chi^2/ndf < 4$. The heterogeneous TPC high voltages between chambers and different sectors, seen in Fig. 4.2, calls for a quantification of the track quality depending on the number of active regions in the TPC. Therefore the 159 pad rows of the TPC were divided into eight segments covering each an interval of 20 consecutive rows. A track segment was assumed to be active if the number of found clusters inside was above five. By this, the requirement on the number of active TPC segments $N_{seg}^{TPC} > 6$ ensures a uniform distribution of clusters along the track. In addition, an successful TPCrefit for all tracks was requested.

---

[4]The χ^2/ndf of the fit in TPC is a measure for the distance of the clusters to the fit, where the number of degrees of freedom is $2 \cdot N_{cls}^{TPC} - 5$ (the five fit parameter: vtx_y, vtx_z, $\sin(\phi)$, p_z/p_T, $\pm 1/p_T$)

(a) ITS layer of first cluster.

(b) Number of ITS clusters.
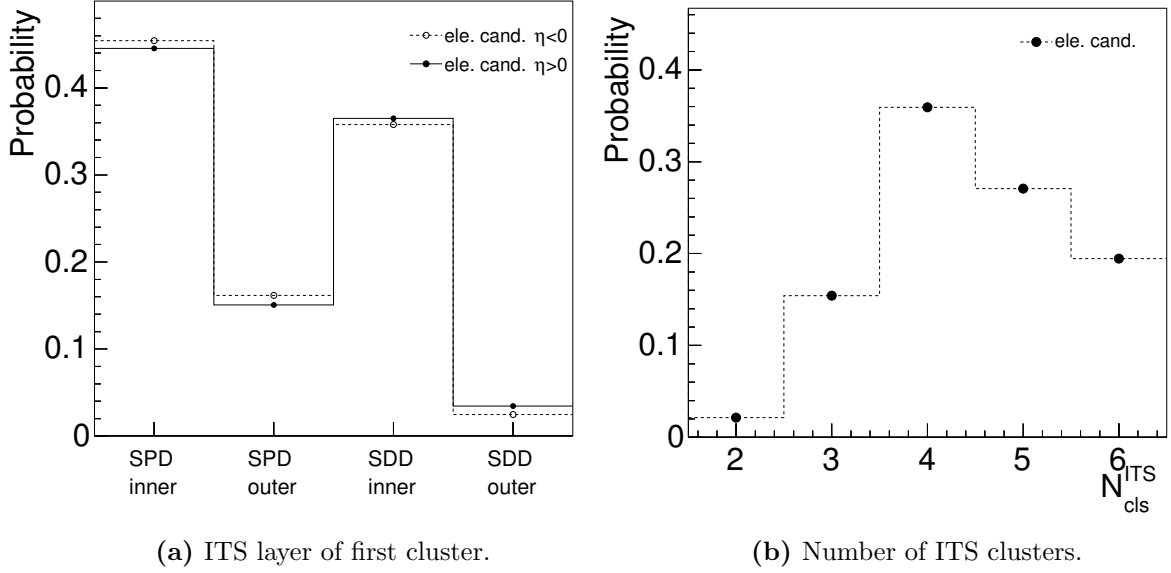
Figure 4.10.: The ITS track quality distributions.

(a) Number of TPC cluster.

(b) TPC PID response for electrons.
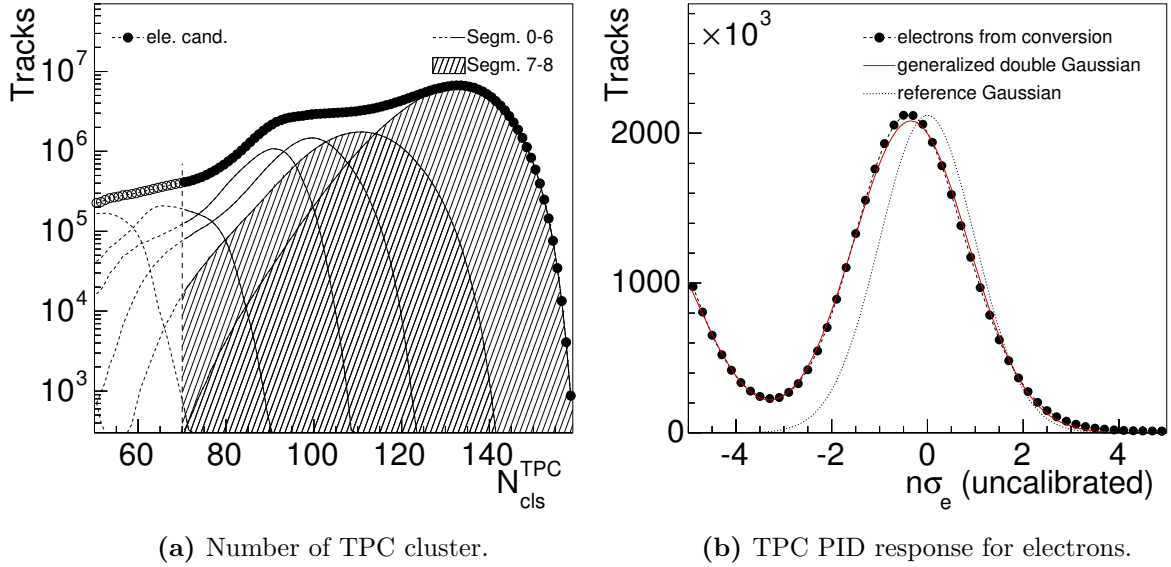
Figure 4.11.: Left: Distribution of the number of TPC cluster and segments per track. Selected track are indicated by a filled pattern. Right: The PID response in terms of $n\sigma_e$ for electron candidates from a sample of γ-conversions compared to a generalized Gaussian fit and the reference PID response.

4.3.2. Particle Identification

The particle identification performed in this analysis is based on the specific energy loss of the particles (dE/dx) in the TPC detector gas (see Eq. (3.2)). A selection of electron

candidates was applied based on the deviation of the measured TPC dE/dx from the Bethe-Bloch expectation in terms of the expected energy loss resolution σ_{exp}:

$$n\sigma = \frac{(dE/dx)_{meas} - (dE/dx)_{exp}}{\sigma_{exp}} \qquad (4.11)$$

The expected energy loss resolution σ_{exp} can be calculated according to Eq. (4.12), where the number of TPC clusters $N_{\mathrm{cls.PID}}^{\mathrm{TPC}}$ used for the dE/dx measurement is taken into account. The parameters Δ_σ and Δ_{cls} describe the relative dE/dx resolution and TPC cluster dependence and are determined during the TPC calibration. An average resolution $\langle\sigma_{exp}\rangle = 6.2\%$ [86] was found for central Pb-Pb collisions.

$$\sigma_{exp} = \Delta_\sigma \cdot (dE/dx)_{exp} \cdot \sqrt{1 + \Delta_{cls}/N_{\mathrm{cls.PID}}^{\mathrm{TPC}}} \qquad (4.12)$$

TPC Post Calibration

Due to the mentioned hardware issues in the TPC during data taking, many of these detector effects can alter the response of the TPC detector in terms of PID. A pure electron sample was used to monitor the compensation of these effects by the calibration. The electron sample was obtained from reconstructed photon conversions via their V^0 decay topology, $\gamma \rightarrow e^+e^-$. Since they can be identified without the use of TPC particle identification information, their decay products can quantify the PID performance of the TPC. As described in Sec. 4.3.1 the track reconstruction and particle identification are optimized for particles pointing to the primary vertex, such as electrons from J/ψ decays. Since photon conversion electrons mostly originate from materials far away from the primary collision vertex, special care must be taken when using them. The corresponding selection criteria are documented in App. A and are optimized such that the reconstruction properties of the electrons match to those of the electron candidates used in the J/ψ → e$^+$e$^-$ analysis.

The Gaussian distribution of the nσ for electrons, shown in Fig. 4.11b, is not centered at its ideal position zero with a width of one. Furthermore, the centroids and widths of the distributions vary with pseudo-rapidity, event multiplicity $N_{\mathrm{trk}}^{\mathrm{TPC}}$, centrality $\mathscr{C}$ and run number (see e.g. Fig. 4.12.

Tracks with larger pseudo-rapidity and therefore longer drift distances have worse dE/dx resolutions. The drift length is proportional to the number of TPC clusters used for

(a) Multiplicity dependence.
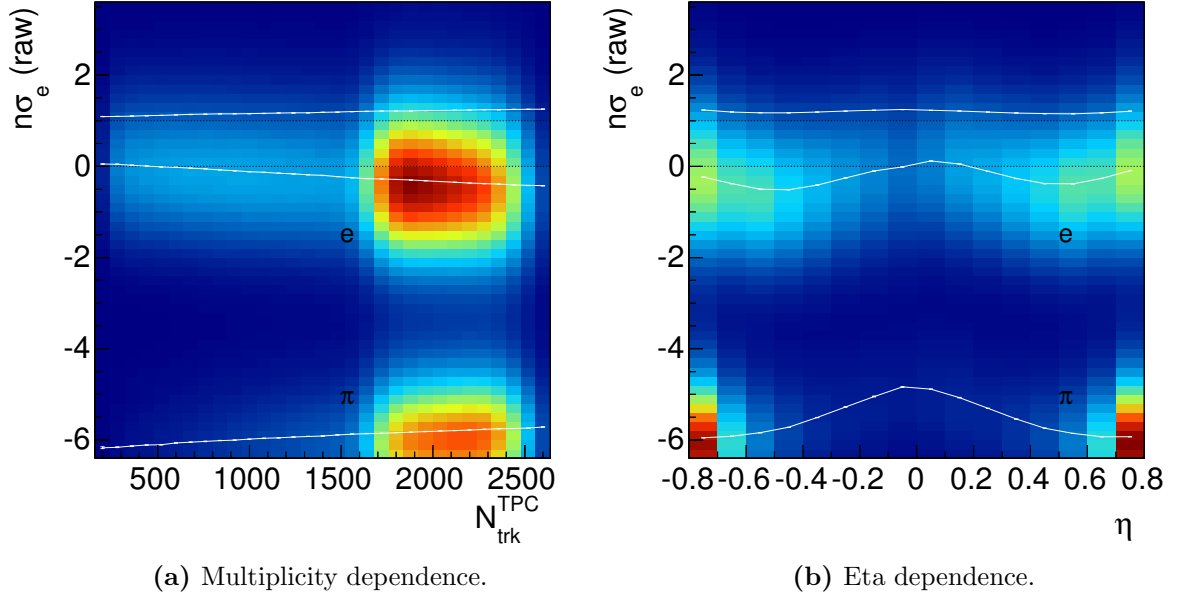
(b) Eta dependence.

Figure 4.12.: The TPC PID response for electrons versus the TPC multiplicity and the pseudo-rapidity. The black, dashed lines correspond to the expected centroid and width of the electron energy loss description.

dE/dx (see Eq. (4.12)). A change of the $n\sigma_e$ distribution with increasing event multiplicity indicates an occupancy effect of the TPC, that can even be seen for different event plane orientations. This results in a drop of the centroids σ_e^0 and in an decrease of the dE/dx resolution w with increasing multiplicity due to a loss of TPC clusters which are caused by so-called ion-tails of the signal readout as studied in [121]. With increasing multiplicity the separation power between electrons and pions gets worse, since the opposite trend for pions is observed.

All these detector effects were not properly taken into account during the calibration. Therefore a post calibration of the TPC PID response was performed. Fig. 4.13 shows the dependence of the fit parameters of a Gaussian fit to the distributions of $n\sigma_e$ from photon conversions in two dimensions. To get independent on the fit parameter fluctuations, which are mainly caused by statistics and the choice of the binning, a two dimensional fit was applied to the obtained parameters. The two dimensional fit is shown in Fig. 4.13. Its results are used to recalibrate the TPC electron PID response according to Eq. (4.13).

$$n\sigma_e^{cal}(\mathscr{C},\eta) = \frac{n\sigma_e(\mathscr{C},\eta) - n\sigma_e^0(\mathscr{C},\eta)}{w(\mathscr{C},\eta)} \qquad (4.13)$$
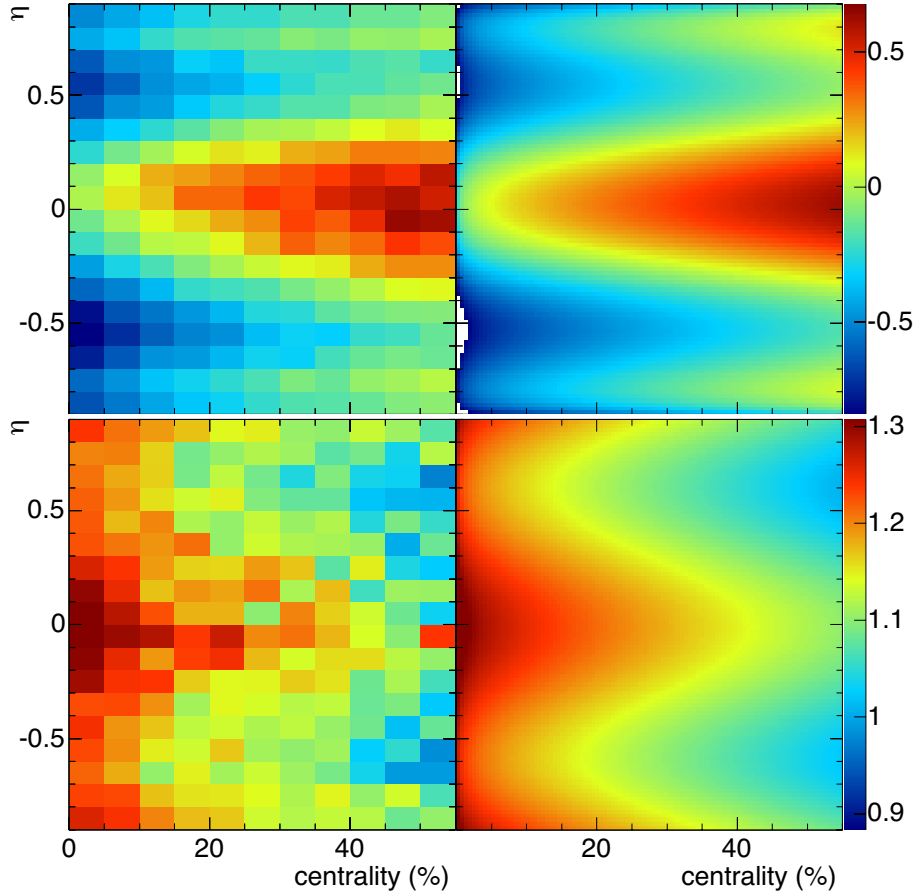
Figure 4.13.: Left: The post calibration parameters, centroids (top) and widths (bottom), obtained via generalized double Gaussian fits. Right: The corresponding two-dimensional fits on the parameter distributions (left) for further smoothing.

Electron Selection

After the post calibration of the TPC PID response is applied, a selection of electrons can be done by including particles around the electron expectation. As shown in Fig. 4.14 several particle species cross the electron band at different momenta. Therefore the selection cuts need to be optimal for high efficiency and low contamination. Due to the preceding cut on the transverse momenta at 0.85 GeV/c an exclusion of kaons and low momentum pions and muons was already done. Protons and deuterons are indistinguishable from electrons in the momentum regions where they cross the electron band. The crossing happens for protons at around $p = 1$ and 2 GeV/c for deuterons. This is important, since in this region most of the electron are selected. To reduce the contamination by protons only tracks are selected which are more than 4.0σ away from the proton expectation. The contribution of deuterons to the selected sample can be

neglected since their absolute amount is small enough. The main source of misidentified electrons are pions. A tighter electron selection at the lower bound of the inclusion band was used to reduce their impact. All PID selections are summarized in Tab. 4.4.
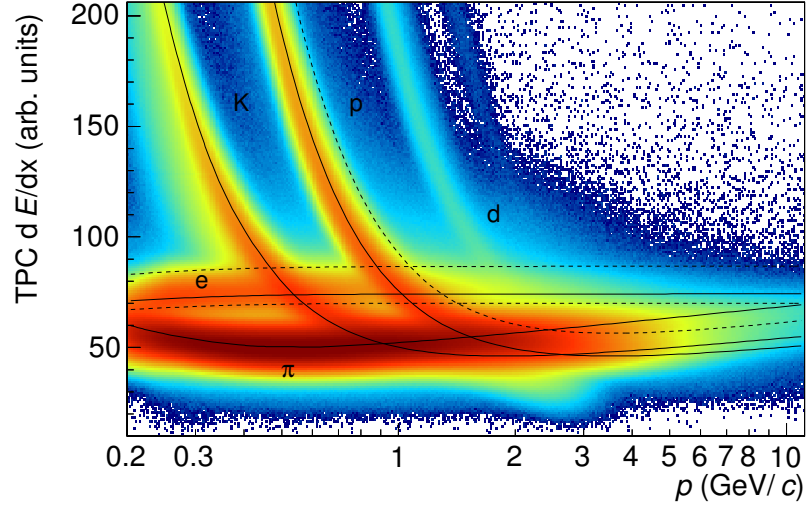
Figure 4.14.: dE/dx distribution of the TPC and the standard electron selection cuts (dashed lines).

Cut group	Description	Criterion
acceptance	transverse momentum	$p_T > 0.85$ GeV/c
	pseudo-rapidity	$|\eta| < 0.8$
reconstruction	impact parameter	$|dca_{xy}| < 1.0$ cm
		$|dca_z| < 3.0$ cm
	Kinks	no daughters
	reconstruction	ITS & TPC refit
	first hit in ITS	layer(ϕ) ≤ 3
		$\chi^2/$ndf < 4.0
	TPC tracking	cluster segments > 7
		cluster per track > 70
PID	electron inclusion	$-1 <$n$\sigma_e < 3$
	proton exclusion	n$\sigma_p > 4$

Table 4.4.: Track selection criteria in this analysis.

4.3.3. Background Estimation and Signal Extraction

After applying the selection criteria, explained in Sections 4.3.1 and 4.3.2 and listed in Tab. 4.4, to all tracks, the invariant mass of all opposite charged track combinations (OS) per event can be calculated according to Eq. (4.14). A two particle decay process of the J/ψ into electron and positron is assumed. The masses of the electrons can be safely neglected, since $m_{\mathrm{e}} \ll m_{\mathrm{J}/\psi}$.

$$m_{\mathrm{J}/\psi} = \sqrt{2 \cdot p_{\mathrm{T}}(\mathrm{e}^+) p_{\mathrm{T}}(\mathrm{e}^-)(\cosh(\Delta\eta) - \cos(\Delta\phi))} \qquad (4.14)$$

Fig. 4.15 shows the invariant mass spectrum in the range from $0 < M_{\mathrm{ee}} < 12$ GeV/c^2 for all events in the centrality intervals $0-10\%$, $10-40\%$, $40-90\%$ and the sum. Since the average number of electron candidates for events of interest is up to ≈ 10, large number of combinations are possible and therefore the J/ψ yield is not immediately visible in all intervals. The invariant mass spectrum is accordingly dominated by uncorrelated background of randomly combined electron candidates. Further components such as misidentified particles, mainly pions, and electrons from semileptonic decays of open-charm and open-beauty hadrons (each $\Gamma_{\mathrm{e+X}}/\Gamma_{\mathrm{tot}}=10\%$ [20]) contribute. Additionally, electrons originating from γ conversions and Dalitz decays (π^0,η,ω) populate the lower mass region of the spectrum.

In the following two different background estimators are described that are used in the extraction of the J/ψ signal.

Like-Sign Reconstruction

The Like-Sign technique (LS) is the most natural way to estimate the uncorrelated background. In addition to the calculation of unlike-sign pairs $N_\pm$, the like-sign pairs (N_{++},N_{--}) within the same event (SE) are combined and therefore provide the normalization by construction. The signal S can be obtained from the number of unlike-sign pairs in two ways:

$$S = N_\pm - R \cdot 2\sqrt{N_{++} \cdot N_{--}} \qquad \text{(geometric mean)} \qquad (4.15a)$$

$$S = N_\pm - R \cdot (N_{++} + N_{--}) \qquad \text{(arithmetic mean)} \qquad (4.15b)$$

(a) $e^+ e^-$ pairs for various centrality intervals.

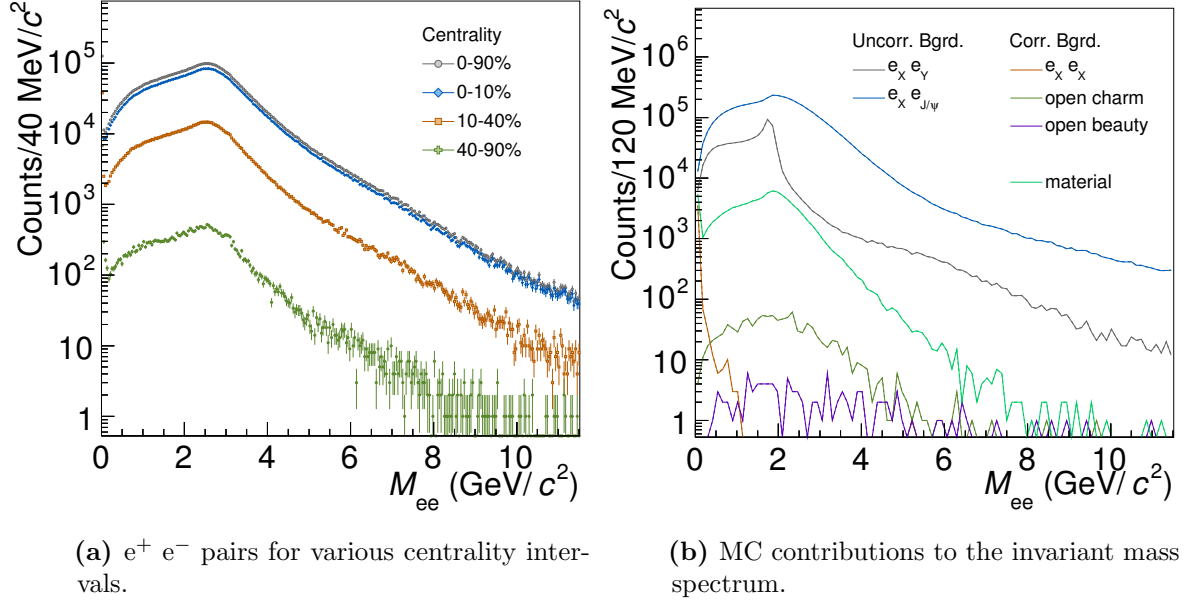**(b)** MC contributions to the invariant mass spectrum.

Figure 4.15.: The invariant-mass distribution of all opposite-charged electron pairs after all selection in collision and simulation data.

Only for very small and non-continuous background distributions the arithmetic mean normalization becomes relevant. The mass-dependent R-factor accounts for asymmetries in the production of positively and negatively charged particles and for effects due to acceptance biases relative to the particle charge. The mixed-event (ME) technique, described in the next paragraph, provides a data driven method to obtain these asymmetries as a function of the invariant mass (m):

$$R(m_{\mathrm{inv}}) = \frac{N_{+-}(m_{\mathrm{inv}})}{2\sqrt{N_{++}(m_{\mathrm{inv}}) \cdot N_{--}(m_{\mathrm{inv}})}} \tag{4.16}$$

Fig. 4.16 shows the like-sign estimation before (black) and after (red) R-factor correction. The magnitude of this correction saturates for $M_{\mathrm{ee}} > 3.5$ GeV/c^2 at 6%. Both spectra are scaled to match the unlike-sign distribution in the region from $3.2 < M_{\mathrm{ee}} < 4.2$ GeV/c^2 where no correlated background is expected (see Fig. 4.15). Since the ratio of $\psi(2S)/(J/\psi(1S))$ production in lead-lead collisions is of the order of 3% [73] and the statistics are low, the $\psi(2S)$ resonance will not bias the normalization done using this interval.

The residual difference in shape of the like-sign to the opposite-sign spectrum at low masses is possibly related to events with like-sign correlated particle pairs [122] and
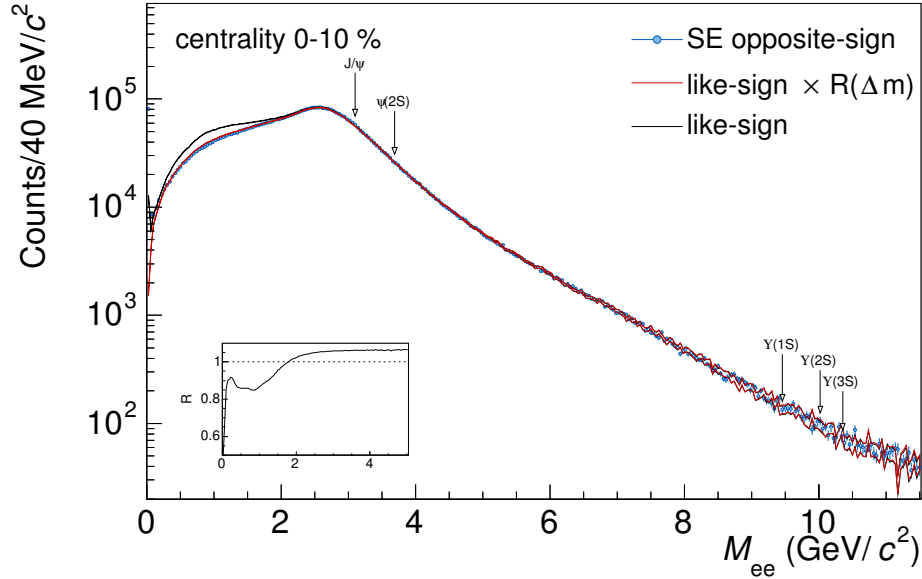
Figure 4.16.: The like-sign distribution for geometric normalization and R-factor correction.

supported by the correlated background contributions shown in Fig. 4.15. The like-sign method has the disadvantage that the statistical uncertainty of the background (B) is limited by the number of events and consequently contributes to the uncertainty of the extracted signal yield.

Mixed Event Generation

The mixed-event technique (ME) [123] provides a different way to estimate the uncorrelated background. The idea is to combine particles from different events ("event mixing") several times to estimate the background. Pairs from mixed events contain all information of the reaction and the experimental device except the correlation of interest. The number of events used for particle mixing determines the statistical precision and can be adjusted. If the resonance falls into the area where the whole invariant mass distribution peaks, it is rather difficult to find an analytic function to approximate the shape of the background, while for mixed events this is not an issue. In the course of this thesis, the mixed-event implementation into the dielectron framework was extended and studied in detail. A good description of the uncorrelated background with mixed events is found by combining only particles of events with similar global event properties, such as acceptance and multiplicity. Events are distributed over so-called event classes in bins of the primary vertex position vtx_z to account for acceptance effects and in bins of

centrality $\mathscr{C}$ for similar detector occupancy and track-density. In the presence of elliptic flow the event can either be rotated to a common event plane or grouped by the event plane angle Ψ_2. Due to the unstable running conditions of the Central-Barrel detectors, a rotation of events would lead to acceptance biases. According to Sec. 4.2.2 the TPC has the best event plane resolution and additionally the particles used in the invariant mass calculation experience the same environmental conditions. For each event the TPC event plane angle Ψ_2^{TPC} is calculated according to Sec. 4.2.2 and corrected for auto-correlations. The maximal resolution of $\Psi_2^{\mathrm{TPC}} \approx 10\%$ defines the granularity of the mixing categories in this dimension. All event classes are summarized in Tab. 4.5 and their distribution is shown in Fig. 4.17 together with the underlying distributions for $\mathscr{C}$, Ψ_2^{TPC}, vtx_z.

Category	Binning
vtx_z (cm)	$-10, -5, -4, -3, \ldots, +5, +10$
$\mathscr{C}$ (%)	9 bins in $(0 - 90)$
Ψ_2^{TPC}	10 bins in $(-\pi/2 - +\pi/2)$

Table 4.5.: Event mixing categories.
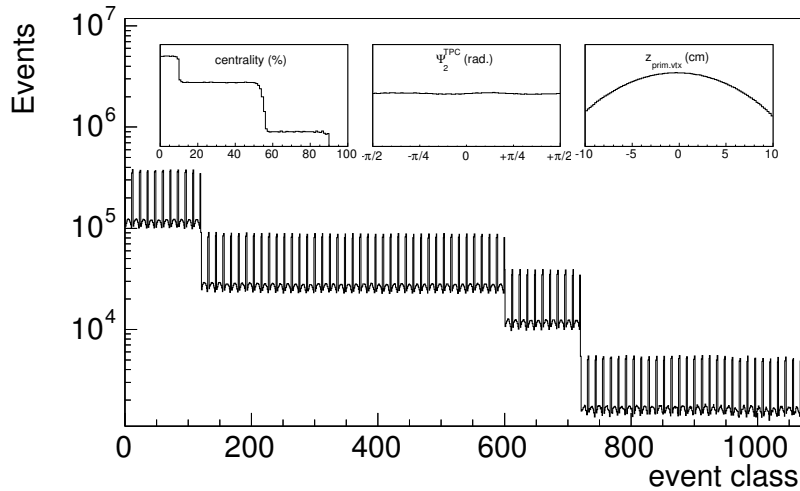
Figure 4.17.: The convolution of the category distributions (sub panels) to the event class distribution. The small peaks are caused by the first and last large bin in the vtx_z category, while the step between 600-800 is due to the trigger inefficiencies and corresponds to the centrality interval $50 - 60\%$.

Since the granularity (1080) of event classes to describe the background is rather high, the processing of the data needs to be done with a large number of events to ensure

enough event mixing statistics for all event classes. A solution for this technical issue is found in the usage of the introduced nanoAODs, which is the major argument for their production besides the speed-up of data processing. On top of this, the event mixing needs to be done run-wise (97 runs) to separate mixed events by different running conditions of the ALICE detector[5].

The event mixing configuration is chosen such that the statistical uncertainty is negligible $\sqrt{N_{\mathrm{ME}}}/N_{\mathrm{ME}} \ll 1\%$. Finally, the normalization of the ME distributions to the SE spectrum is done by matching for each event category the integrals of the two invariant mass distributions in the regions, $1.5 < M_{\mathrm{ee}} < 2.5$ GeV/c^2 and $3.2 < M_{\mathrm{ee}} < 4.2$ GeV/c^2:

$$B_{\mathrm{ME}}(m_{\mathrm{inv}}) = \sum_{\mathrm{vtx}_z} \sum_{\mathscr{C}} \sum_{\Psi} N_{\mathrm{ME}}(\mathrm{vtx}_z, \mathscr{C}, \Psi, m_{\mathrm{inv}}) \times \omega(\mathrm{vtx}_z, \mathscr{C}, \Psi)$$

$$\omega(\mathrm{vtx}_z, \mathscr{C}, \Psi) = \frac{\sum_{m_{\mathrm{inv}}=1.5}^{2.5} N_{\mathrm{SE}}(\mathrm{vtx}_z, \mathscr{C}, \Psi, m_{\mathrm{inv}}) + \sum_{m_{\mathrm{inv}}=3.2}^{4.2} N_{\mathrm{SE}}(\mathrm{vtx}_z, \mathscr{C}, \Psi, m_{\mathrm{inv}})}{\sum_{m_{\mathrm{inv}}=1.5}^{2.5} N_{\mathrm{ME}}(\mathrm{vtx}_z, \mathscr{C}, \Psi, m_{\mathrm{inv}}) + \sum_{m_{\mathrm{inv}}=3.2}^{4.2} N_{\mathrm{ME}}(\mathrm{vtx}_z, \mathscr{C}, \Psi, m_{\mathrm{inv}})}$$

$$(4.17)$$

This guarantees a proper weighting of the different event classes and a good matching between SE and ME. Fig. 4.18 shows the like- and unlike-sign invariant mass distributions after the matching. A reasonable agreement with the SE-distribution is found over a broad range and down to $M_{\mathrm{ee}} \approx 1$ GeV/c^2.

4.3.4. Yield Extraction

In this thesis the mixed-event technique is chosen as the standard method for signal extraction. A J/ψ signal can be extracted in three centrality intervals $(0 - 10\%)$, $(10 - 40\%)$ and $(40 - 90\%)$ with reasonable significances $(S/\sqrt{S+B} > 6)$. For the most peripheral interval, Pb-Pb events of the 2010 data taking (LHC10h) are analyzed, since the amount of minimum bias events recorded in 2011 is too low for a stable signal extraction. Details on the 2010 data analysis can be found in App. B. Fig. 4.19 shows the invariant mass distribution for the three centrality intervals and the decrease of the background towards lower collision centrality. In all cases the background description by the mixed-event technique is sufficient to extract the J/ψ yield in the invariant mass

---

[5]This is not necessary for LHC10h data, since there the running condition are reasonably stable in terms of ITS and TPC performance.
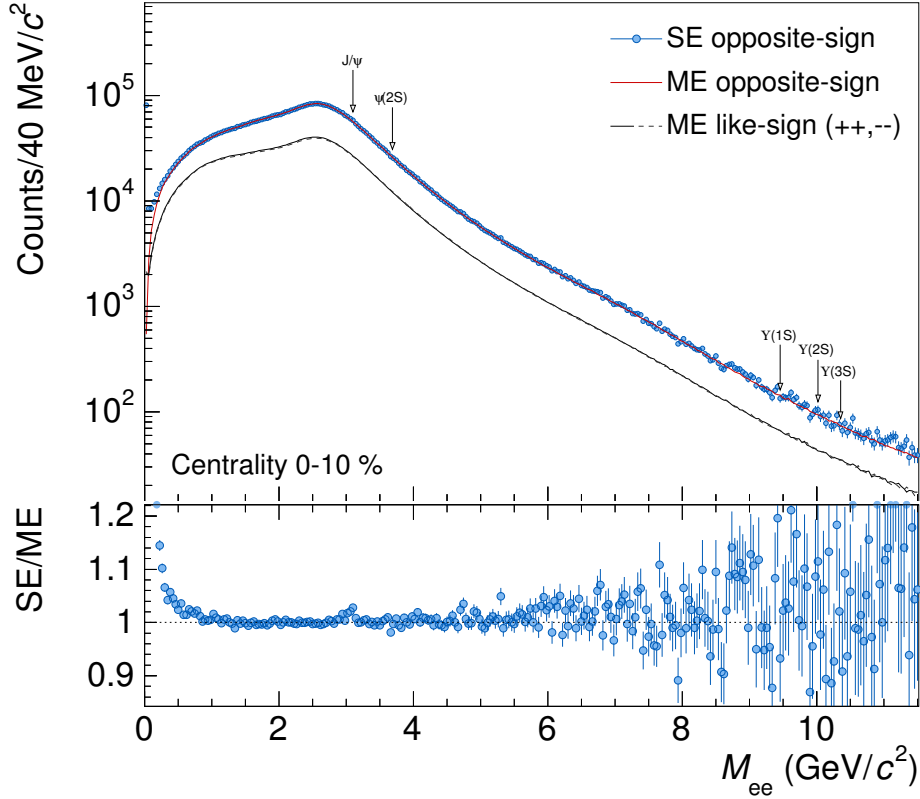
Figure 4.18.: The like- and opposite-sign distribution from event mixing.

interval $2.92 < m_{inv} < 3.16$ GeV/c^2 by bin counting. In Pb-Pb, the optimal integration window with respect to significance and signal-to-background is found to be the same as in the J/ψ analysis of pp collision such as [38], see App. C. The corresponding signal S, signal-to-background ratio S/B and the significance $S/\sqrt{S+B}$ are given in the lower panels of Fig. 4.19. The invariant mass resolution for the 10% most central Pb-Pb events, obtained via a Crystal-Ball [124] fit to the subtracted spectrum, of approximately $\sigma/m_{inv} = 1\%$ is in agreement with [86].

4.4. Corrections

The extracted J/ψ yield depends on the finite acceptance of the Central-Barrel detectors and is further reduced by the kinematical selections done in Sec. 4.3. In addition, the ALICE detector is not fully efficient in particle reconstruction and identification. In order to extract the physical particle yield, these effects need to be quantified and applied to the measured rates. The tool to study these effects are Monte Carlo simulations of
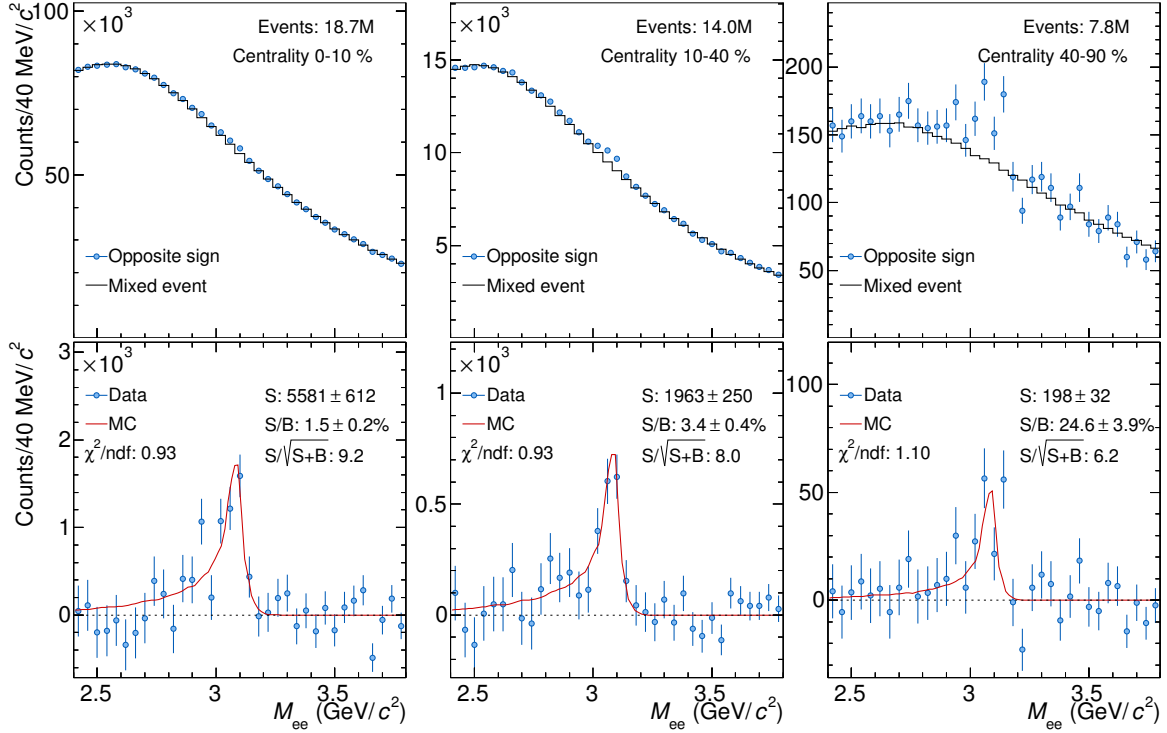
Figure 4.19.: J/ψ signal extraction of the invariant mass distribution with the ME technique for the three centrality intervals $(0 - 10\%)$, $(10 - 40\%)$ and $(40 - 90\%)$.

events which are propagated to a virtual ALICE detector implemented into GEANT. The identical reconstruction algorithm used in collision data are adopted and the detector conditions during the data taking are feed into the MC environment. Hijing is the underlying event generator in the MC production of Pb-Pb collisions at $\sqrt{s_{NN}} = 2.76$ TeV. Additionally, the particle sample is enriched by Pythia events each containing 10 J/ψ that are forced to decay into e$^+$e$^-$(γ). Acceptance and efficiency studies are based on directly simulated J/ψ in the rapidity interval $|y| < 0.8$. In order to quantify the efficiency of several analysis steps, the analysis of correction factors was divided into four groups: geometrical acceptance A, reconstruction efficiency ϵ_{rec}, PID efficiency ϵ_{PID} and signal integration efficiency ϵ_{int}. The product of all steps, the total efficiency $A \times \epsilon$, is shown in Fig. B.2 and applied to the measured yield $N_{\text{J}/\psi}$ for correction:

$$\mathrm{d}N/\mathrm{d}y = \frac{N_{\text{J}/\psi}}{BR(\text{J}/\psi \to \text{e}^+\text{e}^-) \ A \times \epsilon \ N_{\text{evt}} \ \Delta y}, \tag{4.18}$$

where $BR(\text{J}/\psi \to \text{e}^+\text{e}^-)$ is the branching ratio in the dielectron decay channel including the radiative decay, see Chapter 2. The yield is normalized to the rapidity range Δy and

the number of event N_{evt} in the measurement. Step-wise efficiencies integrated over p_{T} and rapidity are summarized in Tab. 4.6. Details of the individual steps are discussed in the following section.

Efficiency (%)	Centrality (%)		
	0-10	10-40	40-90
A	32.6	32.6	34.4
ϵ_{rec}	51.9	53.1	59.9
ϵ_{PID}	44.7	46.7	65.3
ϵ_{int}	68.2	67.5	71.7
FSR correction	-	-	1/1.153
$A \times \epsilon$	5.2	5.5	8.3

Table 4.6.: Partial efficiency obtained for the standard set of selections.

The total efficiency of the radiative and non-radiative decay of J/ψ (introduced in Chapter 2) differ by a factor 2.15 due to the photon emission. The difference can be explained by the acceptance and integration efficiency: (i) for a certain J/ψ p_{T} the geometrical acceptance for radiative decays is smaller due to the minimum p_{T} requirement for the decay daughters. (ii) the invariant mass distribution of dielectron pairs is broader for radiative than non-radiative decays.

Since the MC simulation used for the efficiency calculation for the centrality interval 40-90% was done before the radiative decay of J/ψ was implemented, the ratio of efficiencies ($\epsilon_{\text{non-rad}}/\epsilon_{\text{prompt}}$) is evaluated in the MC analysis with both decay channels. The adjustment for final state radiation (FSR) amounts to 1/1.153 and is used to scale down the integrated efficiency.

4.4.1. Geometrical Acceptance

The geometrical acceptance is defined by the detectors used in the analysis. The TPC has full coverage in the azimuthal angle, the polar acceptance correspond to $|\eta| < 0.9$ and tracks with momentum down to $p = 200$ MeV/c can be reconstructed. For the J/ψ reconstruction, the longitudinal $|\eta| < 0.8$ and transverse $p_{\text{T}} > 0.85$ GeV/c direction of tracks are further restricted. In order to avoid edge effects in the correction also the reconstructed pair rapidity is limited to $|y| < 0.8$. The dependence on the transverse

momentum and rapidity of the J/ψ is shown in Fig. B.2. The acceptance drops towards intermediate $p_\mathrm{T} = 2.5$ GeV/c and then monotonously increases for higher p_T. This behaviour can be understood as follows: (i) electrons produced under large opening angles typically belong to low J/ψ p_T and in case of a decay in the rz-plane do not fall into the acceptance of the TPC, while with increasing J/ψ p_T the opening angle decreases and therefore a detection becomes more likely. (ii) for decays in xy-plane and J/ψ $p_\mathrm{T} = 0$, the daughters electrons are emitted back-to-back, both with $p_\mathrm{T} \approx m_{\mathrm{J}/\psi}/2$, such that they pass the transverse momentum criterion. With increasing J/ψ p_T the p_T of the decay daughter emitted into the flight direction of the mother is boosted, while the p_T of the other daughter is reduced and therefore can suffer from the p_T threshold. For sufficiently high J/ψ transverse momentum both daughters fly into the same direction and both will pass the p_T cut.

4.4.2. Reconstruction Efficiency

The J/ψ decay products matching the geometrical acceptance have to pass the quality cuts described in Sec. 4.3.1. The loss of signal due to inefficiencies in the track reconstruction (detector performance, calibration issues, algorithm, . . .) is called reconstruction efficiency and linearly decreases with increasing J/ψ p_T as shown in Fig. B.2 (left). At low transverse momentum, the track length of the particles is longer due to the shorter bending radius in the magnetic field. Therefore the number of associated clusters and segments in the TPC is larger compared to straight high p_T tracks. Almost no variation versus rapidity is found, since two effects cancel: (i) the ITS efficiency slightly increases towards positive pseudo-rapidity, due to looser SPD hit requirements (a consequence of the larger number of inactive modules), (ii) mainly TPC readout chambers on the Muon-side of ALICE (negative pseudo-rapidity) are effected by the high-voltage issues mentioned in Sec. 4.2 and therefore show a weaker performance for negative J/ψ rapidity. ALICE was build for track reconstruction of charged particles in much larger numbers than finally observed, thus no significant dependence on centrality of the reconstruction efficiency is observed.

Fig. 4.21a shows the J/ψ efficiency for all track selection criteria used in the efficiency calculations. According to this, the J/ψ reconstruction probability is dominated by the transverse momentum cut and the ITS hit selection. They show the largest rejection power, defined as the ratio of cut efficiencies for J/ψ over background $\epsilon_{\mathrm{cut}}(\mathrm{J}/\psi)/\epsilon_{\mathrm{cut}}(\mathrm{B})$, see Fig. 4.21b.
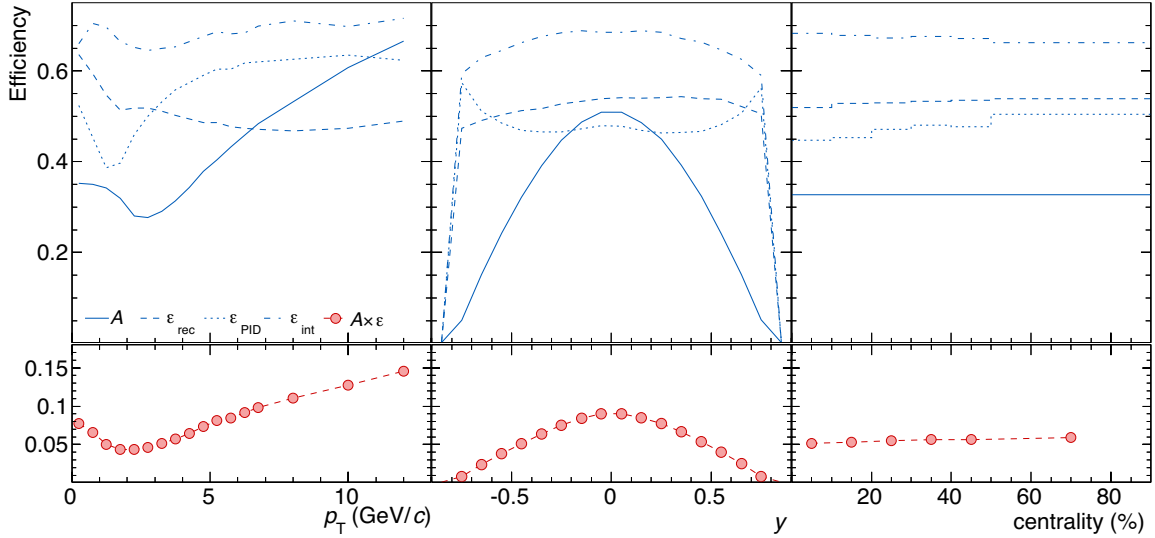
Figure 4.20.: Partial J/ψ efficiencies versus transverse momentum, rapidity and collision centrality. The geometrical acceptance A (solid), reconstruction efficiency ϵ_{rec} (dashed), particle identification efficiency ϵ_{PID} (dotted) and the signal integration efficiency ϵ_{int} (dash dotted) as extracted from MC simulations.

(a) J/ψ efficiency.
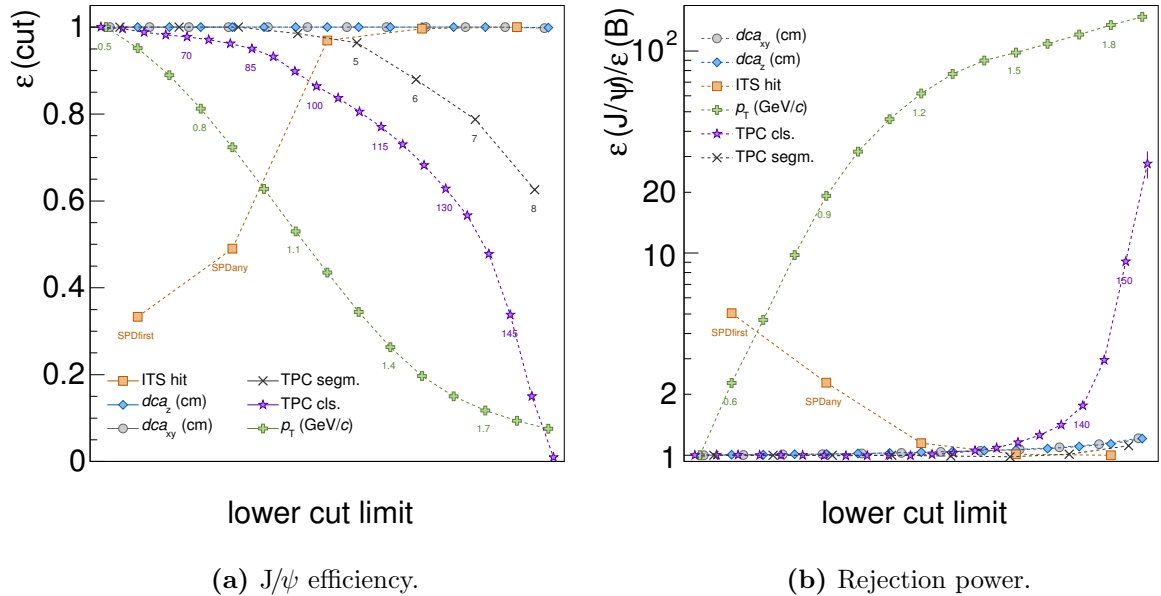
(b) Rejection power.

Figure 4.21.: Left: The J/ψ efficiency dependence on single reconstruction cuts for lower cut limits. Right: The rejection power for the different cuts as obtained from the ratio of efficiencies for direct J/ψ and background particles.

4.4.3. Particle-Identification Efficiency

The proper evaluation for the inefficiencies of the PID procedure is the most crucial part, since it applies the strongest rejection of tracks. The particle identification efficiency ϵ_{PID} is calculated with respect to the previous reconstruction cuts, after applying the PID selection listed in Tab. 4.4. Due to differences in the PID response between data and MC, the following procedure was developed. First the same post-calibration technique, described in Sec. 4.3.2, is applied to MC. The corresponding correction of the electron PID response is less sizable, see App. A. Then, the proton rejection cut of $n\sigma_{\mathrm{p}} > 4.0$ applied to collision data is expressed in terms of σ_{e} for all momenta and in small intervals of centrality and pseudo-rapidity, in order to take into account changes of the TPC PID response function. Projections of the proton rejection translated into electron inclusion cuts are shown in Fig. 4.22. The selection map is then applied to the tracks in MC simulations.

(a) Momentum dependence.

(b) Pseudo-rapidity versus momentum.
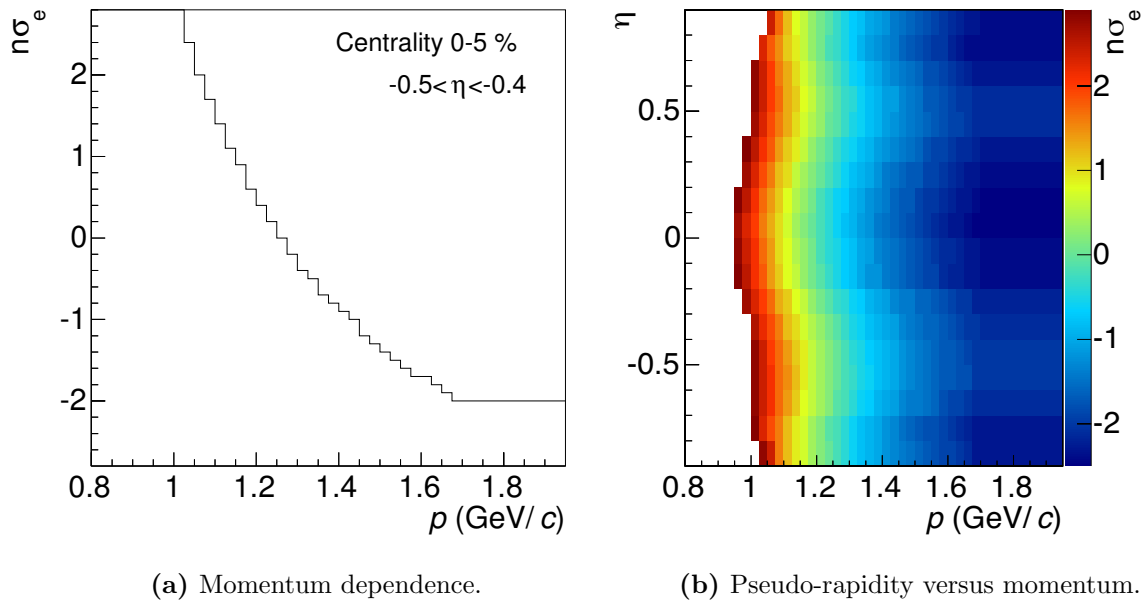
Figure 4.22.: Translation of the proton rejection cut into $n\sigma_{\mathrm{e}}$ for collision data. The projection of the selection map versus track momentum p (left) and η versus p (right) for the centrality interval $0-5\%$.

As a consequence, the PID selection done in data is closely imitated in MC. In addition, the standard electron inclusion $-1 < n\sigma_{\mathrm{e}} < +3$ is applied to the MC tracks. The evaluated PID efficiency for p_{T}, y and centrality are indicated by the dotted lines of Fig. B.2.

4.4.4. Signal Integration Efficiency

As mentioned in the beginning of this section, efficiencies are calculated for direct J/ψ. This includes the radiative $(J/\psi \rightarrow e^+e^-\gamma)$ and non-radiative decays $(J/\psi \rightarrow e^+e^-)$. Their decay products can experience Bremsstrahlung. In the analyses of the MC sample, J/ψ decays into electrons are enriched by Pythia events and their decay (radiative or not) is handled by the EvtGen package [125], where the final state radiation is described by PHOTOS [126]. Both components are shown in the invariant mass distribution, see Fig. 4.23, and used for the evaluation of signal integration efficiency ϵ_{int}. The integration window $2.92 < M_{\text{ee}} < 3.16$ GeV/c^2 for the signal extraction, described in Sec. 4.3.4, corresponds to 67.8% of all J/ψ surviving the track and pair selections. For this correction a proper simulation of the interaction of electrons with material and a good description of the detector material in GEANT is essential. In collision data, the background-subtracted invariant-mass distributions are compared to the J/ψ MC shape, see Fig. 4.19. Within the statistical uncertainty, a good matching and for this reason a proper description of the material budget and reliable performance in MC simulations is ensured.
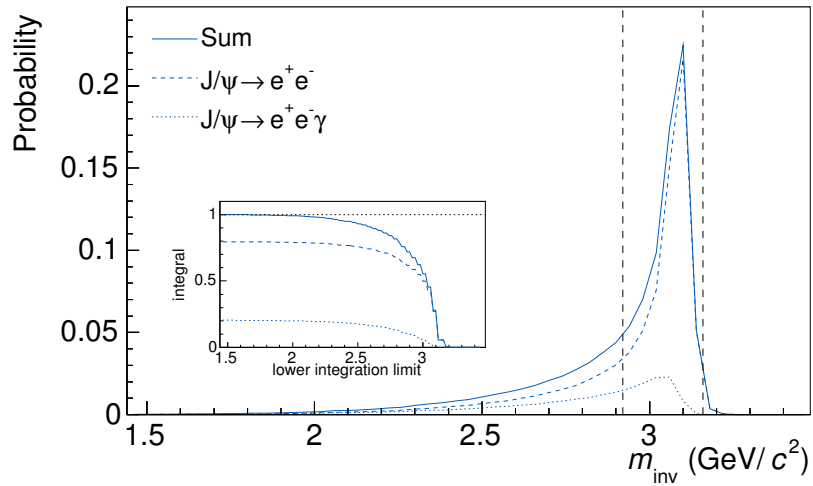
Figure 4.23.: The invariant mass distributions for the radiative and non-radiative J/ψ decay in MC simulations. The integration window used for bin counting is indicated by the vertical lines.

The p_{T}- and y-dependence of the signal integration efficiency, shown in Fig. B.2, can be explained with a similar argument given in Sec. 4.4.2: the drop of ϵ_{int} towards larger p_{T} and $|y|$ is based on the (in average) larger track length of the J/ψ daughters, therefore the probability for Bremsstrahlung is increased and the invariant-mass distribution gets

broader. The decreasing p_{T} resolution of the daughter tracks might result in the slight increase of the integration efficiency for $p_{\mathrm{T}} > 5$ GeV/c.

4.5. Centrality Dependence of the Nuclear Modification Factor

In this section, first the nuclear modification factor, R_{AA}, is introduced, then the systematic uncertainties are discussed and finally results of the centrality dependence of R_{AA} for J/ψ in $\sqrt{s_{\mathrm{NN}}} = 2.76$ TeV in Pb-Pb collisions are presented. The results are compared to published data by ALICE and other experiments, and discussed in the context of different theory calculations.

The Nuclear Modification Factor R_{AA}

The QCD matter produced in heavy-ion collisions is dominated by soft particles, while hard scatterings in the initial state of the collisions can result in "quasi-free" partons (di-jets or high-p_{T} particles) that probe the formed medium through energy loss. Since hard processes scale with the number of binary collisions, as defined in Sec. 4.2.1, an interesting observable introduced in [127] is the nuclear modification factor, see Eq. (4.19a). The measured yield of particles $\mathrm{d}N/\mathrm{d}y$ in nucleus-nucleus collisions (A-A) is compared to a simple superposition (scaling by N_{coll}) of the corresponding yield in nucleon-nucleon collisions (pp), where no formation of a Quark-Gluon Plasma is expected. Often R_{AA} is quantified w.r.t. the pp reference measured in terms of the cross-section σ_{pp} scaled by the geometrical nuclear overlap T_{AA} as explained in Sec. 4.2.1.

$$R_{\mathrm{AA}} = \frac{\mathrm{d}N/\mathrm{d}y_{\mathrm{A\text{-}A}}}{N_{\mathrm{coll}} \times \mathrm{d}N/\mathrm{d}y_{\mathrm{pp}}} \tag{4.19a}$$

$$= \frac{\mathrm{d}N/\mathrm{d}y_{\mathrm{A\text{-}A}}}{T_{\mathrm{AA}} \times \sigma_{\mathrm{pp}}}, \tag{4.19b}$$

In pp collisions at $\sqrt{s} = 2.76$ TeV, the inclusive J/ψ cross sections at mid-rapidity measured by ALICE [128] is:

$$\mathrm{d}\sigma/\mathrm{d}y_{\mathrm{J}/\psi} = 4.31 \pm 0.99(\text{stat.}) \pm 0.77(\text{syst.}) \text{ µb} \qquad (4.20)$$

The cross-section measurement is based on 59 ± 14 J/ψ counts and the combined statistical and systematic uncertainty corresponds to 29% of the cross-section. As a consequence, an interpolation based on mid-rapidity measurements by PHENIX [129], CDF [130], and ALICE [128, 131], done in [132], was used for the calculation of the R_{AA} versus centrality. The uncertainty on the pp reference is reduced by a factor two compared to the measurement:

$$\mathrm{d}\sigma/\mathrm{d}y_{\mathrm{J}/\psi}^{\text{intp.}} = 4.25 \pm 0.28(\text{stat.}) \pm 0.43(\text{syst.}) \text{ µb} \qquad (4.21)$$

4.6. Systematic Uncertainties

Systematic uncertainties in the analysis of J/ψ production in Pb-Pb collisions have been estimated. Tab. 4.7 summarizes the different contributions to the total systematic uncertainty, that are added in quadrature. They can be categorized into point-by-point correlated (type I) or uncorrelated (type II) uncertainties. The different contributions are discussed in the following. Due to the spare statistics for peripheral collisions, only a reduced number of systematic checks with an adequate signal extraction are possible.

Uncertainty (%)	Centrality (%)			Type
	0-10	10-40	40-90	
Signal extraction	± 12.4	± 12.1	± 7.9	II
MC input kinematics	± 5.3	± 5.3	± 5.3	I
Nuclear overlap	± 3.2	± 3.2	± 5.2	II
pp reference	± 12.1	± 12.1	± 12.1	I
Total	± 13.2	± 13.2	± 13.2	I
	± 12.8	± 12.5	± 9.4	II

Table 4.7.: Systematic uncertainties on the R_{AA}. The type specifies whether the uncertainty is correlated (type I) or uncorrelated (type II) between the centrality intervals.

4.6.1. J/ψ Reconstruction and Signal Extraction

The largest contribution to the total systematic uncertainties arises from the variation of the track selection and the corresponding signal extraction. Variations for all parts of the analysis are applied and corrected yields $\mathrm{d}N/\mathrm{d}y$ are calculated according to Sec. 4.4. The systematic uncertainties for all variations are obtained via the Barlow criterion [133]. In order to understand whether a systematic effect is present for a certain variation i, the systematic deviation is calculated relative to the standard track selections std in terms of a statistically independent quantity $(\mathrm{d}N/\mathrm{d}y)$:

$$\Delta(\mathrm{d}N/\mathrm{d}y)_i = \mathrm{d}N/\mathrm{d}y_i - \mathrm{d}N/\mathrm{d}y_{std} \qquad (4.22)$$

By varying the track selection, we obtain either a statistical sub- or superset. The statistical uncertainty $\delta(\Delta(\mathrm{d}N/\mathrm{d}y)_i)$ of a variation on the systematic deviation $\Delta(\mathrm{d}N/\mathrm{d}y)_i$ is (almost) independent on the standard selection:

$$\delta(\Delta(\mathrm{d}N/\mathrm{d}y)_i) = \sqrt{|\delta^2(\mathrm{d}N/\mathrm{d}y_i) - \delta^2(\mathrm{d}N/\mathrm{d}y_{std})|} \qquad (4.23)$$

Where, $\delta(\mathrm{d}N/\mathrm{d}y_i)$ and $\delta(\mathrm{d}N/\mathrm{d}y_{std})$ correspond to the statistical uncertainty of $\mathrm{d}N/\mathrm{d}y$ for a certain variation i and the standard selections std.

Fig. 4.24 shows the $\mathrm{d}N/\mathrm{d}y$ of the cut variation with their independent (uncorrelated) uncertainty w.r.t. the standard cut choice. Deviations by less than one sigma are candidates for pure statistical fluctuations, while all others are taking as systematic variation. The mean of these distributions in the vertical is taken as the final $\mathrm{d}N/\mathrm{d}y$ value (solid line) with an systematic uncertainties covering all significant deviations (dashed lines). Depending on the centrality the systematic uncertainties from this contribution vary between 7.9% (peripheral) and 12.4% (central).

4.6.2. MC Input kinematics

The integrated efficiency applied in this analysis is calculated for $p_\mathrm{T} < 10$ GeV/c and $|y| < 0.8$. As described in Sec. 4.4, there are strong variations with transverse momentum and rapidity. Fig. 4.25 shows the p_T spectrum (red) used as input for MC simulations[6]. The shape can be considerably well described by a double m_T exponential ($\propto \exp(-m_\mathrm{T}/T_1) +$

---

[6]J/ψ p_T parametrization include the EKS98 [134] shadowing model with a minimum bias shadowing factor of 0.66 in 4π.
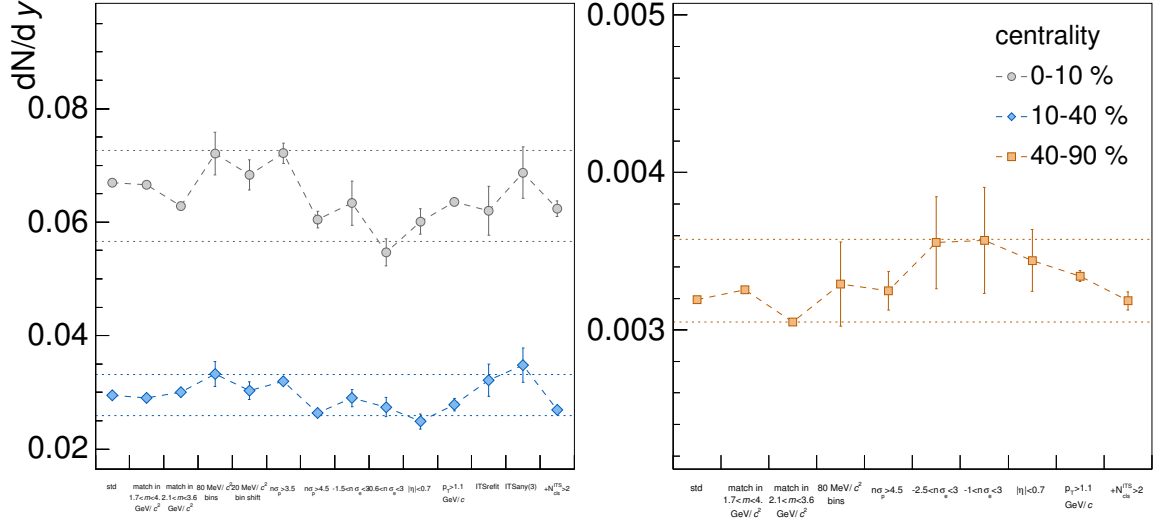
Figure 4.24.:   The efficiency corrected $\mathrm{d}N/\mathrm{d}y$ with its systematic variations in the three centrality intervals. The statistical uncertainties of the points are the uncorrelated contributions with respect to the standard selection and signal extraction. The dashed lines correspond systematic uncertainties assigned to the measurement.

$\exp(-m_\mathrm{T}/T_2)$) (dotted line). In order to study the effect of this input spectrum on the average efficiency, the two inverse slope parameters are independently and randomly varied within $T_{1,2} \pm 50\%$. The RMS of the resulting p_T-distributions is shown in Fig. 4.25 as the blue band. The corresponding deviation from the standard average efficiency is shown in the subpanel and accounts to 5.3%. The rapidity distribution of the MC input spectrum is almost flat within $|y| < 0.8$, therefore the effects can be neglected safely.

4.6.3. Normalization

The systematic uncertainty of the normalization is given by the pp reference (correlated; see above) and the nuclear overlap (uncorrelated) as calculated in the centrality determination (see Sec. 4.2.1). Their uncertainties are given in Tab. 4.7.

4.6.4. Results

The p_T-integrated R_AA of inclusive J/ψ in Pb-Pb collisions at $\sqrt{s_\mathrm{NN}} = 2.76$ TeV is compared to the published result by ALICE [132] in Fig. 4.26. The systematic and statistical uncertainties are partially uncorrelated, since there are significant differences in
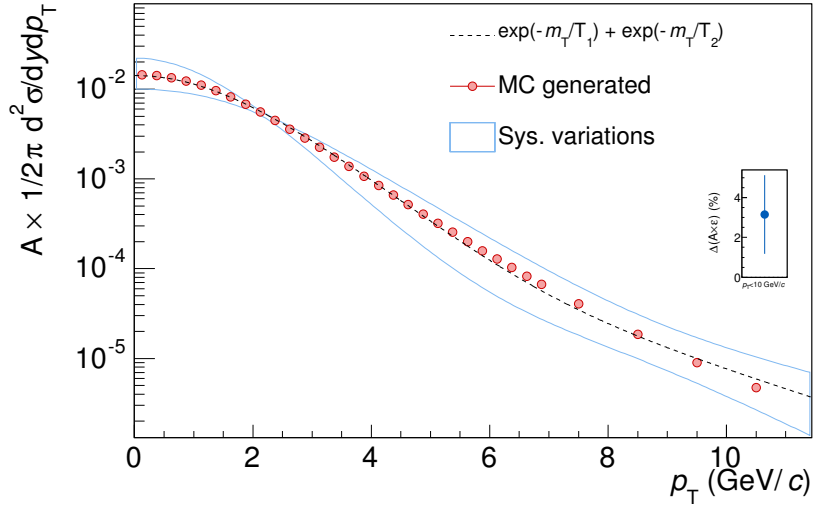
Figure 4.25.: Systematic variations of the MC input p_T spectrum and the effect on the integrated efficiency (sub panel).

the setup of the two mid-rapidity analyses. For the publication the data of two running periods (LHC10h, LHC11h) are combined for the centrality interval $0-10\%$ and $10-40\%$. Good consistency is found between the two measurements. In comparison to the ALICE measurement in the dimuon decay channel at forward rapidity, slightly less suppression is observed, possibly related to a higher charm quark density at mid-rapidity which make recombination more important. In both rapidity intervals no strong centrality dependence has been found for $N_{part} > 70$.

Comparison to Other Measurements

As illustrated in Fig. 4.27, a significant difference of the inclusive J/ψ R_{AA} to the results reported by the PHENIX and STAR collaborations [129, 135] for lower centre-of-mass energy is observed, with a factor 2-3 less suppression for the 10% most central events. A prompt J/ψ measurement at the same energy as studied in this work was performed by the CMS collaboration [136]. Clearly stronger suppression of the R_{AA} is found compared to the results of this thesis. The fraction from non-prompt J/ψ in $|y| < 2.4$ for CMS acceptance is $f_B \approx 23.5\%$ and therefore has no large impact. In CMS J/ψ is measured for $6.5 < p_T < 30$ GeV/c and the R_{AA} drops with increasing centrality, which points to an important contributions of low-p_T J/ψ particles that seems to vary with centrality. The transverse momentum behaviour of J/ψ production is studied in Sections 5.1 and 5.2 of this work.
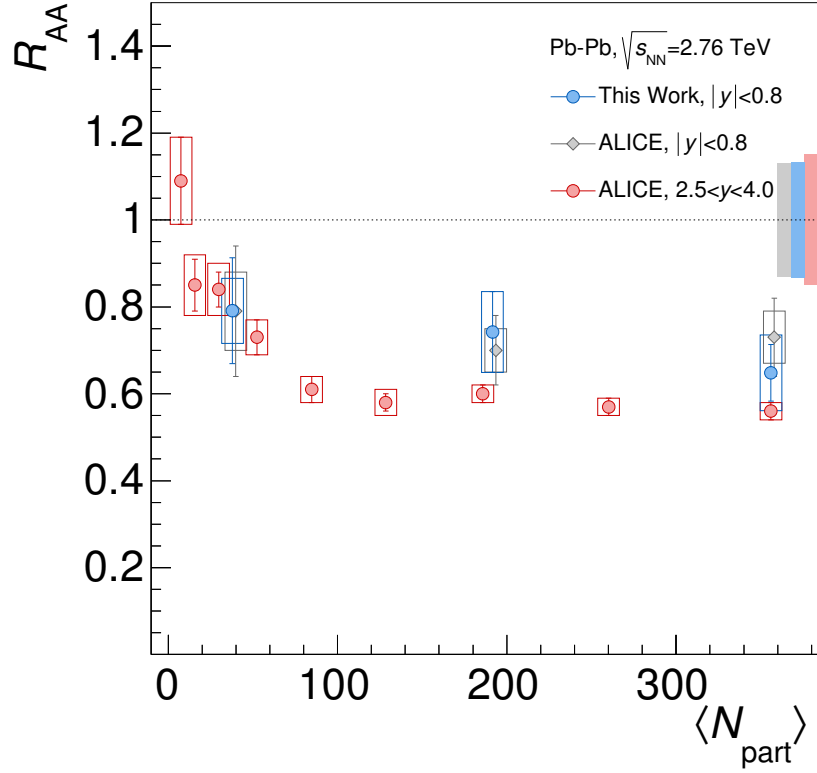
Figure 4.26.: The inclusive J/ψ R_{AA} as a function centrality compared to the ALICE measurements published in [132]. Open boxes correspond to the uncorrelated uncertainties between the points, while the global, correlated uncertainties are indicated by the coloured box at $R_{AA} = 1$.

Comparison to Theory Calculations

As introduced in Chapter 2, different concepts are used to describe J/ψ production in heavy-ion collisions. In Fig. 4.28 a compilation of the theory calculations available for J/ψ production in the same kinematic range as the measurement is given. In the concept of statistical hadronization [137] it is assumed that charm quarks are produced via hard collisions and recombination happens only at the phase boundary of the QGP. For the transport models [138–140], both dissociation and recombination processes are present throughout the whole hydro-dynamical evolution of the system. For [140], the effect of dissociation is described within the comover interaction model. All model calculation can describe the trend seen in data within their uncertainty. The main uncertainty of all models comes from the ambiguity of the c$\bar{c}$ cross section for LHC energy, which has not yet been determined by ALICE for Pb-Pb collisions.
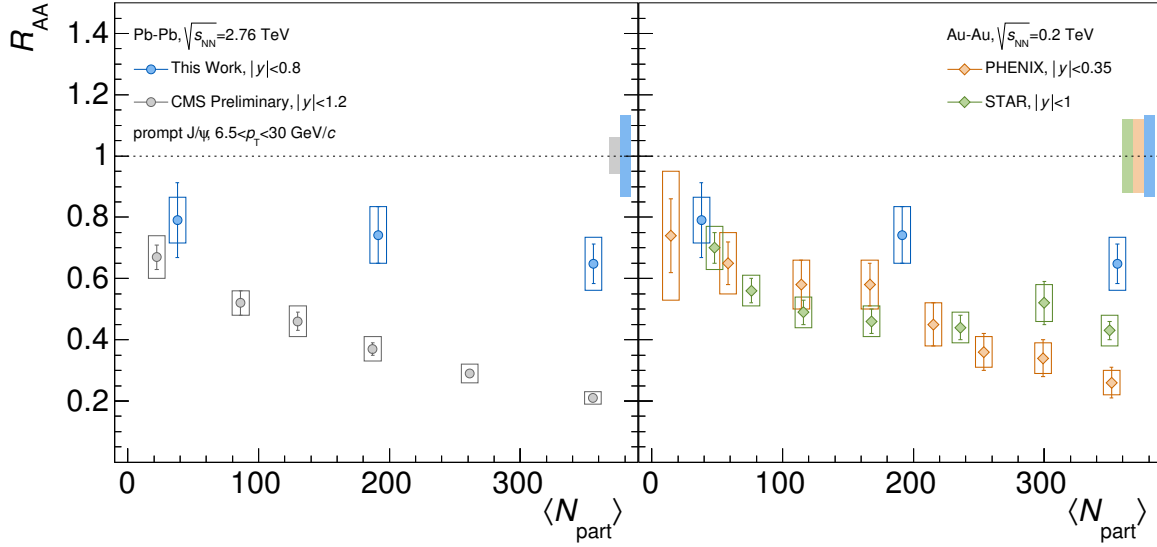
Figure 4.27.: The inclusive J/ψ R_{AA} at mid-rapidity $|y| < 0.8$ compared to the PHENIX $|y| < 0.35$ and prompt J/ψ measurement by CMS $|y| < 1.2$ as a function of the number of participant nucleons N_{part}.

Charged Particle Density Dependence of J/ψ Production

In Tab. 4.8 the average dN/dy with statistical and systematic uncertainties are given for the three centrality intervals. An extrapolation of J/ψ production versus the underlying event multiplicity $dN_{ch}/d\eta$ in pp collisions [37] towards Pb-Pb collisions is shown in Fig. 4.29. At LHC energies, the event multiplicity changes from pp to Pb-Pb systems by up to two orders of magnitude. To first order, J/ψ production seem to scale with the charged particle multiplicity, when the absolute dN/dy values for pp collisions at $\sqrt{s} = 7$ TeV are scaled to $\sqrt{s} = 2.76$ TeV using the ratio of inclusive J/ψ cross-sections given in [131] and Eq. (4.21) as scaling factor. The $dN_{ch}/d\eta$ values are listed in Tab. 4.2 and are obtained from [113]. They are connected to the initial energy density of the system according to [28]. A 1st order polynomial (red) is fitted to the pp results. In the lower panel of Fig. 4.29, the ratio "data/fit" shows a factor 3 more J/ψ production in Pb-Pb collisions then expected from the pp extrapolation indicating that no simple scaling for the J/ψ production related to the underlying event multiplicity from pp to Pb-Pb collisions is present. This can be further confirmed by the linear fit to pp and Pb-Pb data (black) with a χ^2/ndf of 4.25.

In [141] the relative production of $\Upsilon(nS)/\Upsilon(1S)$ versus multiplicity is discussed. A decrease of relative Υ production is found and hints to a smooth suppression pattern
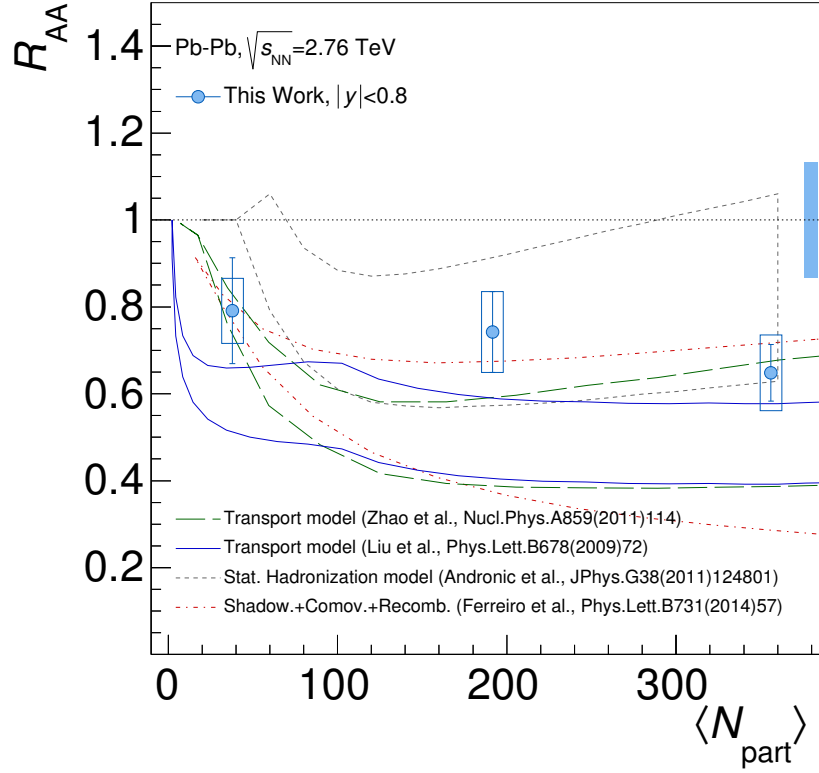
Figure 4.28.: The centrality dependence of inclusive J/ψ R_{AA} at mid-rapidity $|y| < 0.8$ compared to several transport model calculations and the statistical hadronization model.

Centrality (%)	dN/dy ($\times 10^{-2}$)
$0 - 10$	$6.46 \pm 0.65 \pm 0.80$
$10 - 40$	$2.95 \pm 0.37 \pm 0.36$
$40 - 90$	$0.33 \pm 0.05 \pm 0.03$

Table 4.8.: dN/dy values for the three centrality intervals. Statistical and uncorrelated systematic uncertainties (type II) are quoted. The global uncertainty on the result is 5.4% and originates from the unknown J/ψ transverse momentum distribution in the efficiency calculation.

from pp to p-Pb to Pb-Pb collisions. This might be an indication for either systematically more particle production when the ground state (1S) is formed compared to the exited states and would affect the underlying multiplicity distribution, or a stronger interaction of the excited states (2S,3S) with the surrounding environment, than for the smallest, most tightly bound state Υ(1S). A normalization of the J/ψ production to open charm will help to understand the underlying physics.

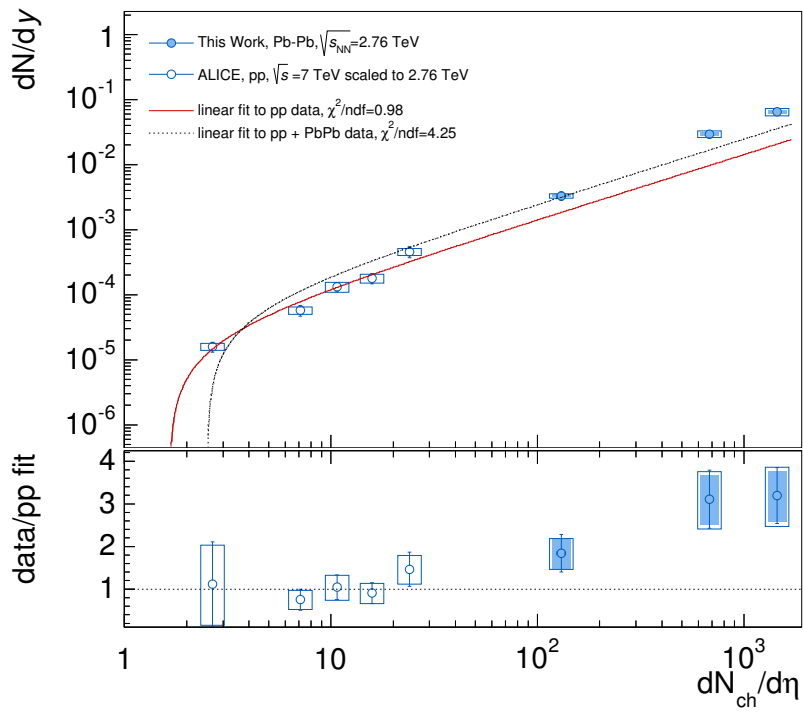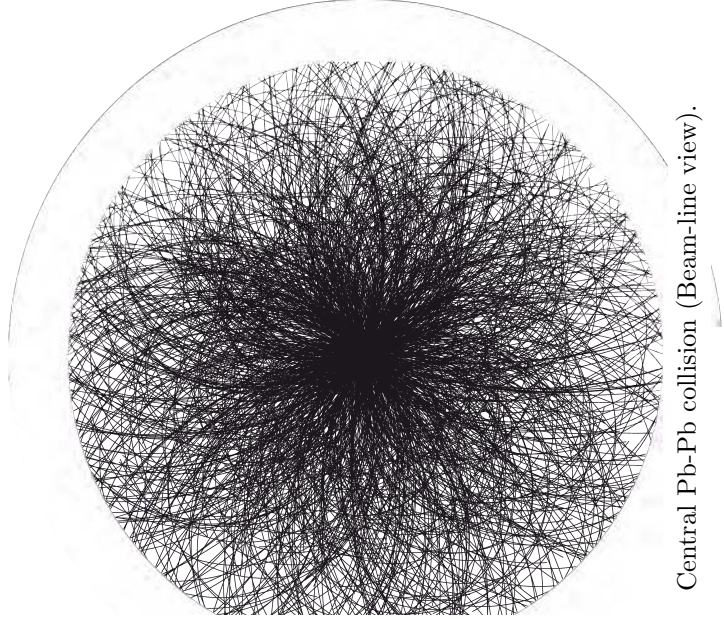**Figure 4.29.:** dN/dy versus the underlying charged particle multiplicity for pp and Pb-Pb collisions. Bottom: The fit uncertainty is propagated into the ratio.

Chapter 5.

Transverse Momentum Dependence of J/ψ Production

5.1. p_{T}-Dependence of the R_{AA}

ALICE is the only experiment at the LHC, that can measure J/ψ production at mid-rapidity down to $p_{\mathrm{T}} = 0$. In this section, the nuclear modification factor in transverse momentum intervals is studied.

5.1.1. Signal Extraction in Transverse Momentum Intervals

In order to obtain a good statistical significance, events in the large centrality interval from 0 to 40% are selected. Since this interval contains two different multiplicity trigger (see Sec. 4.2.1), the invariant mass spectra in the same-event (SE) and mixed-event (ME) need to be normalized accordingly:

$$\frac{(S+B)_{SE}^{0-40\%}}{N_{evt}} = \frac{1}{4} \times \frac{(S+B)_{SE}^{0-10\%}}{N_{evt}^{0-10\%}} + \frac{3}{4} \times \frac{(S+B)_{SE}^{10-40\%}}{N_{evt}^{10-40\%}} \tag{5.1a}$$

$$\frac{B_{ME}^{0-40\%}}{N_{evt}} = \frac{1}{4} \times \frac{B_{ME}^{0-10\%}}{N_{evt}^{0-10\%}} + \frac{3}{4} \times \frac{B_{ME}^{10-40\%}}{N_{evt}^{10-40\%}} \tag{5.1b}$$

Without the applied weighting, the signals are biased towards more central events. Fig. 5.1 shows the signal extraction in the p_{T} intervals $0-2.5$ and $2.5-6$ GeV/c. The quoted significance, statistical uncertainty of the signal and signal-to-background ratio (S/B) correspond to the unweighted spectra. The average corrections in $0-40\%$ most central

events, described in Sec. 4.4, are calculated for the quoted p_T intervals. The corrections are applied to the normalized signal yield and further corrected for the rapidity interval and branching ratio to obtain the $\mathrm{d}N/\mathrm{d}y$.
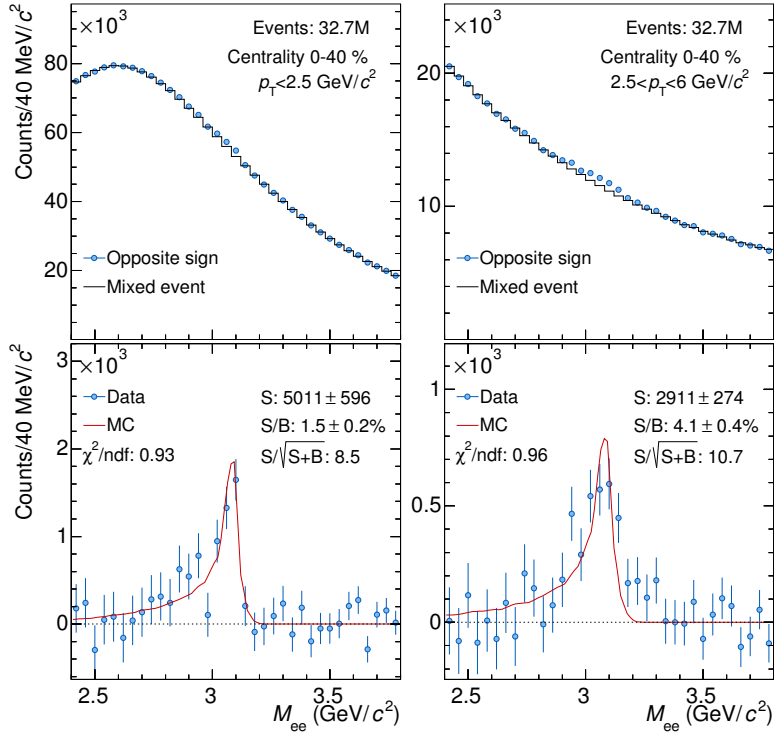

Figure 5.1.: The invariant mass distribution for the two p_T intervals and for the 40% most central events.

5.1.2. pp Reference

For the calculation of the R_{AA} versus p_T, a pp reference in the same p_T-intervals is essential. ALICE has measured the cross-section for inclusive J/ψ production at the required energy of $\sqrt{s} = 2.76$ TeV in pp collisions at forward and mid-rapidity [128] as mentioned in Sec. 4.5. However, for the p_T-dependence of the R_{AA}, the corresponding differential cross-sections in p_T at mid-rapidity were not obtained due to a limit in statistic.

In the following a similar procedure to [142] was developed to evaluate the transverse momentum distribution at $\sqrt{s} = 2.76$ TeV and 5.02 TeV for pp collisions[1]. Their precision is crucial for the interpretation of the measured rates in p-Pb and Pb-Pb collisions. In

---

[1] The interpolation for $\sqrt{s} = 5.02$ TeV is used for the publication of the R_{pA} of J/ψ production at mid-rapidity (*publication in preparation*).

this approach all the available experimental data for inclusive J/ψ production in pp collisions with a p_T-reach down to zero are collected and summarized in Tab. 5.1. The p_T-spectra of the double differential cross section $(\mathrm{d}^2\sigma/\mathrm{d}y\mathrm{d}p_T)$ and its $\langle p_T \rangle$, as well as the rapidity differential cross section $(\mathrm{d}\sigma/\mathrm{d}y)$ are calculated numerically. With these numbers an universal scaling for inclusive J/ψ production can be found. In the first step $\mathrm{d}^2\sigma/\mathrm{d}y\mathrm{d}p_T$ is normalized by the p_T-integrated cross section to unity. Then the transformation of $p_T \rightarrow p_T/\langle p_T \rangle$ is done to approach the universal behaviour.

Experiment	$\sqrt{s}$ (TeV)	y	p_T-range (GeV/c)	$\mathrm{d}\sigma/\mathrm{d}y$ (μb)	$\langle p_T \rangle$ (GeV/c)	Ref.
PHENIX	0.2	$|y| < 0.35$	$p_T < 9$	0.79 ± 0.05	1.78 ± 0.07	[143]
	0.2	$1.2 < |y| < 2.2$	$p_T < 8$	0.49 ± 0.02	1.63 ± 0.03	
CDF	1.96	$y < 0.6$	$p_T < 20$	3.40 ± 0.30	2.47 ± 0.03	[130]
ALICE	2.76	$2.5 < y < 4$	$p_T < 8$	2.23 ± 0.20	2.28 ± 0.08	[128, 144] [26, 88, 131]
	7	$2.5 < y < 4$	$p_T < 20$	4.51 ± 0.43	2.47 ± 0.07	
	7	$|y| < 0.9$	$p_T < 10$	6.90 ± 1.18	2.91 ± 0.31	
CMS	7	$1.6 < |y| < 2.4$	$p_T < 30$	7.15 ± 1.03	2.55 ± 0.09	[145]
LHCb	2.76	$2 < y < 4.5$	$p_T < 12$	2.24 ± 0.16	2.17 ± 0.09	[146]
	7	$2 < y < 4.5$	$p_T < 14$	4.24 ± 0.22	2.40 ± 0.05	[147, 148]
	8	$2 < y < 4$	$p_T < 14$	6.11 ± 0.40	2.60 ± 0.03	[149]

Table 5.1.: Compilation of the inclusive J/ψ cross-section $\mathrm{d}\sigma/\mathrm{d}y$ and the average transverse momentum $\langle p_T \rangle$ used for the interpolation analysis.

In this study the statistical and systematic uncertainties for all observables are summed in quadrature and it is supposed that J/ψ mesons are not polarized[2]:

$$\Delta(\mathrm{d}^2\sigma/\mathrm{d}y\mathrm{d}p_T) = \sqrt{stat^2 + syst_A^2 + syst_B^2} \qquad (5.2)$$

The collected p_T spectra are shown in Fig. 5.2 for the different energies, kinematic regions and experiments[3].

---

[2]The existing polarization measurements by ALICE [150], LHCb [148] and CMS [151] show no or only small longitudinal polarization.

[3]For LHCb the differential cross sections are obtained from the prompt and non-prompt spectra for four different rapidity ranges, quoted in [147, 149].
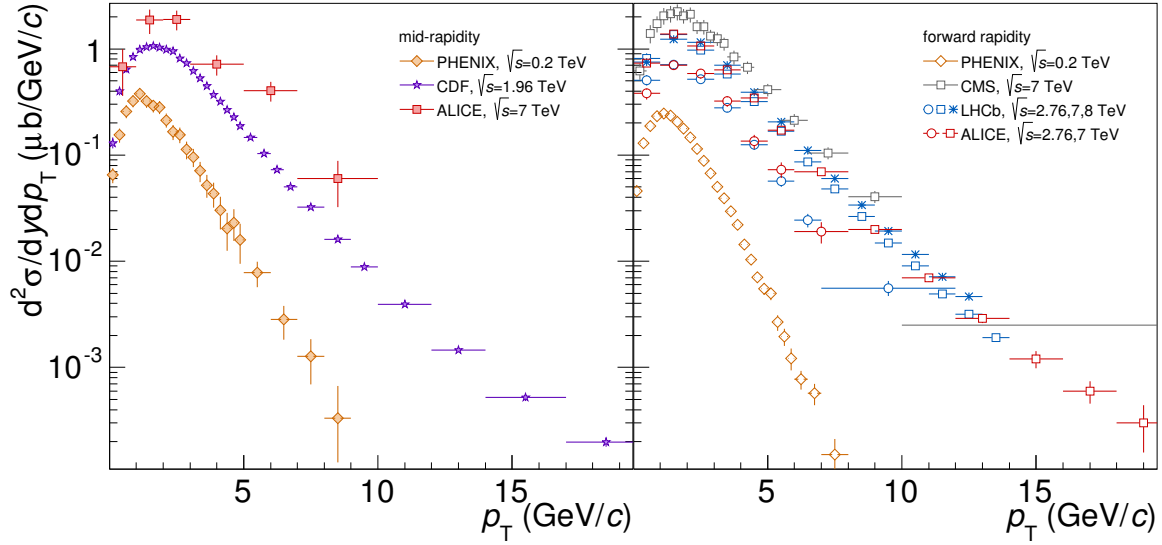
Figure 5.2.: Compilation of inclusive J/ψ cross sections $\mathrm{d}^2\sigma/\mathrm{d}y\mathrm{d}p_\mathrm{T}$ in pp collisions.

Inclusive J/ψ cross sections $\mathrm{d}\sigma/\mathrm{d}y$ are obtained from the data for the PHENIX [143] and the CMS [145] measurement, while for the LHCb results of the prompt and non-prompt contributions are combined at $\sqrt{s} = 7$ and 8 TeV [147–149]. The experimental result by the CDF collaboration was corrected for an old branching ratio $(BR(\mathrm{J}/\psi \to \mu^+\mu^-) = 5.88 \pm 0.10\%)$ used at this time. Fig. 5.3a shows the energy dependence of the inclusive J/ψ production cross section.

The mean transverse momentum for all measurements have been calculated by integrating over the measured $\mathrm{d}^2\sigma/\mathrm{d}y\mathrm{d}p_\mathrm{T}$ spectra in the range $p_\mathrm{T} < 10$ GeV/c, according to:

$$\langle p_\mathrm{T} \rangle = \frac{\sum (\mathrm{d}^2\sigma/\mathrm{d}y\mathrm{d}p_\mathrm{T}) \cdot p_\mathrm{T} \cdot \Delta(p_\mathrm{T})}{\sum (\mathrm{d}^2\sigma/\mathrm{d}y\mathrm{d}p_\mathrm{T}) \cdot \Delta(p_\mathrm{T})} \tag{5.3}$$

For both rapidity intervals of the PHENIX measurement it is confirmed that the integrated value and the one obtained by a modified Kaplan function [152] (see Eq. (5.4)) agree.

$$\frac{\mathrm{d}^2\sigma}{\mathrm{d}y\mathrm{d}p_\mathrm{T}} = A \cdot (1 + (p_\mathrm{T}/B)^2)^{-6} \cdot \frac{2\pi \cdot p_\mathrm{T}}{BR(\mathrm{J}/\psi \to \ell^+\ell^-)} \tag{5.4}$$

The resulting $\langle p_\mathrm{T} \rangle$-dependence is shown as function of the collision energy in Fig. 5.3b, values are listed in Tab. 5.1. At mid- and forward rapidity the average of the functions
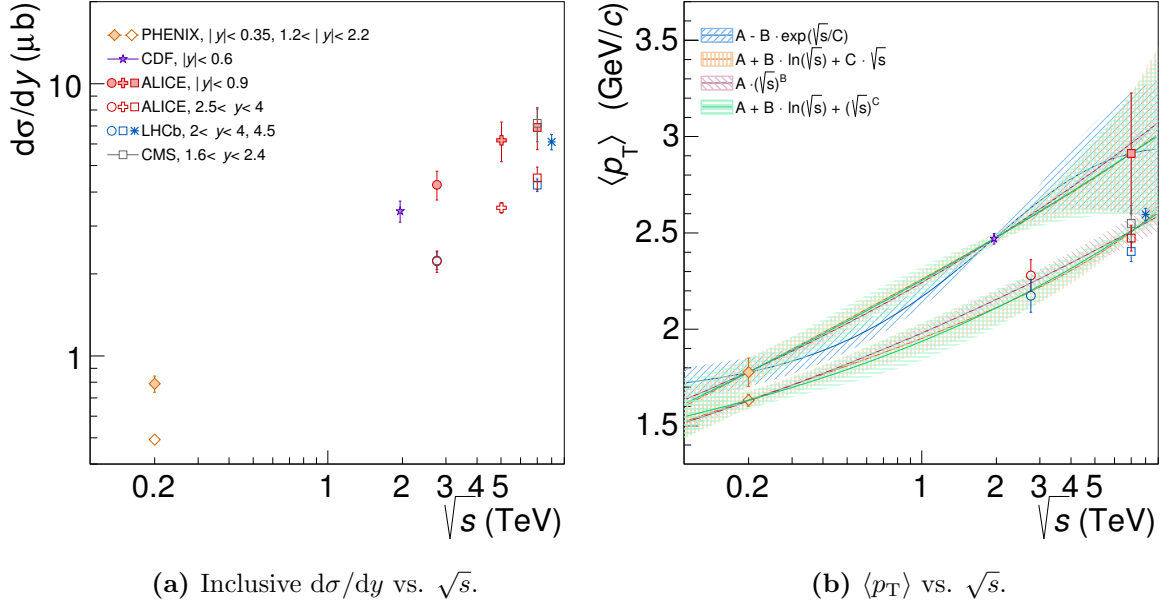
(a) Inclusive dσ/dy vs. $\sqrt{s}$.

(b) $\langle p_{\mathrm{T}} \rangle$ vs. $\sqrt{s}$.

Figure 5.3.: Energy dependence of the cross-sections dσ/dy and the $\langle p_{\mathrm{T}} \rangle$ interpolation done for inclusive J/ψ production in pp collisions.

Eq. (5.5) is used to interpolate the $\langle p_{\mathrm{T}} \rangle$ to $\sqrt{s} = 2.76$ and 5.02 TeV:

$$\langle p_{\mathrm{T}} \rangle = A - B \cdot \exp(\sqrt{s}/C) \tag{5.5a}$$

$$= A + B \cdot \ln(\sqrt{s}) + C \cdot \sqrt{s} \tag{5.5b}$$

$$= A + B \cdot \ln(\sqrt{s}) + (\sqrt{s})^{C} \tag{5.5c}$$

$$= A \cdot (\sqrt{s})^{B} \tag{5.5d}$$

The interpolated $\langle p_{\mathrm{T}} \rangle$ values are listed in Tab. 5.2 together with the results of the cross section interpolations done in [132].

$\sqrt{s}$ (TeV)	y	dσ/dy (μb)	$\langle p_{\mathrm{T}} \rangle$ (GeV/c)
2.76	$|y| < 0.9$	4.25 ± 0.52	2.60 ± 0.04
5.02	$|y| < 0.9$	6.20 ± 1.03	2.81 ± 0.10
5.02	$2.5 < |y| < 4$	5.50 ± 0.38	2.39 ± 0.04

Table 5.2.: The pp interpolation results for dσ/dy and $\langle p_{\mathrm{T}} \rangle$ for the different centre-of-mass energies in ALICE. Quoted uncertainties are the sum of statistical and systematic uncertainties in quadrature.

According to the transformation and scaling noted above, the resulting distributions (see Fig. 5.4) show a common behaviour which can be fitted by the following function:

$$\frac{\langle p_\mathrm{T}\rangle}{\mathrm{d}\sigma/\mathrm{d}y}\cdot\frac{\mathrm{d}^2\sigma}{\mathrm{d}y\mathrm{d}p_\mathrm{T}} = \frac{2(n-1)\cdot B^2\cdot p_\mathrm{T}/\langle p_\mathrm{T}\rangle}{(1+B^2\cdot(p_\mathrm{T}/\langle p_\mathrm{T}\rangle)^2)^n} \tag{5.6}$$

In $B = \Gamma(3/2)\Gamma(n-3/2)/\Gamma(n-1)$ the gamma-function Γ is used and the fit function has only one free parameter n. The fit to all the data with a $\chi^2/\mathrm{ndf} = 0.68$ gives $n = 3.73\pm0.07(\mathrm{stat.})^{+0.16}_{-0.10}(\mathrm{syst.})$.
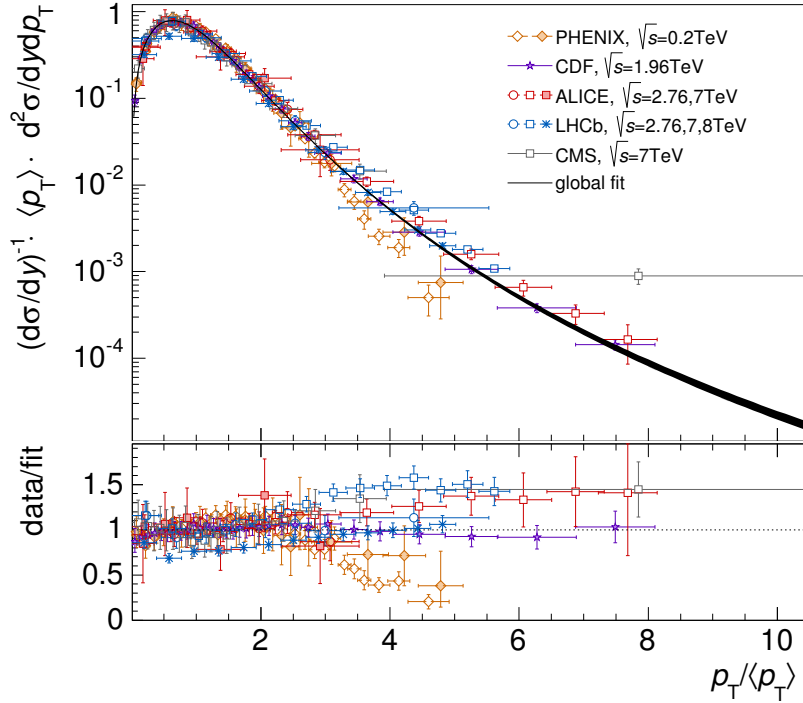

Figure 5.4.: The simultaneous fit to the scaled data (upper panel) and the ratio of the data to the fit result (lower panel).

The systematic uncertainty is determined in Fig. 5.5 (lower panel) for two intervals ($p_\mathrm{T} < 5$ and $5 < p_\mathrm{T} < 10$ GeV/c) by fitting the ratio $|(data-fit)|/(data+fit)$ of all experimental spectra $\mathrm{d}^2\sigma/\mathrm{d}y\mathrm{d}p_\mathrm{T}$ and the corresponding interpolation functions translated into $\mathrm{d}^2\sigma/\mathrm{d}y\mathrm{d}p_\mathrm{T}$ using $\langle p_\mathrm{T}\rangle$ and $\mathrm{d}\sigma/\mathrm{d}y$ (upper panel). This uncorrelated systematic shape uncertainty varies between 4.3% and 9.1% (for $p_\mathrm{T} > 5$ GeV/c).

Finally, the pp reference for the two different energies can be obtained using the interpolated values for $\langle p_\mathrm{T}\rangle$ and $\mathrm{d}\sigma/\mathrm{d}y$ in Tab. 5.2 and the function in Eq. (5.6) with its uncertainties. The p_T interpolated distributions and their uncertainty bands for mid-rapidity are compared to the existing data in Fig. 5.6.
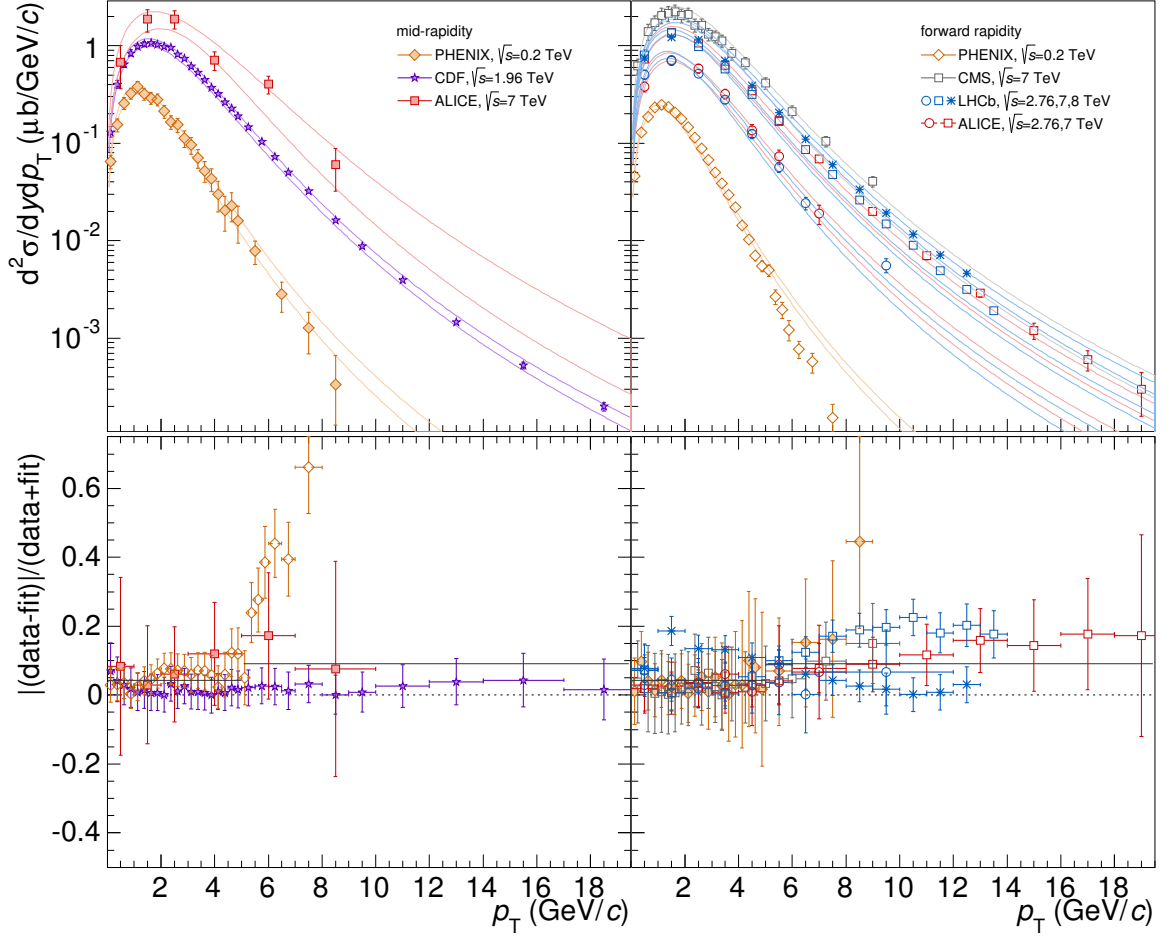
Figure 5.5.: Top panels: Universal fits compared to experimental data. Bottom panels: Ratio used for systematic uncertainty evaluation.

The values for the p_T intervals at $\sqrt{s} = 2.76$ TeV used in this analysis are given in Tab. 5.3.

p_T (GeV/c)	$d\sigma/dy$ (µb)
$0 < p_T < 2.5$	$2.455 \pm 0.110 \pm 0.298$
$2.5 < p_T < 6$	$1.609 \pm 0.079 \pm 0.195$

Table 5.3.: The differential cross section for pp collisions at $\sqrt{s} = 2.76$ TeV at mid-rapidity used for the p_T-dependent R_{AA} calculation. Uncorrelated and correlated systematic uncertainties are noted consecutively.
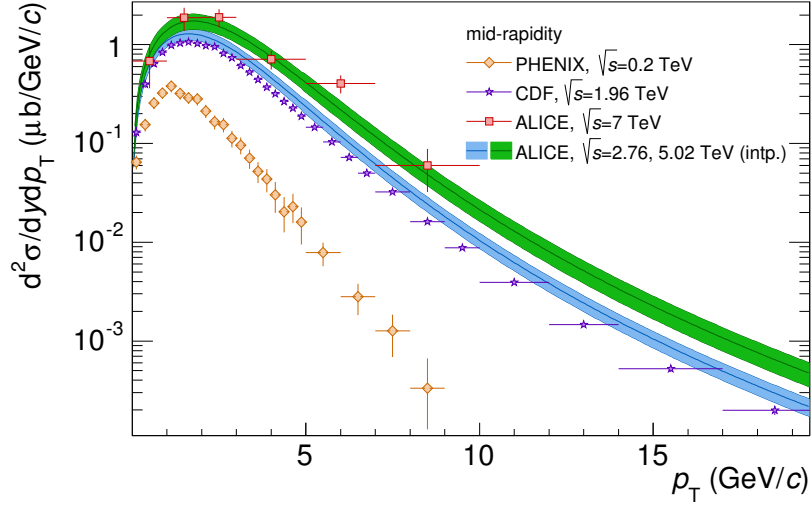
Figure 5.6.: Double differential cross-sections compared to the interpolation results at $\sqrt{s} = 2.76$ TeV and $\sqrt{s} = 5.02$ TeV.

5.1.3. Systematic Uncertainties

In this section the different contributions to the systematic uncertainties in the two p_{T}-intervals are discussed. They are summarized in Tab. 5.4 for the p_{T} intervals studied. In comparison to the p_{T}-integrated R_{AA} analysis, the type of systematic uncertainties (correlated (I), uncorrelated (II)) changes, e.g. the normalization and MC input kinematics.

Uncertainty (%)	p_{T} interval (GeV/c)		Type
	$p_{\mathrm{T}} < 2.5$	$2.5 < p_{\mathrm{T}} < 6.0$	
Signal extraction	± 10.9	± 11.0	II
MC input kinematics	± 3.2	± 5.9	II
Nuclear overlap	± 3.6	± 3.6	I
pp reference	± 12.1	± 12.1	I
	± 4.5	± 4.9	II
Total	± 12.7	± 12.7	I
	± 12.3	± 13.5	II

Table 5.4.: Systematic uncertainties on the R_{AA} versus p_{T} for the 40% most central events. The type specifies whether the uncertainty is correlated (type I) or uncorrelated (type II) between the p_{T} intervals.

For the J/ψ reconstruction and signal extraction uncertainty exactly the same variations of track selections as for the p_T-integrated analysis are done. Then the corresponding normalized yields obtained via the mixed-event technique are corrected in the usual way for the geometrical acceptance, efficiency and branching ratio. Fig. 5.7 shows the systematic variations for the two p_T-intervals with the assigned systematic uncertainties (dashed lines).
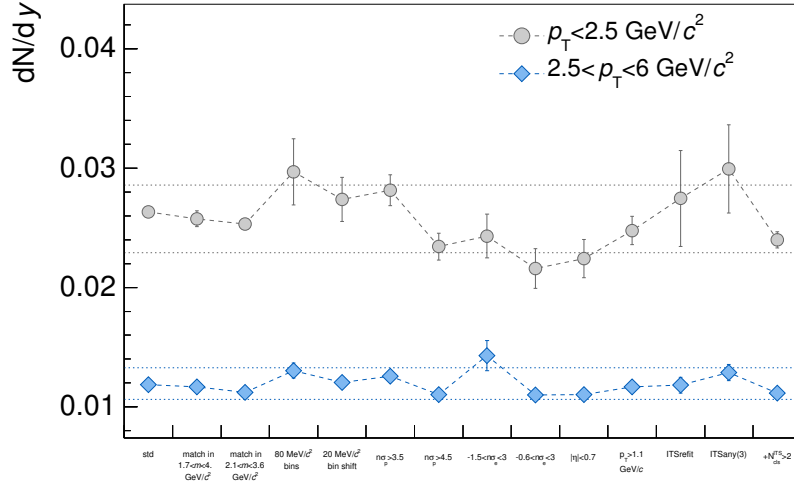

Figure 5.7.: Systematic variations for the different p_T intervals.

The procedure to obtain the impact of the input p_T-distribution for the MC simulation is described in Sec. 4.6.2. For the two p_T-intervals this study is repeated using the p_T-dependent $\langle A \times \epsilon \rangle$ for the collision centrality in the range $0 - 40\%$. The systematic uncertainties from this source are uncorrelated (type II) and quoted in Tab. 5.4.

The interpolation done for the p_T-differential pp cross-section is described in Sec. 5.1.2. For this part of the normalization a correlated and uncorrelated uncertainty is evaluated. Due to the non-flatness of the centrality distribution in large centrality intervals a weighting according to Eq. (5.1) at the level of the invariant mass distribution was necessary. As a consequence, the underlying centrality distribution corresponds to the one from minimum bias data taking, and the average nuclear overlap is calculated with the values of [92]. The $\langle T_\text{AA} \rangle$ for the 40% most central events is quoted in Tab. 4.2 of Sec. 4.2.1 with an uncertainty of $\pm 3.6\%$.

5.1.4. Results

In order to account for the rather large p_T-intervals, the R_AA result is not quoted at the center of the interval, but at the corrected average p_T. The $\langle p_\mathrm{T} \rangle = 1.54 \pm 0.04(\mathrm{stat.}) \pm 0.06(\mathrm{syst.})$ for $p_\mathrm{T} < 2.5$ GeV/c and $\langle p_\mathrm{T} \rangle = 3.30 \pm 0.05(\mathrm{stat.}) \pm 0.07(\mathrm{syst.})$ for $2.5 < p_\mathrm{T} < 6$ GeV/c are obtained via the method described in Sec. 5.2.

The p_T-dependence of the nuclear modification factor of inclusive J/ψ production in Pb-Pb at $\sqrt{s_\mathrm{NN}} = 2.76$ TeV for the 40% most central collisions is depicted in Fig. 5.8 for the mid-rapidity and forward rapidity region (published in [132]). Both results exhibit a similar suppression pattern with less suppression at low p_T, as expected from the comparison to the high-p_T R_AA measurement by the CMS collaboration (see Sec. 5.1.4). This result points to a contribution of J/ψ production via the recombination mechanism, and is further emphasized in the comparison to lower energy results (see below).
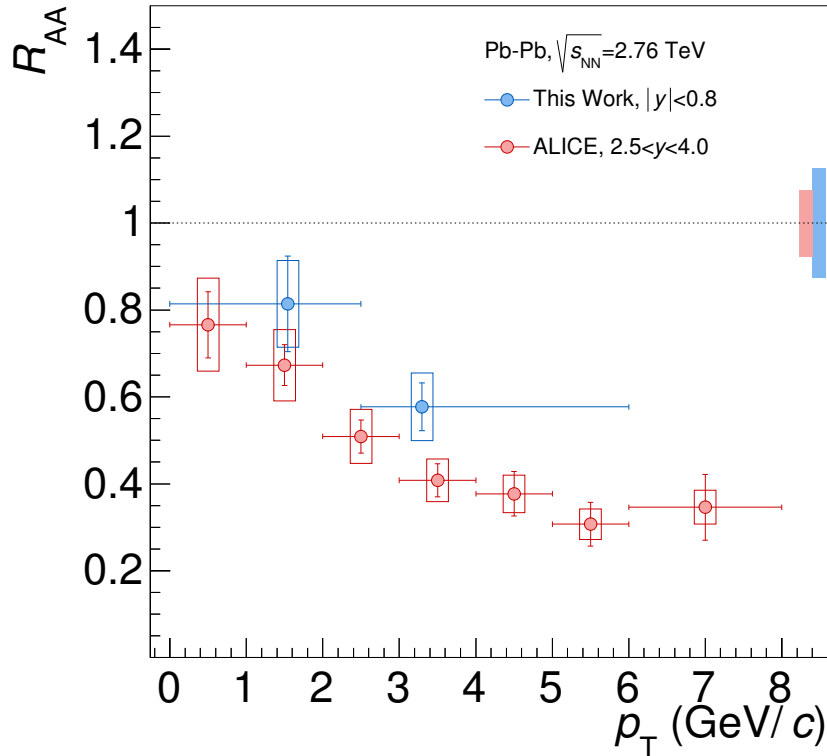

Figure 5.8.: The inclusive J/ψ R_AA as a function of transverse momentum compared to the ALICE measurement published in [132]. Open boxes correspond to the uncorrelated uncertainties between the points, while the correlated uncertainties are indicated by the coloured boxes.

Comparison to Other Measurements

The p_{T}-dependence of J/ψ production in Au-Au collisions at lower energy, $\sqrt{s_{\mathrm{NN}}} = 0.2$ TeV, was reported by the PHENIX [129] and STAR collaborations [135, 153], see Fig. 5.9. Remarkably less suppression at $\sqrt{s_{\mathrm{NN}}} = 2.76$ TeV than at $\sqrt{s_{\mathrm{NN}}} = 0.2$ TeV is observed at low p_{T} that might indicate a substantial contribution from charm quark recombination at the LHC. The R_{AA} measured at RHIC increases towards high-p_{T} and is compatible with unity above 4-6 GeV/c. This behaviour is not found at LHC energies. The published inclusive J/ψ R_{AA} [154] reported by the CMS collaboration for $|y| < 2.4$, see Fig. 5.9 (left), show a strong suppression ($R_{\mathrm{AA}} \approx 0.3$). A reasonable connection of the R_{AA} for $p_{\mathrm{T}} > 6.5$ GeV/c to the results of this work is found, despite the different centrality intervals. At high-p_{T}, J/ψ should dominantly be characterized by energy loss (Debye screening) on the initial J/ψ production, since the probability for $c\bar{c}$ coalescence decreases for increasing quark momentum differences. Towards very high-p_{T} the R_{AA} should increase due to the fact that the relative velocity between the resonance and deconfined expanding medium reduces the Debye screening potential which consequently leads to larger dissociation temperatures for the different $c\bar{c}$ states at high transverse momentum [155].
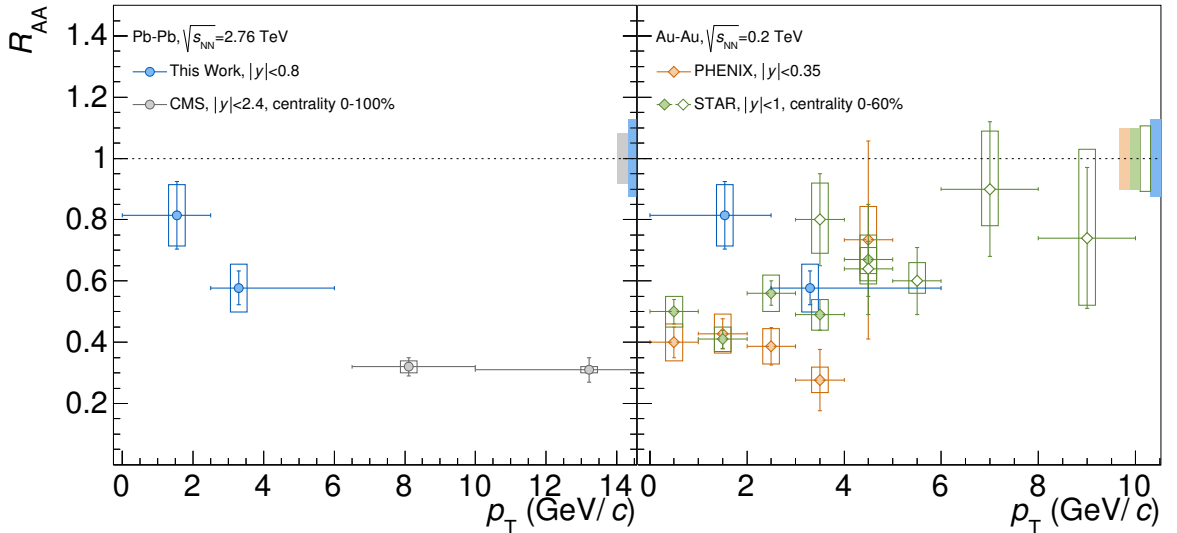

Figure 5.9.: Comparison to the p_{T} measurement of inclusive J/ψ R_{AA} at mid-rapidity reported by PHENIX, STAR and CMS, see text for details. Open (filled) boxes correspond to the uncorrelated (correlated) uncertainties of the measurements.

Comparison to Theory

In order to understand the combination and contributions of the different production mechanisms, comparisons to theory predictions [67, 139] are illustrated in Fig. 5.10. Both transport models suggest a dominant contribution from charm quark coalescence (dashed lines) at low p_T. Since the effect of gluon shadowing on the overall J/ψ production is insufficiently known, the model quote this uncertainty as band. Both models can qualitatively describe the trend in the data.
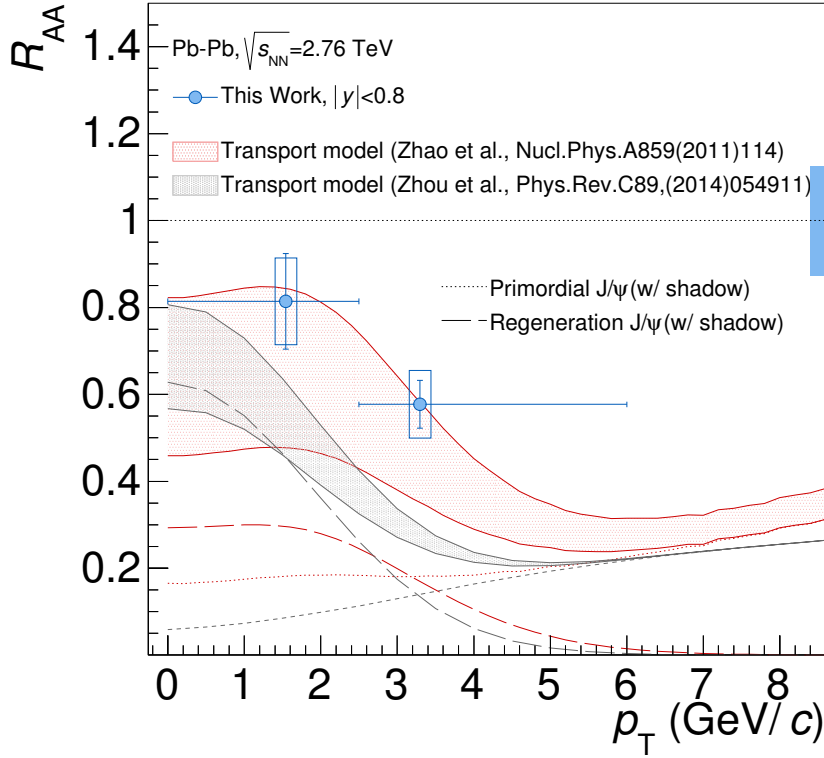

Figure 5.10.: The inclusive J/ψ R_{AA} as a function of transverse momentum compared to transport model predictions.

Comparison to Expected Cold-Nuclear-Matter Effects

For the quantification of the cold-nuclear matter effects in the observed J/ψ suppression in Pb-Pb collisions, p-Pb results discussed in [156] are used. The expected CNM effects in Pb-Pb can be expressed as $R_{p\text{-}Pb}^2 = R_{p\text{-}Pb} \times R_{p\text{-}Pb}$, assuming that (i) the J/ψ production process occurs through gluon fusion (ii) CNM effects are dominated by gluon shadowing (iii) the dominant kinematics is g + g → J/ψ (2 → 1 kinematics). In this situation, the

Bjorken x_{B}-values (see Tab. 5.5) of the initial gluons in the probed lead nucleus are similar in Pb-Pb and p-Pb collisions, despite the different energy and shifted rapidity intervals in p-Pb. In this scheme (see Fig. 5.11), the comparison of $R_{\mathrm{Pb\text{-}Pb}}$ with the extrapolation of CNM effects shows a hint for J/ψ enhancement relative to CNM in Pb-Pb collisions at lower transverse momentum.

		System	
Quantity		p-Pb	Pb-Pb
$\sqrt{s_{\mathrm{NN}}}$	(TeV)	5.02	2.76
rapidity interval		$-1.37 < y < 0.43$	$\lvert y \rvert < 0.9$
x_{B}	$(\times 10^{-3})$	$(0.2 - 2.4)$	$(0.5 - 2.8)$

Table 5.5.: Bjorken x_{B} values correspond to J/ψ production at $p_{\mathrm{T}} = 0$ for the different rapidity intervals and energies of p-Pb and Pb-Pb collisions in the ALICE Central-Barrel.
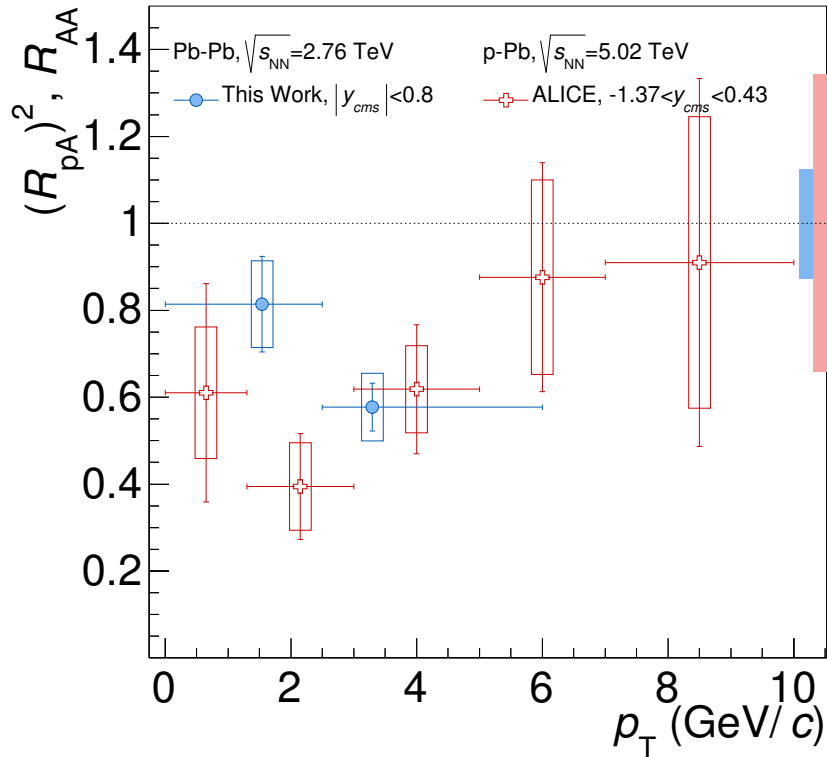

Figure 5.11.: The inclusive J/ψ R_{AA} and $R^2_{\mathrm{p\text{-}Pb}}$ versus p_{T} for mid-rapidity.

5.2. Average Transverse Momentum

A different way to study the kinematic properties of J/ψ production in nucleon-nucleon compared to nucleus-nucleus collisions is given by the p_{T}-distributions. The first ($\langle p_{\mathrm{T}} \rangle$) and second moment ($\langle p_{\mathrm{T}}^2 \rangle$) of the distribution in pp and A-A collisions allows to disentangle the different effects that might occur in medium, as discussed in Chapter 2. The statistics is not sufficient to extract the $\langle p_{\mathrm{T}} \rangle$ and $\langle p_{\mathrm{T}}^2 \rangle$ by fitting the J/ψ p_{T}-distribution or numerical calculation. Therefore a different approach based on the invariant mass distribution of $\langle p_{\mathrm{T}} \rangle$ and $\langle p_{\mathrm{T}}^2 \rangle$, inspired by the elliptic flow extraction technique [157], is followed.

5.2.1. Signal Extraction

Fig. 5.12 shows the distribution of the transverse momentum for SE and ME dielectron pairs in the typical J/ψ mass integration window ($2.92 < m_{\mathrm{inv}} < 3.16$ GeV/c^2). Over a broad range reasonable matching between both is found, which indicates that in addition to the invariant mass description, the mixed-event technique also matches the p_{T} distribution of same events which is dominated by uncorrelated background (very low S/B). Furthermore the invariant mas distribution of $\langle p_{\mathrm{T}} \rangle$ obtained in mixed events matches very good the same event distribution (see App. C).

For the extraction of the $\langle p_{\mathrm{T}} \rangle$ and $\langle p_{\mathrm{T}}^2 \rangle$ the invariant mass distributions, illustrated in Figs. 5.13 and 5.14, are fitted in the region $2.32 < m_{\mathrm{inv}} < 3.76$ GeV/c^2 by taking into account the mass dependent S/B ratio obtained via the standard signal extraction method (see Sec. 4.3.3). The corresponding functional form of the $\langle p_{\mathrm{T}} \rangle$ fit as a function of m_{inv} is given in Eq. (5.7):

$$\langle p_{\mathrm{T}}^{S+B} \rangle = \frac{S \cdot \langle p_{\mathrm{T}}^{\mathrm{J}/\psi} \rangle + B \cdot \langle p_{\mathrm{T}}^{B} \rangle}{S + B} \tag{5.7}$$

where $B(m_{\mathrm{inv}})$ and $\langle p_{\mathrm{T}}^{B} \rangle(m_{\mathrm{inv}})$ (obtained via mixed events) are adjusted to the opposite-sign spectrum of the same-event distribution in the usual intervals ($1.5 < m_{\mathrm{inv}} < 2.5$ GeV/c^2 and $3.2 < m_{\mathrm{inv}} < 4.2$ GeV/c^2). For $S(m_{\mathrm{inv}})$ the background subtracted signal distribution is used, while for the denominator $S + B$ the measured opposite-sign invariant mass distribution is applied. In the analysis of the transverse momentum dependence (see Sec. 5.1) is was observed that for $p_{\mathrm{T}} > 10$ GeV/c no significant signal is seen and mainly background contributes to the mass spectrum. Therefore the calculation of $\langle p_{\mathrm{T}} \rangle$ and
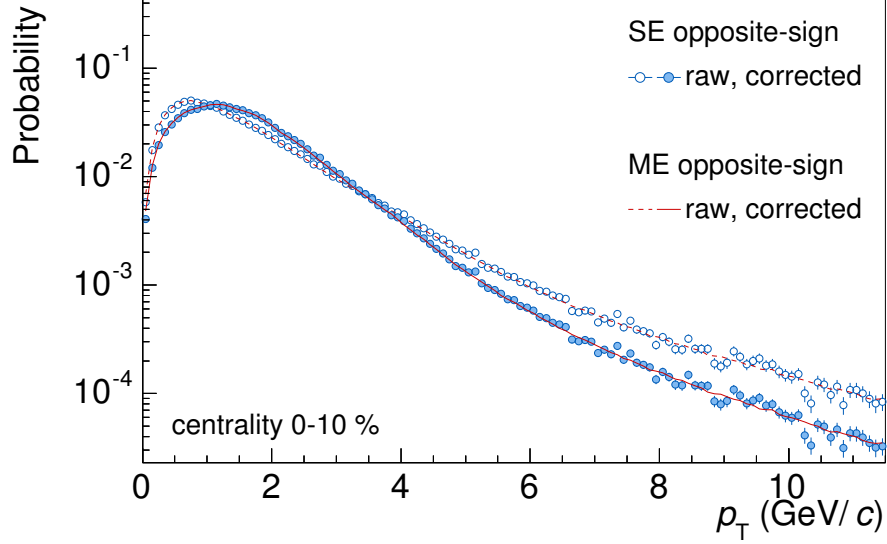
Figure 5.12.: The p_T distribution in the invariant mass range $2.92 < m_{\text{inv}} < 3.16\,\text{GeV}/c^2$ of same and mixed events.

$\langle p_T^2 \rangle$ is limited to this range. Due to the low S/B (1.5% (central) to 24.5% (peripheral)) and the limited statistic no prominent excess compared to the background can be seen in Figs. 5.13 and 5.13. In MC simulations, a closure test is performed. The true S/B-ratio as obtained in collision data, is constructed by randomly rejecting J/ψ particles of the enhanced MC sample. In the next step the same selection criteria as for the efficiency calculation are applied to the particles. Then the pairing of electron candidates in MC for same and mixed events is performed in the usual way. Finally the signal distribution is fitted and the expected $\langle p_T \rangle$, $\langle p_T^2 \rangle$ is successfully extracted for central collisions.
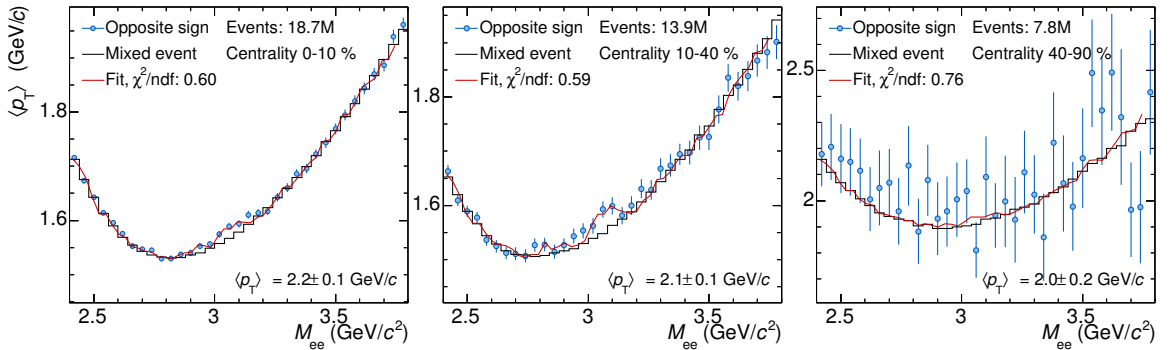

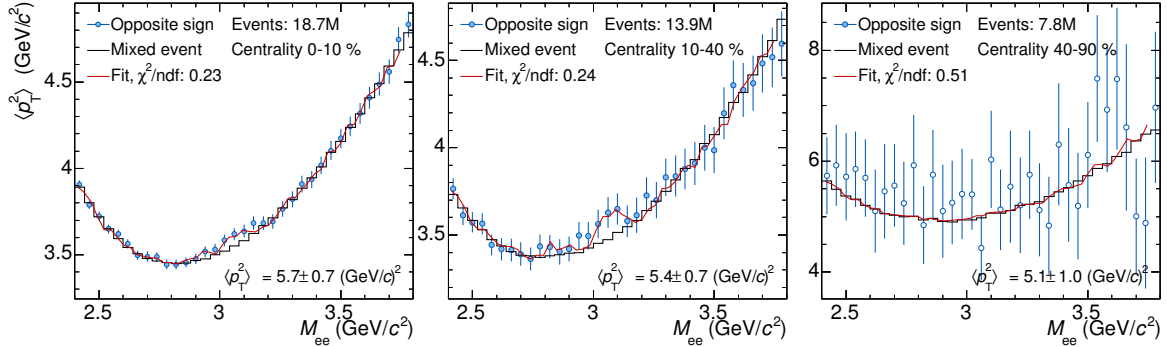**Figure 5.13.:** J/ψ $\langle p_T \rangle$ extractions in the three centrality intervals.

Figure 5.14.: J/ψ $\langle p_T^2 \rangle$ extractions in the three centrality intervals.

5.2.2. Corrections

According to Sec. 4.4, the track quality selection cuts act differently on J/ψ daughters and background tracks. Furthermore the $\langle A \times \epsilon \rangle$ varies strongly with transverse momentum, as discussed there. As a consequence a correction of the $\langle p_T \rangle$ and $\langle p_T^2 \rangle$ is necessary, which leads to a change of the p_T-distribution properties ($\langle p_T \rangle > \langle p_T \rangle_{\mathrm{raw}}$, $\langle p_T^2 \rangle < \langle p_T^2 \rangle_{\mathrm{raw}}$) as depicted in Fig. 5.12.
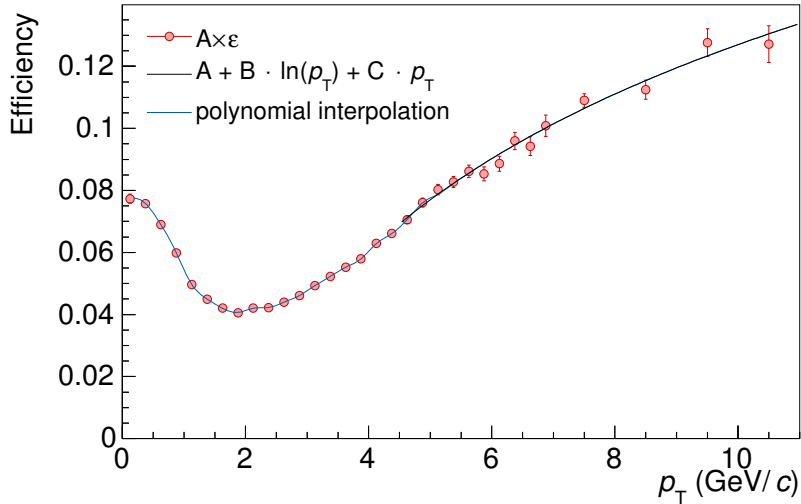

Figure 5.15.: The total efficiency of prompt J/ψ versus transverse momentum. For "on-the-fly"-corrections, polynomial interpolations (low p_T) and a logarithmic function (high p_T) is deployed.

The correction is applied "on-the-fly" to the combined SE and ME pairs, meaning that for each individual $e^+ e^-$-pair the efficiency correction of Fig. 5.15 is taken as a weight according to Eq. (5.8).

$$\langle p_\mathrm{T}^{obs} \rangle (m_\mathrm{inv}) = \frac{\sum\limits_{i}^{N_\mathrm{pairs}} p_\mathrm{T}^i(m_\mathrm{inv})/\langle A \times \epsilon \rangle (p_\mathrm{T}^i)}{\sum\limits_{i}^{N_\mathrm{pairs}} 1/\langle A \times \epsilon \rangle (p_\mathrm{T}^i)} \tag{5.8}$$

Advantage of such a procedure is, that the MC input kinematics of the J/ψ at the generator level do no longer constitute a systematic uncertainty on the average efficiency, as evaluated in Sec. 4.6, provided that the binning is small enough. In order to ensure this, the p_T distribution of $\langle A \times \epsilon \rangle$ was described by reasonable interpolations (3rd order polynomials, between the points for $p_\mathrm{T} < 5$ GeV/c and a logarithmic function for $p_\mathrm{T} > 5$ GeV/c). This correction is already applied to the invariant mass spectra shown in Figs. 5.13 and 5.14. As a consequence the extracted $\langle p_\mathrm{T} \rangle$ and $\langle p_\mathrm{T}^2 \rangle$ are corrected observables. As mentioned in Sec. 4.4, for the most peripheral interval $(40 - 90\%)$, the efficiency was calculated based on the non-radiative J/ψ decay only. In order to account for the radiative decay in the correction of this centrality interval, the p_T-dependent adjustment defined as the ratio of $\epsilon_\mathrm{non-rad.}/\epsilon_\mathrm{prompt}$ (shown in Fig. 5.16) is applied to the efficiency. The transverse momentum dependence of the ratio can be understood by two effects (i) the geometrical acceptance for the three-body (radiative) J/ψ decay is lower, due to the smaller $\langle p_\mathrm{T} \rangle$ of the daughter tracks and the imposed p_T-cut. Towards higher J/ψ p_T the acceptance increases reaches the values for non-radiative J/ψ decays. (ii) in the J/ψ reconstruction the invariant mass resolution for J/ψ $\to$ e$^+$e$^-\gamma$ is biased due to the absence of the photon energy. At low p_T the m_inv-distribution is only slightly broader for radiative decays, while the missing photon energy has a stronger impact on the width of the distribution with increasing p_T and saturates for J/ψ $p_\mathrm{T} \approx 3.5$ GeV/c.

5.2.3. Systematic Uncertainties

The sources of the systematic uncertainties of this analysis, can be divided into signal extraction, track selection and MC fit systematic (see Tab. 5.6). In a MC closure the extracted $\langle p_\mathrm{T} \rangle$, $\langle p_\mathrm{T}^2 \rangle$ results are compared to the known value and consistency within 2% is found. The variation of the track selection criteria are done in the same fashion as for the centrality and p_T dependent R_AA analyses. The results can be found in Fig. 5.17b for $\langle p_\mathrm{T} \rangle$ and Fig. 5.18b for $\langle p_\mathrm{T}^2 \rangle$ and as expected show the largest sensitivity to changes of the PID selection. In addition the variation of the results with respect to the fitting
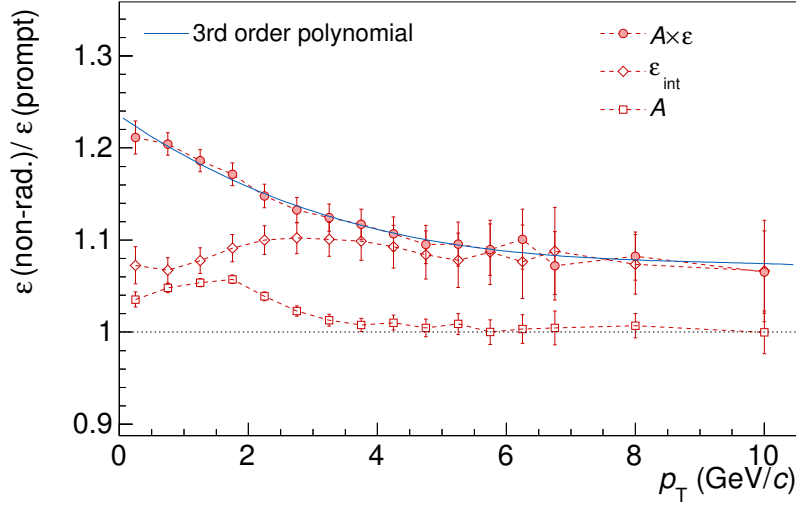
Figure 5.16.: Ratio of partial efficiencies for non-radiative and prompt J/ψ decays versus transverse momentum.

process and the functional form for the background are evaluated. For this the matching region of the ME to the SE distribution and the bin width are varied, as well as the bin edges of the invariant mass spectra are shifted by 20 MeV/c^2. Furthermore, the number of degrees of freedom for the background fit is increased by multiplication of a 1st order polynomial $((A + Bm_{\text{inv}}) \cdot \langle p_{\text{T}}^B \rangle (m_{\text{inv}}))$ to the ME background. The fit range used to extract the $\langle p_{\text{T}} \rangle$ and $\langle p_{\text{T}}^2 \rangle$ is changed within reasonable limits and for symmetric and non-symmetric intervals around the J/ψ mass.

| Uncertainty (%) | Centrality (%) | | | | | | Type |
| | 0-10 | | 10-40 | | 40-90 | | |
	$\langle p_{\text{T}} \rangle$	$\langle p_{\text{T}}^2 \rangle$	$\langle p_{\text{T}} \rangle$	$\langle p_{\text{T}}^2 \rangle$	$\langle p_{\text{T}} \rangle$	$\langle p_{\text{T}}^2 \rangle$	
Signal extraction	± 2.0	± 0.7	± 1.6	± 2.1	± 4.5	± 6.8	II
Track selection	± 3.1	± 4.0	± 3.9	± 6.6	± 13.7	± 22.9	II
MC fit systematic	± 2.0	± 2.0	± 2.0	± 2.0	± 2.0	± 2.0	I
Total	± 2.0	± 2.0	± 2.0	± 2.0	± 2.0	± 2.0	I
	± 3.7	± 4.1	± 4.2	± 6.9	± 14.4	± 23.9	II

Table 5.6.: Systematic uncertainties of the $\langle p_{\text{T}} \rangle$ and $\langle p_{\text{T}}^2 \rangle$ measurements. The type specifies whether the uncertainty is correlated (type I) or uncorrelated (type II) between the centrality intervals.
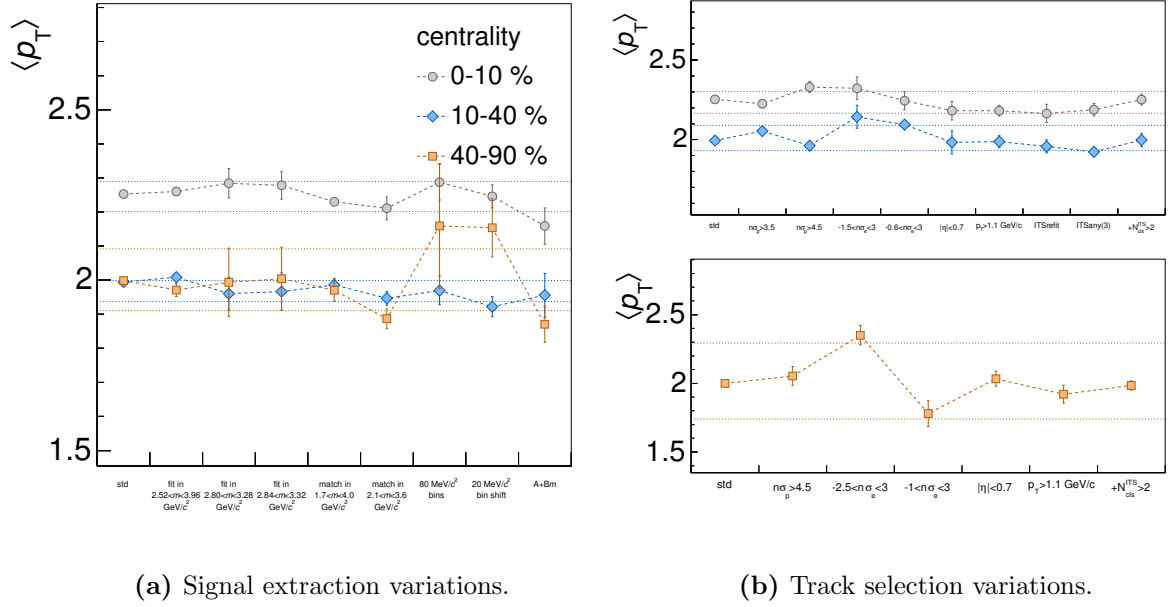
(a) Signal extraction variations.

(b) Track selection variations.

Figure 5.17.: The systematic uncertainties for the $\langle p_T \rangle$ analysis for the three centrality intervals. The statistical uncertainties of the points are the uncorrelated contributions with respect to the standard selection and signal extraction. The colored bands correspond systematic uncertainties assigned to the measurement.
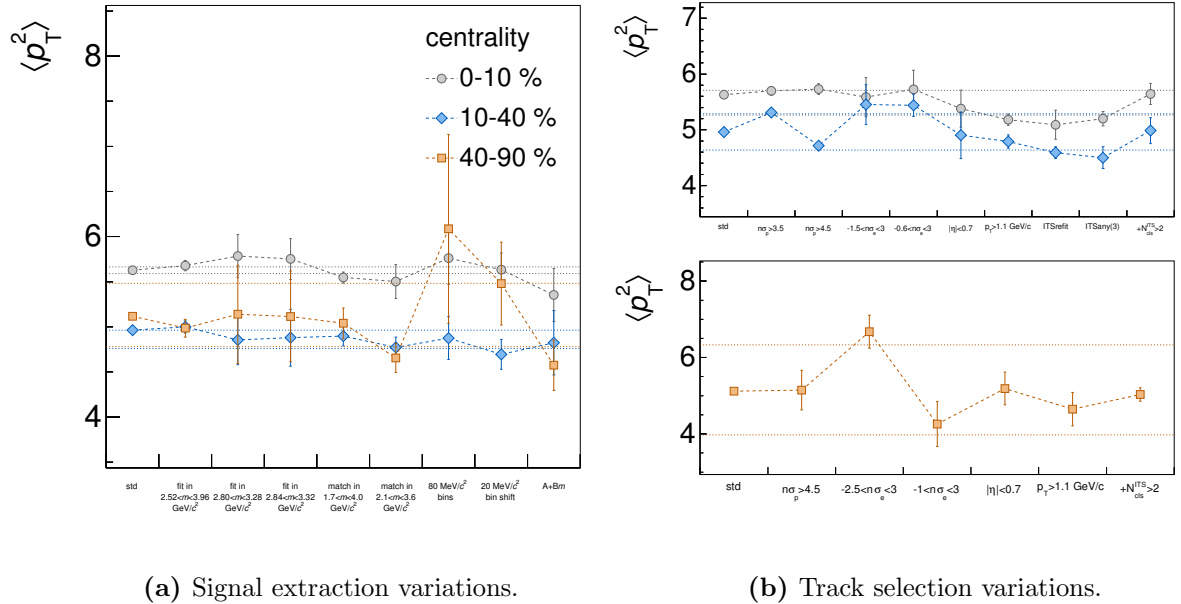

(a) Signal extraction variations.

(b) Track selection variations.

Figure 5.18.: The systematic uncertainties for the $\langle p_T^2 \rangle$ analysis for the three centrality intervals. The statistical uncertainties of the points are the uncorrelated contributions with respect to the standard selection and signal extraction. The colored bands correspond systematic uncertainties assigned to the measurement.

5.2.4. pp Reference

Since there is no mid-rapidity measurement of the first and second moment of the transverse momentum distribution in pp collisions at $\sqrt{s} = 2.76$ TeV, the interpolation result obtained in Sec. 5.1.2 is utilized to study final state effects. For the systematic uncertainty evaluation of the $\langle p_{\mathrm{T}} \rangle$ and $\langle p_{\mathrm{T}}^2 \rangle$, the covariance matrix values of the pp interpolation function are randomly varied within one standard deviation. Furthermore, a partially correlated uncertainty needs to be assigned to the $\langle p_{\mathrm{T}} \rangle$ and $\langle p_{\mathrm{T}}^2 \rangle$ due to the average deviations $\langle \Delta(\sigma_{\mathrm{intp}}, \sigma_{\mathrm{meas}}) \rangle$ of the interpolation procedure to measured spectra at different energies (illustrated in Fig. 5.5 of Sec. 5.1.2). This shape uncertainty is addressed in the $\langle p_{\mathrm{T}} \rangle$ and $\langle p_{\mathrm{T}}^2 \rangle$ by randomly shifting σ_{intp} up or down within $\Delta(\sigma_{\mathrm{intp}}, \sigma_{\mathrm{meas}})$. As illustrated in Fig. 5.19 the $\langle p_{\mathrm{T}} \rangle$ and $\langle p_{\mathrm{T}}^2 \rangle$ values and systematic uncertainties depend strongly on the p_{T} interval used for their calculation. The calculation of $\langle p_{\mathrm{T}} \rangle$ for $p_{\mathrm{T}} < 10$ GeV/c covers already 98% of the true $\langle p_{\mathrm{T}} \rangle$ (dashed line). Values for $\langle p_{\mathrm{T}} \rangle$ and $\langle p_{\mathrm{T}}^2 \rangle$ with uncertainties obtained via the pp interpolations for $\sqrt{s} = 2.76$ and 5.02 TeV are quoted in Tab. 5.7.
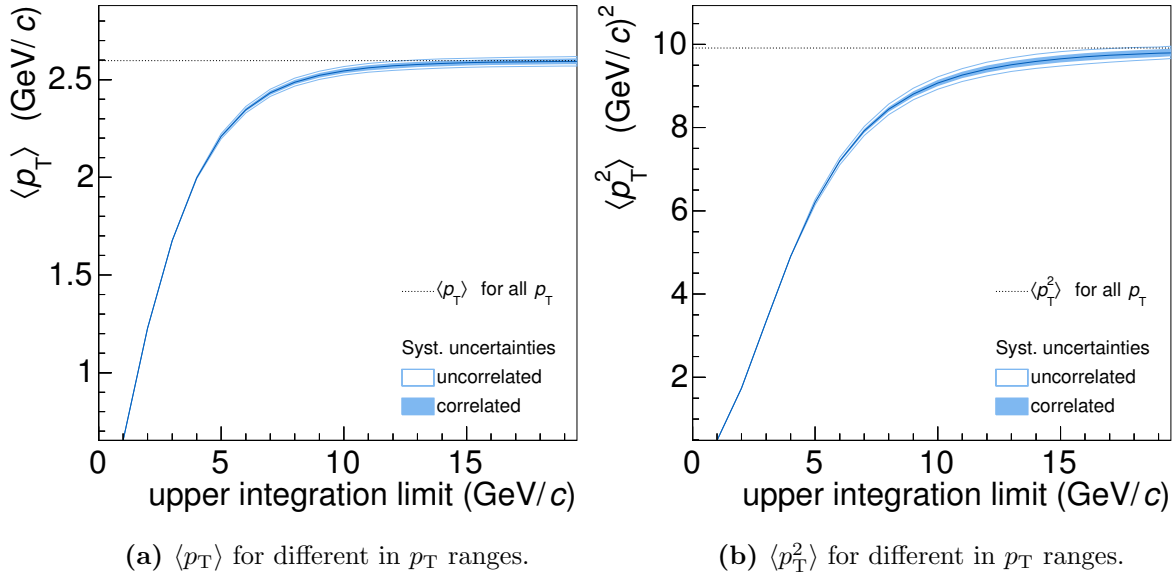

(a) $\langle p_{\mathrm{T}} \rangle$ for different in p_{T} ranges.   **(b)** $\langle p_{\mathrm{T}}^2 \rangle$ for different in p_{T} ranges.

Figure 5.19.: The $\langle p_{\mathrm{T}} \rangle$ and $\langle p_{\mathrm{T}}^2 \rangle$ for the mid-rapidity interpolation and pp collisions at $\sqrt{s} = 2.76$ TeV.

$\sqrt{s}$ (TeV)	$\langle p_{\mathrm{T}} \rangle$ (GeV/c)	$\langle p_{\mathrm{T}}^2 \rangle$ (GeV/c)^2
2.76	$2.544 \pm 0.018 \pm 0.012$	$9.072 \pm 0.148 \pm 0.074$
5.02	$2.689 \pm 0.094 \pm 0.021$	$10.417 \pm 0.345 \pm 0.090$

Table 5.7.: The $\langle p_{\mathrm{T}} \rangle$ and $\langle p_{\mathrm{T}}^2 \rangle$ values obtained in $p_{\mathrm{T}} < 10$ GeV/c for pp collisions at $\sqrt{s} = 2.76$ and 5.02 TeV at mid-rapidity.

5.2.5. Results

Fig. 5.20 show the N_{part}-dependence of the extracted $\langle p_{\mathrm{T}} \rangle$ and $\langle p_{\mathrm{T}}^2 \rangle$ in Pb-Pb collisions at $\sqrt{s_{\mathrm{NN}}} = 2.76$ TeV in comparison to the results obtained in the forward-rapidity region [158]. There the values are obtained by several fits to the p_{T} distributions in the range from $1 < p_{\mathrm{T}} < 8$ GeV/c. For $p_{\mathrm{T}} < 1(0.3)$ GeV/c an intriguing excess of J/ψ for peripheral events was found, that might hint to an electromagnetic production process and therefore was excluded from the $\langle p_{\mathrm{T}} \rangle$ calculation. The $\langle p_{\mathrm{T}} \rangle$ value for most central collisions at mid-rapidity is slightly larger, but all centrality intervals are compatible with the forward-rapidity measurements within the uncertainties. In comparison to the pp interpolation values (see Tab. 5.7 for $|y| < 0.8$ and $2.5 < y < 4$ [128]), a significant difference is found.
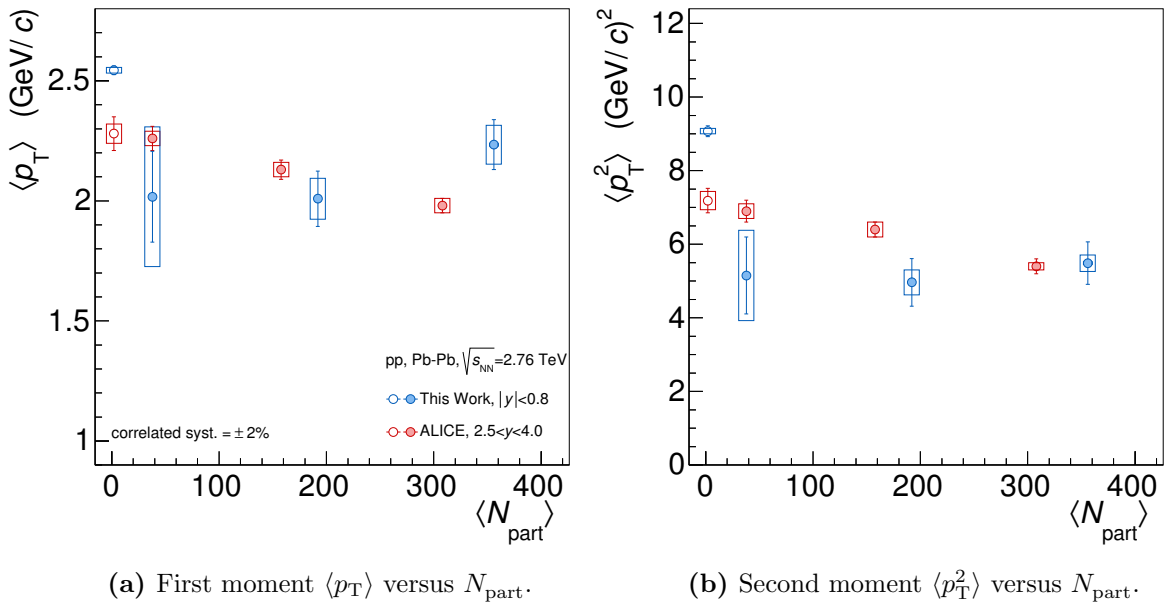

(a) First moment $\langle p_{\mathrm{T}} \rangle$ versus N_{part}.

(b) Second moment $\langle p_{\mathrm{T}}^2 \rangle$ versus N_{part}.

Figure 5.20.: Centrality dependence of the $\langle p_{\mathrm{T}} \rangle$ and $\langle p_{\mathrm{T}}^2 \rangle$ for mid- and forward-rapidity measurements in ALICE.

The results of the forward rapidity measurement show a monotonous decrease of $\langle p_\mathrm{T} \rangle$ = 2.3 GeV/c ($\langle p_\mathrm{T}^2 \rangle$) from pp collisions to peripheral, to central Pb-Pb collisions ($\langle p_\mathrm{T} \rangle$ = 2.0 GeV/c). The difference between the $\langle p_\mathrm{T} \rangle$ result of the pp interpolation and the centrality interval $0 - 10\%$ is about the same (300 MeV/c), but due to the large uncertainties no obvious dependence on N_part can be seen. The change of $\langle p_\mathrm{T}^2 \rangle$ from pp collisions to central Pb-Pb collisions is more pronounced than for $\langle p_\mathrm{T} \rangle$. At mid-rapidity the pp result differs by almost $2(\mathrm{GeV}/c)^2$ to the value in $2.5 < y < 4$, while the $\langle p_\mathrm{T}^2 \rangle$ for most central collisions are in agreement (see Fig. 5.20b). The differences of $\langle p_\mathrm{T} \rangle$ and $\langle p_\mathrm{T}^2 \rangle$ in pp collisions to Pb-Pb collisions can possibly be interpreted as a recombination effect, which is dominant at low p_T due to the smaller momentum differences of the c and $\bar{\mathrm{c}}$ which are favourable for J/ψ formation. In [65] narrower p_T-distributions with increasing energy density are predicted based on $\langle p_\mathrm{T}^2 \rangle$ calculations for two different charm quark momentum distributions (from pQCD and thermal equilibrium). Since pp and Pb-Pb results are definitely incompatible the effect of exclusive J/ψ production in the corona and full dissociation in the core is ruled out as explained in Sec. 2.2.2.

Comparison to Other Measurements

For lower energy measurements at mid-rapidity by the PHENIX [83, 129, 143] and STAR collaborations [135, 153] at $\sqrt{s_\mathrm{NN}} = 0.2$ TeV, and NA50 [159] at $\sqrt{s_\mathrm{NN}} = 0.173$ TeV, the centrality dependence, shown in Fig. 5.21, look significantly different and show a flat, resp. increasing trend. These PHENIX and NA50 measurements were performed for $p_\mathrm{T} < 5$ GeV/c, so high p_T J/ψ particles might not be sufficiently represented in the $\langle p_\mathrm{T} \rangle$. However, a Kaplan (Boltzmann) fit to the underlying p_T-distribution shows that 98(99)% of the cross-section is covered in the PHENIX (NA50) result. In this context, the $\langle p_\mathrm{T} \rangle$ and $\langle p_\mathrm{T}^2 \rangle$ behaviour seen at LHC energies is comparable with lower centre-of-mass energy results and might indicate that processes either deplete the region of high J/ψ p_T or substantially enhance the J/ψ production at low p_T as expected from J/ψ recombination.

Comparison to Theory

In Fig. 5.22 the results of this analaysis are compared to predictions by the two kinematic transport models [67, 160]. For both model predictions the $\langle p_\mathrm{T}^2 \rangle$ and $\langle p_\mathrm{T} \rangle$ in central Pb-Pb collisions at mid-rapidity is lower compared to pp collisions at the same centre-of-mass energy. A reasonable agreement with the results of this work is observed, although the
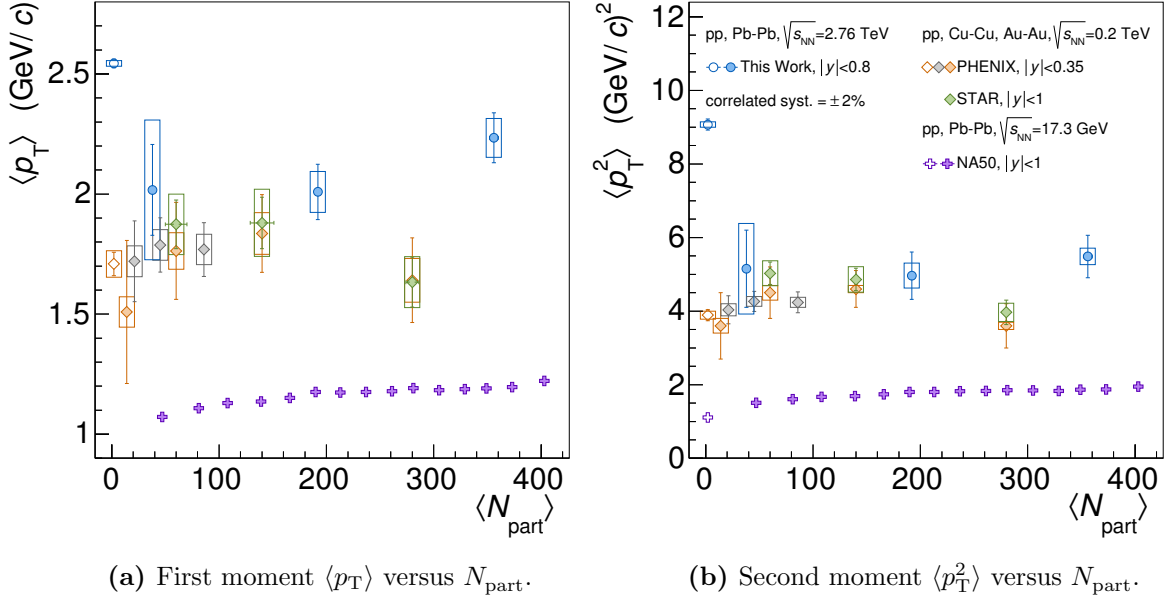
(a) First moment $\langle p_\text{T} \rangle$ versus N_part. **(b)** Second moment $\langle p_\text{T}^2 \rangle$ versus N_part.

Figure 5.21.: System-size dependence of $\langle p_\text{T} \rangle$ and $\langle p_\text{T}^2 \rangle$ for mid-rapidity measurements by the PHENIX, STAR and NA50 collaborations.

predictions are systematically above the data. For [160] the contribution of primordial J/ψ (dotted) and recombination (dashed) to the $\langle p_\text{T} \rangle$ and $\langle p_\text{T}^2 \rangle$ are shown as a function of N_part. The stronger radial flow in larger systems is transferred to the charm quarks in the case of a QGP. Therefore, the first and second moment of the p_T distribution for the recombination component grow with increasing centrality, while the primordial J/ψ $\langle p_\text{T} \rangle$ and $\langle p_\text{T}^2 \rangle$ are almost constant from pp to central Pb-Pb collisions. This implies that for the description of the $\langle p_\text{T} \rangle$ and $\langle p_\text{T}^2 \rangle$ in data using the transport model approach the recombination mechanism is crucial.

Nuclear Modification Factor of $\langle p_\text{T}^2 \rangle$

A promising quantity to separate hot from cold nuclear matter effects, is given by the nuclear modification factor of the second moments of the transverse momentum distributions [161]:

$$r_\text{AA} = \langle p_\text{T}^2 \rangle_\text{A-A} / \langle p_\text{T}^2 \rangle_\text{pp} \tag{5.9}$$

At mid-rapidity the energy density is the highest, hot nuclear matter effects are most prominent and the r_AA should change the most with increasing centrality. Fig. 5.23 shows the measurement of r_AA for SPS, RHIC and LHC energies with the comparison to the

(a) First moment $\langle p_{\mathrm{T}} \rangle$ versus N_{part}.   (b) Second moment $\langle p_{\mathrm{T}}^2 \rangle$ versus N_{part}.
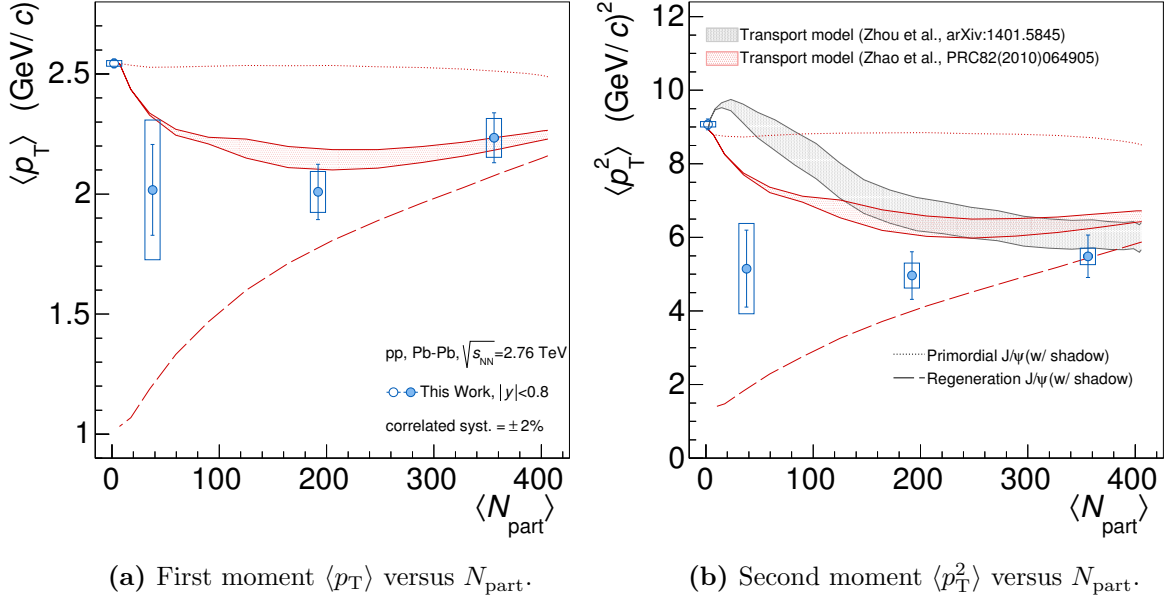
Figure 5.22.: Comparison to predictions by the transport model calculations.

transport model calculations [67, 139, 160]. Good agreement between model calculations and data is observed for SPS and RHIC collision energies. The results of this work are in qualitative agreement with the model predictions and the evolution of r_{AA} can be interpreted as the following:

SPS result: At $\sqrt{s_{\mathrm{NN}}} = 17.3$ GeV almost all measured J/ψ are produced through the initial hard scattering processes. The monotonic increase of r_{AA} with centrality is caused by the Cronin effect and is interrupted at most central collisions due to the escape of high-p_{T} J/ψ particles from the interaction with comovers (leakage).

RHIC result: At $\sqrt{s_{\mathrm{NN}}} = 0.2$ TeV, initial production and recombination of J/ψ become equally important. The J/ψ suppression is largely canceled by this, which leads to a flat r_{AA} around unity and the similar magnitude of R_{AA}.

LHC result: At $\sqrt{s_{\mathrm{NN}}} = 2.76$ TeV, J/ψ production is dominated by recombination, in particular for central collisions. According to this more and more low-p_{T} J/ψ with respect to pp collisions are measured resulting in the drop of r_{AA} below unity.
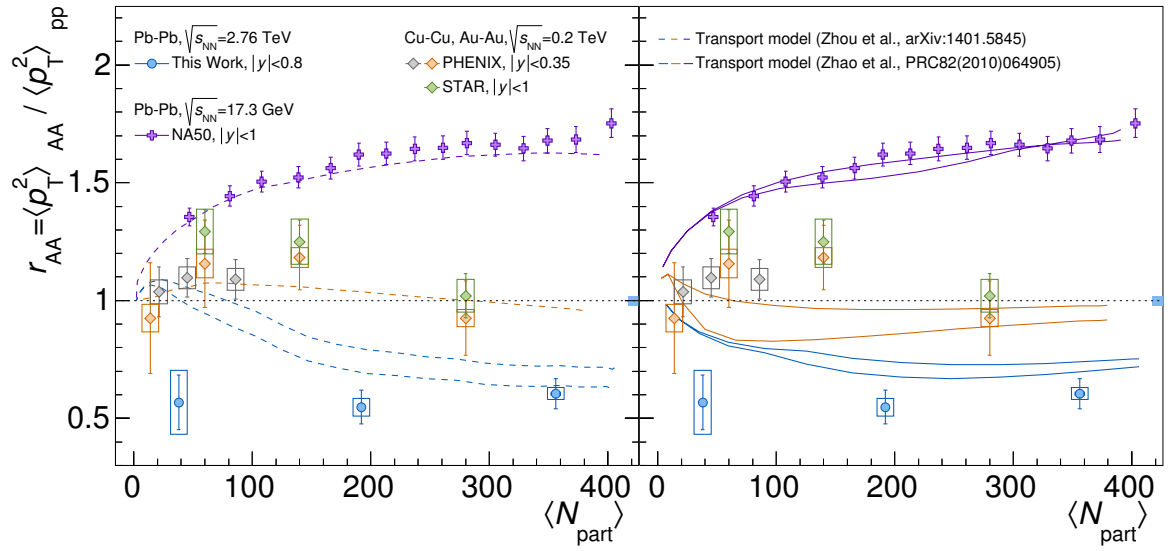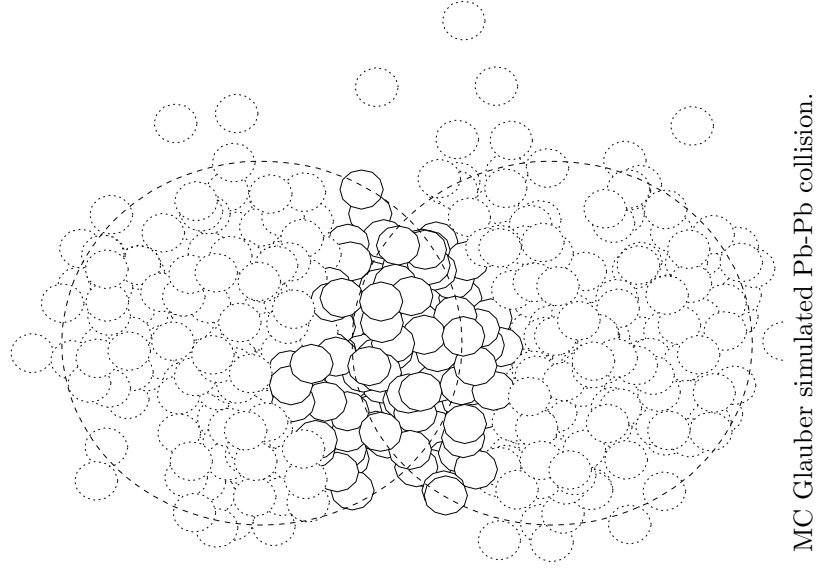
Figure 5.23.: Experimental and theoretical results of the nuclear modification factor of $\langle p_T^2 \rangle$ at mid-rapidity as a function of the system size.

Chapter 6.

Azimuthal Dependence of J/ψ Production

Elliptic flow originates from the initial geometric eccentricity of two colliding nuclei. The largest significance for flow is expected at intermediate collision centrality $10 < \mathscr{C} < 50\%$, where the event plane resolution, for the same reason, is the highest. If J/ψ production only happens at the initial state and before the formation of a hot medium, then no J/ψ v_2 will be present, since hard processes do not have any information about the geometry of the collision. However, according to transport model predictions including J/ψ recombination at LHC energies[66, 67], a prominent J/ψ v_2 is expected at intermediate p_T and was confirmed by ALICE and CMS measurements[77, 78]. In the recombination picture, the flow of (thermalized) c and $\bar{\text{c}}$ quarks is transferred to the created J/ψ. In this chapter, a feasibility study on the elliptic flow extraction of J/ψ at mid-rapidity is presented. Two different v_2 signal-extraction techniques based on the event plane reconstruction, described in Sec. 4.2.2, are discussed. Finally, the statistics needed for a qualitative measurement of non-zero elliptic flow is estimated.

6.1. Signal Extraction

Usually, the azimuthal anisotropy of particles is studied in multiple bins of $\Delta\phi$, where the particle yields are measured as a function of the azimuthal angle ϕ relative to the event plane angle Ψ_n. The p_T-differential azimuthal distribution is then described by a Fourier series, according to Eq. (4.2). Fig. 6.1 shows the $\Delta\phi$ distribution of all e$^+$ e$^-$-pairs in the interval $1.5 < m_{\text{inv}} < 5$ GeV/c^2 compared to pairs from mixed events in the centrality

107

interval $10 - 50\%$ and for intermediate pair transverse momentum ($2 < p_\mathrm{T} < 6$ GeV/c). A very good description of the shape with the mixed event technique is found. As mentioned in Sec. 4.2 the TPC and ITS detectors have a non-uniform acceptance and efficiency in the azimuthal angle. In order to obtain the best rejection of secondary particles the ϕ-dependent ITS hit requirement (see Sec. 4.3.1) is imposed. This leads to an asymmetry in the $\Delta\phi$ distribution for an event plane angle defined in ($-\pi/2 < \Psi_2 < +\pi/2$). However, in the coordinate system of the event plane this asymmetry vanishes. The angle of any track is always in the range from 0 to $\pi/2$. This is illustrated in the sub-panel of Fig. 6.1, where the elliptic flow of all $\mathrm{e}^+ \mathrm{e}^-$-pairs (mainly uncorrelated background) is found to be $v_2 = 0.10 \pm 0.02$. Since the number of J/ψ counts in this sample is limited, the number of $\Delta\phi$-intervals are reduced to its minimum of two bins. Particles emitted in a cone in direction or perpendicular to the second order harmonic event plane orientation Ψ_2 are illustrated by the full and open marker respectively.
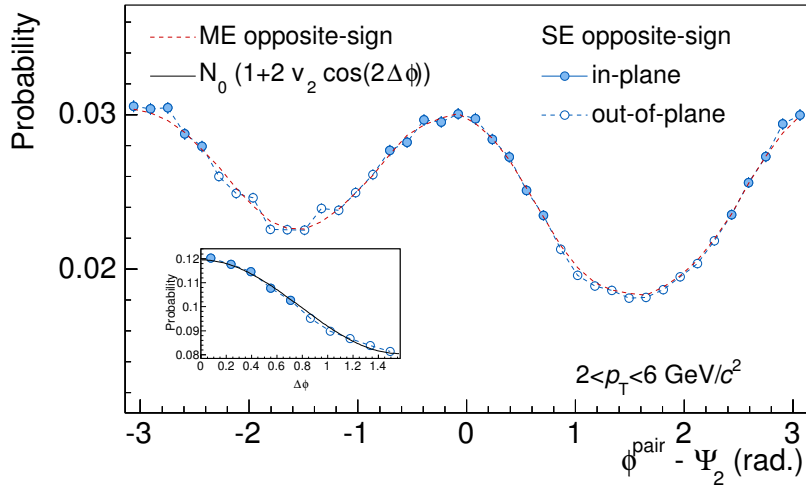

Figure 6.1.: The $\Delta\phi$ distribution of all opposite charged pairs in the invariant mass range $1.5 < m_\mathrm{inv} < 5$ GeV/c^2 for mixed and same events using the TPC event plane angle.

6.1.1. In- and Out-Of-Plane Method

The signal extraction "in-plane" and "out-of-plane" covers the information of the asymmetry of the particles emission in the azimuth w.r.t. Ψ_2. By integrating Eq. (4.2), it can

be shown that the elliptic flow is given by:

$$v_2 = \frac{1}{R_2} \frac{\pi}{4} \frac{S_{\text{in}} - S_{\text{out}}}{S_{\text{in}} + S_{\text{out}}},\tag{6.1}$$

where S_{in} (S_{out}) is the J/ψ yield extracted in $|\Delta\phi| < \pi/4$ ($\pi/4 < |\Delta\phi| < 3\pi/4$) and R_2 the event plane resolution correction factor obtained for the corresponding event plane detector (TPC,V0A,V0C).

In Sec. 4.2.2 the event plane resolution for the different detectors was derived from the Ψ_2 angle correlations between the detectors. The resolution in a large centrality interval (i.e. $10 < \mathscr{C} < 50\%$) requires special treatment, since the J/ψ signal is a rare probe and scales with the number of binary collisions (N_{coll}). Therefore, the bias towards central collisions needs to be considered. If the statistic is sufficient the average over a centrality interval of the event plane resolution can be calculated using weights proportional to the number of J/ψ signals obtained in narrower centrality bins as done in [77] for $2.5 < y < 4$. Since the statistic is limited in the analysis of J/$\psi \to \text{e}^+\text{e}^-$ at $|y| < 0.8$, such a weighting is not possible. To first order the J/ψ dN/dy depends linearly on N_{coll}: dN/d$y \sim w(\mathscr{C}) = N_{\text{coll}}(\mathscr{C}) \cdot 4.52 \times 10^{-5}$. Accordingly, the event plane resolutions obtained for 5%-wide centrality intervals (see Sec. 4.2.2) have been weighted to obtain the averaged values:

$$R_2 = \frac{\sum_{\mathscr{C}} R_2^{raw} \cdot w(\mathscr{C})}{\sum_{\mathscr{C}} w(\mathscr{C})}\tag{6.2}$$

It is observed that the event plane resolution with and without weight differ by only 1% (TPC) and 3% (V0A) in the centrality interval $10 - 50\%$.

Fig. 6.2 shows the signal extraction via the mixed-event technique in two $\Delta\phi$ bins based on Ψ_2^{TPC} and for the p_{T} range from 2 to 6 GeV/c. In both $\Delta\phi$ bins the significance ($S/\sqrt{S+B}$) is larger than 5σ. Within the statistical uncertainties the J/ψ signal counts are the same and thus according to Eq. (6.1) an J/ψ $v_2 = -0.027 \pm 0.110$ is observed, which is consistent with zero. A J/ψ $v_2 = -0.103 \pm 0.137$ consistent with zero within one sigma is also observed for V0A as event plane estimator, which has a worse Ψ_2 resolution.
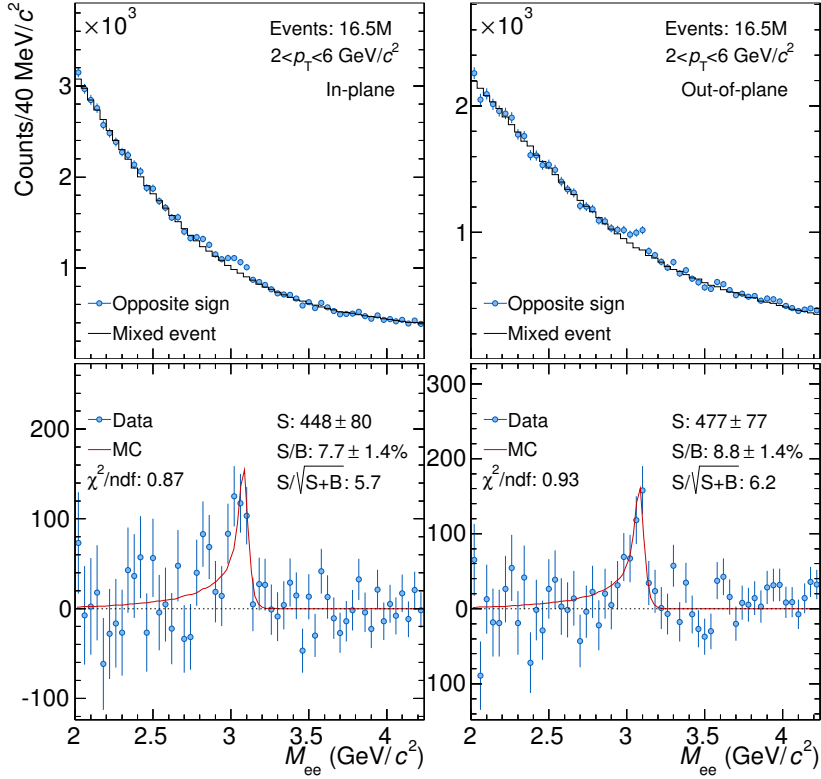
Figure 6.2.: Invariant mass distributions and J/ψ signal extractions in- and out-of-plane (Ψ_2^{TPC}) for $10 - 50\%$ most central events.

6.1.2. Fitting Approach

Similar to the $\langle p_{\mathrm{T}} \rangle$-signal extraction (see Sec. 5.2) and invented in [157], a combined fit making use of the signal-to-background ratio can be applied to the invariant mass spectrum of the observed flow $v_2^{S+B} = \langle \cos(2\Delta\phi) \rangle$. The functional form is given by Eq. (6.3), where the only free parameter is the J/ψ v_2.

$$v_2^{S+B} = \frac{S \cdot v_2^{\mathrm{J}/\psi} + B \cdot v_2^B}{S + B} \tag{6.3}$$

The background $B(m_{\mathrm{inv}})$ and its flow $v_2^B(m_{\mathrm{inv}})$ are obtained from mixed events which provides a good matching to the same event distribution down to $m_{\mathrm{inv}} = 200$ MeV/c^2 (see App. C). The signal $S(m_{\mathrm{inv}})$ corresponds to the background subtracted invariant mass distribution described in Sec. 4.3.3. This method is less statistics hungry compared to the $\Delta\phi$ technique, since the signal is extracted for the full azimuthal angle. Fig. 6.3 illustrates the fit to the invariant mass distribution of v_2 for different event plane detectors. Both fits

give consistent results of J/ψ $v_2 = 0.035 \pm 0.069$, that is compatible with the $\Delta\phi$-method, but has a smaller uncertainty.
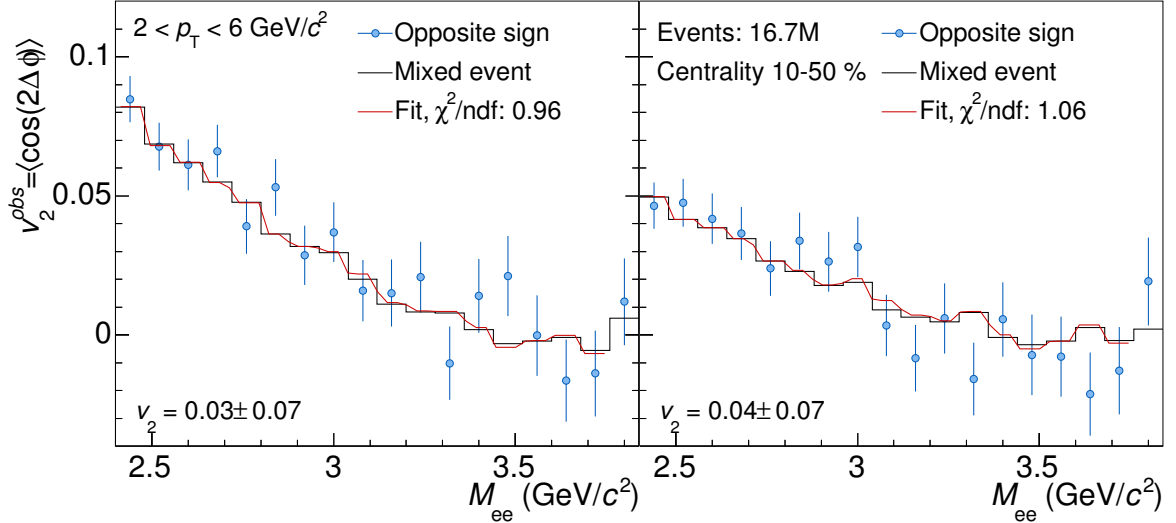

Figure 6.3.: Fitted invariant mass distributions of the observed v_2 for the event plane detector TPC (left) and V0C (right).

6.2. Estimation for Data Taking in Run2

Due to the large statistical uncertainty of the flow signal an analysis including all systematic checks has not been performed. However, based on the result of the $\Delta\phi$-method, an estimation on the needed statistic for a reasonable J/ψ v_2 measurement is done. The goal is to obtain a v_2 result with an absolute statistical uncertainty $\Delta v_2 = 0.04$ similar to one published by ALICE [77] for the forward rapidity interval or half of it $\Delta v_2 = 0.02$. For future v_2 analyses the following assumptions are made:

- The expected efficiency of the J/ψ measurement will improve by a 1.2, due to a better control of the TPC PID in run 2 that allows for a looser electron selection: $-1 < n\sigma_e < +3 \rightarrow -2 < n\sigma_e < +3$. In addition, the improved TPC performance should further increase the signal-to-background ratio by $\approx 10\%$.

- Furthermore, the SPD acceptance will increase from $\langle\epsilon\rangle = 61\%$ to $\approx 100\%$ resulting in an improved signal-to-background ratio (S/B) by a factor 1.5, due to the better rejection of secondary particles. However, according to Fig. 4.21 in Sec. 4.4.2, the efficiency drops by about the same factor when the ITS requirement is restricted

to a hit in the first SPD layer. In total, no or only a slight change is therefore expected.

- The measured J/ψ v_2 at mid-rapidity should be larger than zero. The estimation is done based on the predictions made in [67] using the kinetic transport model approach. According to the model the expected prompt J/ψ elliptic flow at mid-rapidity ($|y| < 2.4$) for minimum bias Pb-Pb collisions at $\sqrt{s_{\mathrm{NN}}} = 2.76$ TeV and J/ψ $p_{\mathrm{T}} = 2.9$ GeV/c is $v_2 = 0.071$. Fig. 6.5 shows the model prediction and the importance of the recombination component for the evolution of such a prominent J/ψ anisotropy. The quoted transverse momentum corresponds to the $\langle p_{\mathrm{T}} \rangle$ for the p_{T}-interval $2 < p_{\mathrm{T}} < 6$ GeV/c, that is evaluated based on the method described in Sec. 5.2 and shown in Fig. 6.4.

The calculation relies on existing data, and is based on the raw yield S, signal-to-background ratio S/B and integrated luminosity $\mathscr{L}_{int}$ of the ϕ-integrated signal extraction shown in Fig. 6.4.
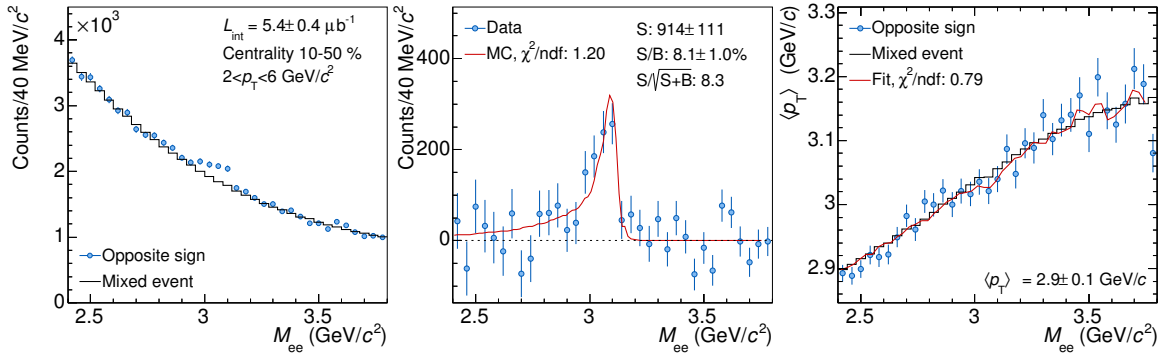

Figure 6.4.: J/ψ signal extraction with (left) and without background (center) and $\langle p_{\mathrm{T}} \rangle$ extraction (right) for the ϕ-integrated invariant mass spectrum in the centrality range $10 - 50\%$ and for $2 < p_{\mathrm{T}} < 6$ GeV/c.

According to Eq. (6.1), the statistical uncertainty of a predefined v_2 is then:

$$\Delta v_2 = \frac{1}{R_2} \frac{\pi}{4} \sqrt{\left(\frac{2 S_{\mathrm{out}}}{S (\mathscr{L}_{int})^2} \right)^2 (\Delta S_{\mathrm{in}})^2 + \left(\frac{2 S_{\mathrm{in}}}{S (\mathscr{L}_{int})^2} \right)^2 (\Delta S_{\mathrm{out}})^2}, \qquad (6.4)$$

with $S_{\mathrm{in}} = (2 v_2 / \pi + 1/2) S$ and $\Delta S = \sqrt{S(1 + B/S)}$.

Fig. 6.5 shows the expected statistical precision of v_2 compared to the published results by ALICE [77] in $2.5 < y < 4$ and the theoretical prediction [67] used for the estimate.

For such precise measurements the needed number of events and integrated luminosity is about $N_{\text{evt}} = 115.5 - 446.6 \times 10^6$ corresponding to $\mathscr{L}_{int} = 15 - 58$ µb^{-1}. In order to archive this, clearly a multiplicity trigger strategy needs to be followed also for the Pb-Pb data taking in run 2 with a focus on semi-central collisions.
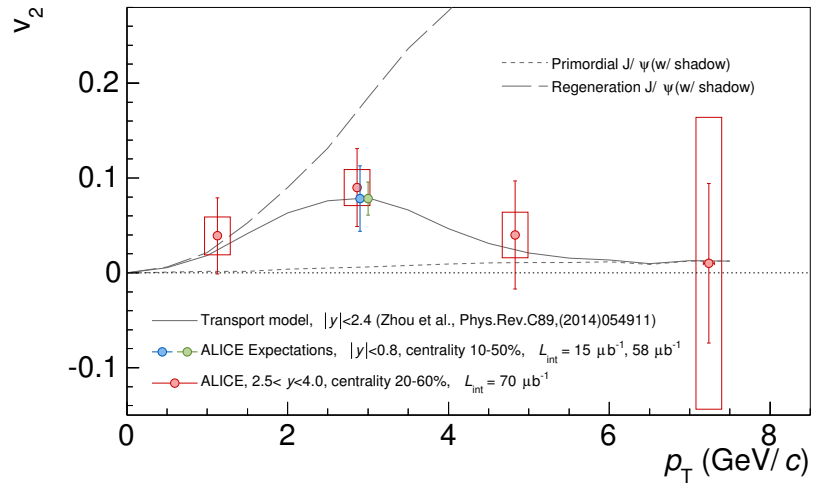

Figure 6.5.: The expected v_2 signal and statistical uncertainty for the two scenarios compared to model predictions and published results by ALICE in $2.5 < y < 4$.

Chapter 7.

Summary

The ALICE experiment is the dedicated general-purpose heavy-ion detector at the LHC. It was designed to explore the strongly-interacting matter created in ultra-relativistic heavy-ion collisions. ALICE is composed of several different detectors at forward and mid-rapidity in order to perform high precision measurements at very high track densities and down to low transverse momenta. Its unique selling proposition is the excellent particle identification capabilities at low transverse momentum. For this work the most important detectors are the Inner Tracking System and Time-Projection Chamber, that allow to the reconstruct the J/ψ particle via its decay into two electrons. Since the azimuthal coverage of the Transition Radiation Detector was not yet complete at the time of data taking, its electron-pion separation power has not been utilized. For future measurements its PID and trigger capabilities will improve the J/ψ measurements at mid-rapidity. Charmonia, and in particular the J/ψ, are ideal probes to study the Quark-Gluon Plasma due to their production in the very first stages of the collision. At the LHC, the production of charm and anti-charm quarks is sufficiently high to see the potential J/ψ production mechanism through c$\bar{\text{c}}$ coalescence, which can clearly be attributed to the existence of the QGP. In this thesis various observables for c$\bar{\text{c}}$ coalescence into J/ψ have been analyzed in order to understand the interplay of J/ψ dissociation and recombination in the formed medium.

In the presented work, we first have investigated the nuclear modification of J/ψ production with respect to nucleon-nucleon interactions. Clearly less J/ψ suppression for the most central nucleus-nucleus collisions is observed at LHC energies than in lower energy measurements. Furthermore, no strong centrality dependence of the R_{AA} for the 90% most central collisions has been found. Various transport model calculations, which include the c$\bar{\text{c}}$ recombination process, and the statistical hadronization model can qualitatively

describe the trend seen in data. However, the large uncertainties of the measurement and the ambiguity of the $c\bar{c}$ cross-section, which dominates the uncertainty in the model predictions, prevents to confirm or dismiss one of the models. Furthermore, results of the p_T-differential analysis have been obtained. An interpolation procedure based on mid-rapidity measurements by PHENIX, CDF and ALICE has been developed in order to calculate the p_T-dependent pp baseline, since there is no p_T-differential measurement in pp collisions at the energy under study. The result shows a decreasing trend of the R_{AA} from low towards high J/ψ transverse momenta and connects reasonable to the mid-rapidity result reported by the CMS collaboration. Significantly less suppression at low p_T was also observed in the R_{AA} measurement at forward rapidity done by ALICE. It can be interpreted as following: According to transport model predictions, less J/ψ suppression is expected at low p_T due to the smaller momentum differences of the charm quarks which is a favourable condition for J/ψ formation through the recombination mechanism. Therefore the observation of a larger R_{AA} at low J/ψ p_T can be seen as a indication for recombination. Furthermore, the transverse momentum behaviour of the R_{AA} found in this analysis is clearly different to the results at lower $\sqrt{s_{NN}}$ as reported by PHENIX and STAR collaborations, where the charm quark density is expected to be approximately 10 times smaller.

In the second part of this dissertation, the properties of transverse momentum distribution of J/ψ production were studied in more detail. The first and second moment of the distribution allows to disentangle different impacts on the J/ψ production that might occur in the formed medium. Since the collected Pb-Pb statistics is too low to obtain the kinematic properties directly from the p_T-distribution, a different approach was followed. The $\langle p_T \rangle$ and $\langle p_T^2 \rangle$ have been determined by a fit to the invariant mass distribution of the $\langle p_T \rangle$ for all e$^+$ e$^-$-pairs. The $\langle p_T \rangle$ and $\langle p_T^2 \rangle$ values in Pb-Pb are smaller than the values in pp collisions obtained via the pp interpolation. Either the region of high J/ψ p_T is reduced or the J/ψ production at low p_T is enhanced in heavy-ion collisions at LHC energies. Furthermore, no significant system-size dependence of $\langle p_T \rangle$ and $\langle p_T^2 \rangle$ was observed, but the uncertainties on the measurement are rather large. The evolution of $\langle p_T \rangle$ and $\langle p_T^2 \rangle$ versus N_{part} can be described by transport models, which include recombination and dissociation processes. In addition, the observable $r_{AA} = \langle p_T^2 \rangle_{A\text{-}A} / \langle p_T^2 \rangle_{pp}$ was obtained for inclusive J/ψ production at $\sqrt{s_{NN}} = 2.76$ TeV and found to be significantly below unity. This is in contrast to the results from lower energies (SPS and RHIC), where the r_{AA} increases or stays constant at unity with increasing N_{part}. The data are in good agreement with the transport model calculations, but results obtained in this work are

systematically below the LHC predictions, which might point to a stronger contribution of $c\bar{c}$ coalescence in data compared to theory.

A feasibility study on the signal extraction of the elliptic flow was presented in the last part of the thesis. A strong non-zero J/ψ v_2 signal is probably the cleanest signature for recombination processes, since J/ψ created in hard processes are created isotropically and do not have any information about the geometry of the collision. Only very small $v_2 < 0.02$ can be assigned to the path length dependent energy loss, while J/ψ created from (thermalized) charm and anti-charm quarks will inherit their anisotropy. However, the measurement of elliptic flow is statistics intensive and therefore only a J/ψ v_2 consistent with zero and large uncertainties was found. Nevertheless, the statistical uncertainty of such a measurement was estimated for the run 2 Pb-Pb data taking conditions. Accordingly, a significant non-zero or zero v_2 should be identifiable with the expected improvements in the TPC performance and approximately a factor three more statistics.

Appendix A.

PID Post-Calibration

Gamma Conversion Tagging

Gamma conversion are reconstructed using their V^0 decay topology. Since these decays can be identified based on kinematical and geometrical selections without relying on PID information, their products can be used for quantification of the PID response of the TPC. The selection criteria are listed in Tab. A.1, where the aim of the pair cuts is to select the γ conversion and the track selections on the daughter electrons are foreseen in order to match the reconstruction properties of the J/ψ daughter electrons. The algorithm to tag V^0 candidates can run in two modes ("offline" and "on-the-fly"). For the selection of electrons close to the interaction point the "on-the-fly" mode is preferred. In order to reduce the contamination by heavier particles (p, K, etc.) a cut on the TOF β estimation is imposed.

TPC PID Calibration in MC

The TPC PID calibration parameter distributions for centroids and widths of the PID response obtained for the MC simulations LHC12a17g,h,i.

Cut group	Description	Criterion
V^0 cuts	pointing angle	$\cos(\theta_{\mathrm{point}}) > 0.9998$ $\rightarrow \theta_{\mathrm{point}} < 20$ mrad
	Armenteros kinematics	$p_{\mathrm{T}}^{\mathrm{Arm}} < 0.05$ GeV/c $\left|\alpha^{\mathrm{Arm}}\right| < 0.35$
	invariant mass	$m_{\mathrm{inv}} < 50$ MeV/c^2
	fit quality	$\gamma\chi^2/\mathrm{ndf} < 10$
	approach of daughters	$dca < 0.25$ cm
	radius of decay vertex	$3 < R < 90$ cm
	angle btw. $\vec{B}$ and plane of $\vec{p_{\mathrm{e}^+}}$ and $\vec{p_{\mathrm{e}^-}}$	$\Psi_{\mathrm{e}^+\mathrm{e}^-} < 50$ mrad
track cuts	transverse momentum	$p_{\mathrm{T}} > 50$ MeV/c
	pseudo-rapidity	$|\eta| < 0.9$
	impact parameter	$|dca_{\mathrm{xy}}| < 1.0$ cm $|dca_{\mathrm{z}}| < 3.0$ cm
	Kinks	no daughters
	reconstruction	TPC refit
	TPC tracking	$\chi^2/\mathrm{ndf} < 4.0$ cluster segments > 7 cluster per track > 70
	TOF PID	$\beta > 0.9$

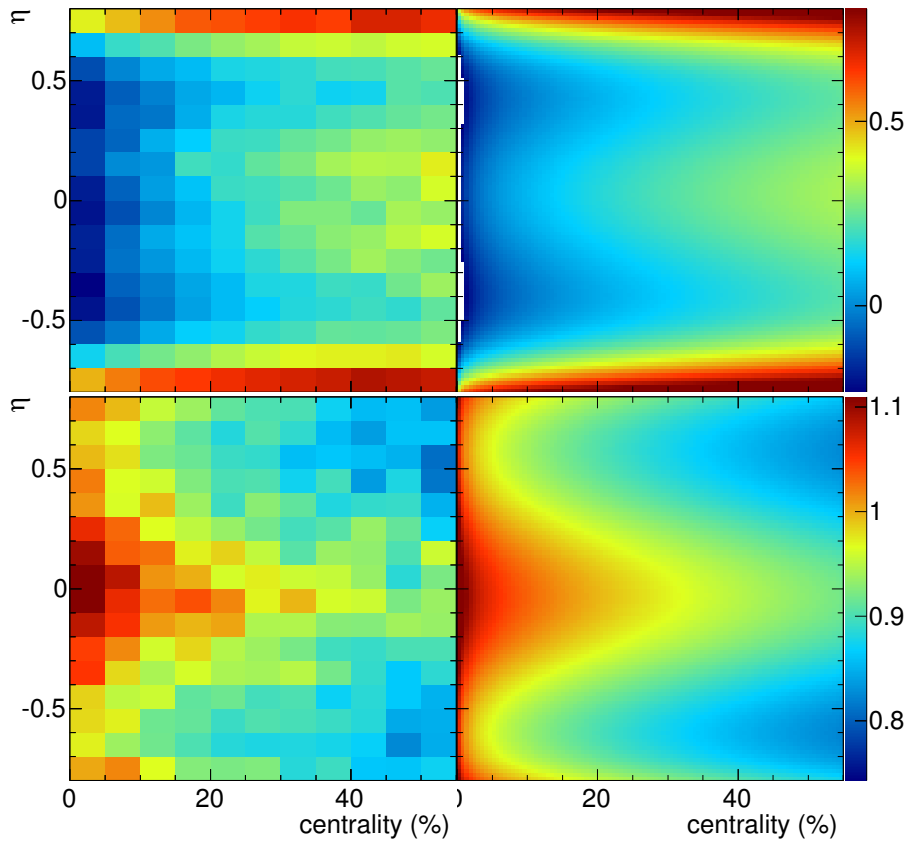**Table A.1.:** Track and pair selection criteria in post calibration.
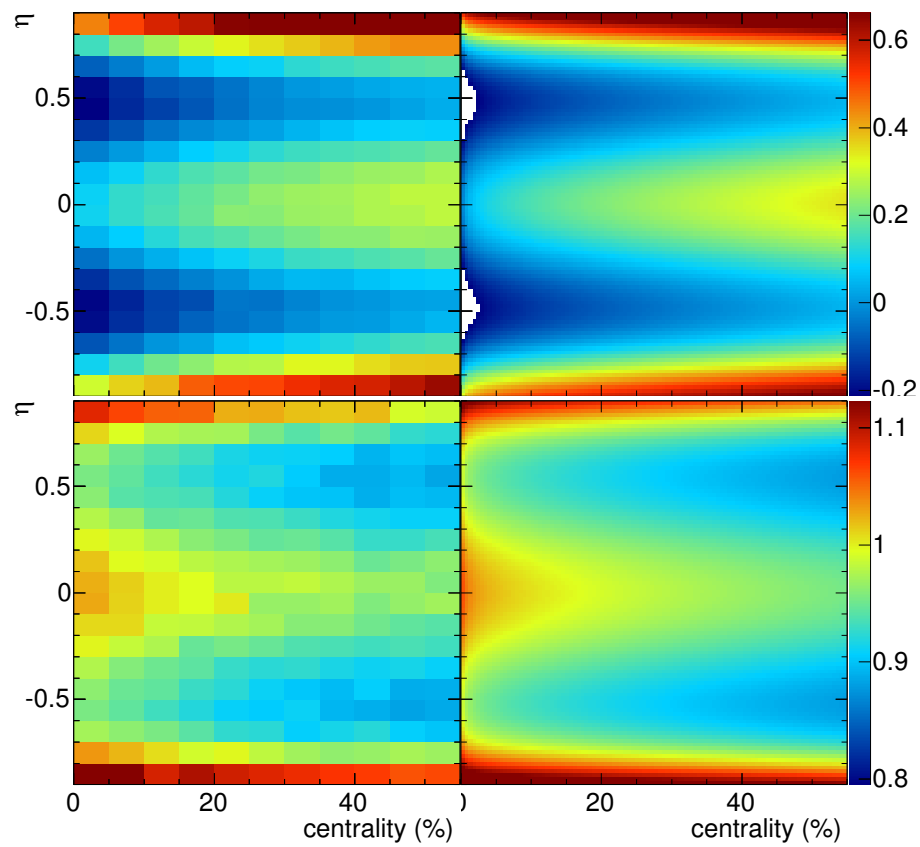
Figure A.1.: Left: The post calibration parameters, centroids (top) and widths (bottom), obtained via generalized double Gaussian fits. Right: The corresponding two-dimensional fits on the parameter distributions (left) for further smoothing.

Appendix B.

Analysis Details for the 2010 Data Sample

The measurement of the R_{AA}, $\langle p_{\mathrm{T}} \rangle$ and $\langle p_{\mathrm{T}}^2 \rangle$ in the peripheral centrality interval $40 - 90\%$ was performed based on the data taken end of 2010 with the minimum bias trigger. Due to the better quality of data in terms of TPC PID and ITS acceptance, looser selections are applied to the tracks (see Tab. B.1). Furthermore, the overall more stable running conditions compared to the 2011 data taking period allows to mix events from different runs without introducing a bias.

Cut group	Description	Criterion
acceptance	transverse momentum	$p_{\mathrm{T}} > 0.85$ GeV/c
	pseudo-rapidity	$|\eta| < 0.8$
reconstruction	impact parameter	$|dca_{\mathrm{xy}}| < 1.0$ cm
		$|dca_{\mathrm{z}}| < 3.0$ cm
	Kinks	no daughters
	reconstruction	ITS & TPC refit
	first hit in ITS	layer(ϕ) ≤ 3
		$\chi^2/\mathrm{ndf} < 4.0$
	TPC tracking	cluster per track > 70
PID	electron inclusion	$-2 <\mathrm{n}\sigma_{\mathrm{e}} < 3$
	proton exclusion	$\mathrm{n}\sigma_{\mathrm{p}} > 4$

Table B.1.: Track selection criteria for $40 - 90\%$.

In Fig. B.1, the TPC PID correction described in Sec. 4.3.2 is shown for LHC10h.

Figure B.1.: Left: The post calibration parameters, centroids (top) and widths (bottom), obtained via generalized double Gaussian fits. Right: The corresponding two-dimensional fits on the parameter distributions (left) for further smoothing.
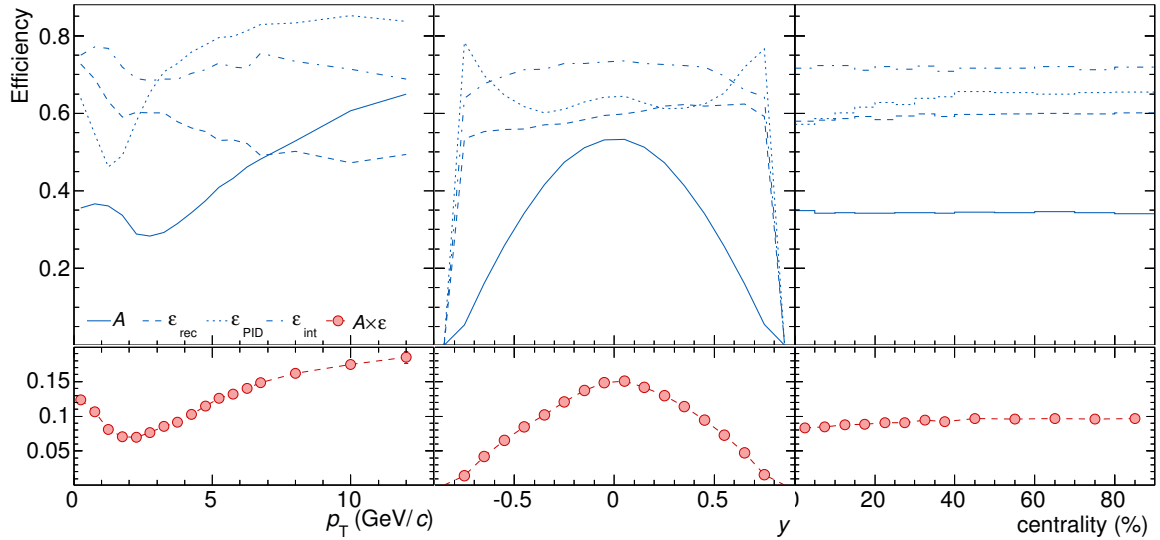
Figure B.2.: Partial J/ψ efficiencies versus transverse momentum, rapidity and collision centrality. The geometrical acceptance A (solid), reconstruction efficiency ϵ_{rec} (dashed), particle identification efficiency ϵ_{PID} (dotted) and the signal integration efficiency ϵ_{int} (dash dotted) as extracted from MC simulations (production: LHC11a10b-bis). Note: the efficiencies shown correspond to the decay of J/$\psi \rightarrow \mathrm{e}^{+}\mathrm{e}^{-}$ without the radiative component.

Appendix C.

Additional Figures
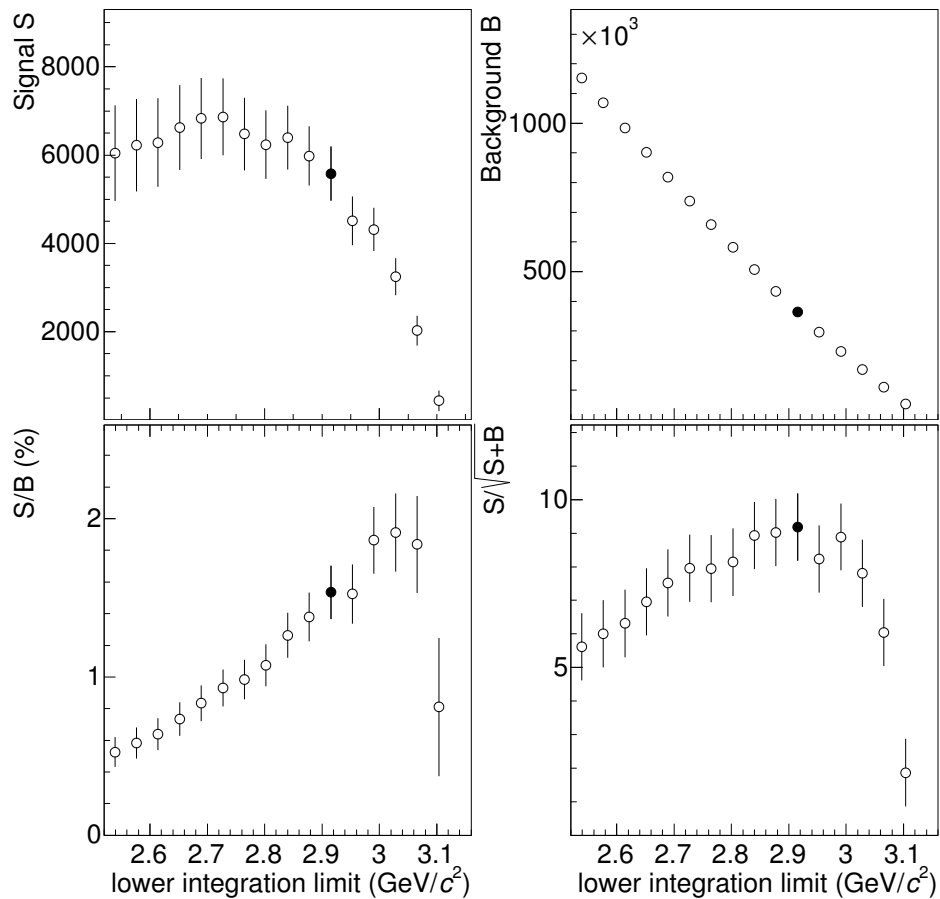
Figure C.1.: The signal S, background B, signal-to-background ratio S/B and significance $S/\sqrt{S+B}$ for signal extractions in the centrality interval $0-10\%$ are shown for variations of the lower integration limit by a fixed upper limit of $m_{\text{inv}} = 3.16$ GeV/c^2. The lower limit used in the analysis is indicated by the filled marker.
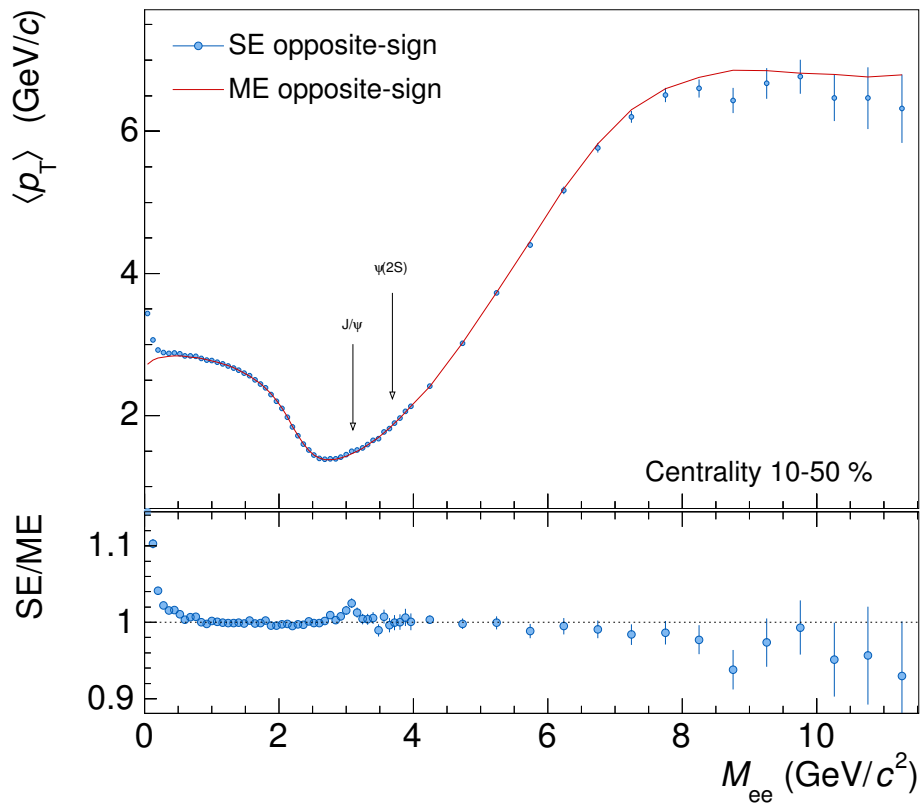
Figure C.2.: The uncorrected average transverse momentum versus m_{inv} for same and mixed events in the centrality interval $10 - 50\%$. The ratio SE/ME illustrates the background estimation quality over a broad m_{inv}-range.
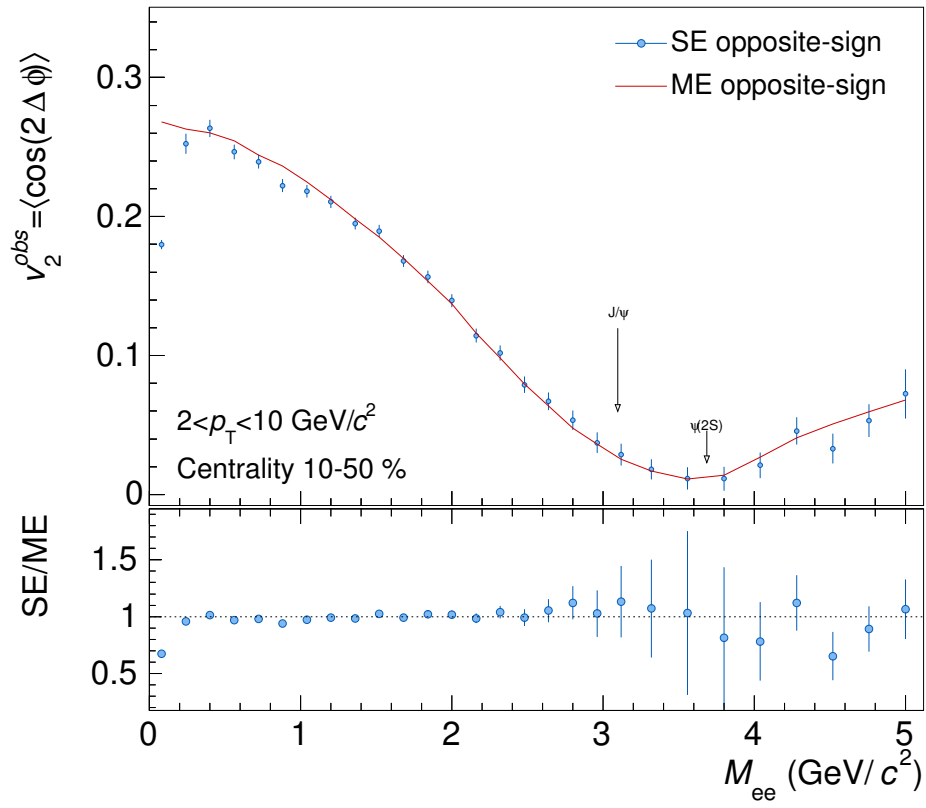
Figure C.3.: The observed v_2 versus m_{inv} for same and mixed events in the centrality interval $10 - 50\%$. The ratio SE/ME illustrates the background estimation quality.

Bibliography

[1] M. Breidenbach et al.: Observed Behavior of Highly Inelastic electron-Proton Scattering, Phys.Rev.Lett. **23** (1969) 935.

[2] E. D. Bloom et al.: High-Energy Inelastic e-p Scattering at 6 and 10, Phys. Rev. Lett. **23(16)** (1969) 930.

[3] J. Bjorken et al.: Inelastic Electron Proton and gamma Proton Scattering, and the Structure of the Nucleon, Phys.Rev. **185** (1969) 1975.

[4] M. Gell-Mann: A Schematic Model of Baryons and Mesons, Phys.Lett. **8** (1964) 214.

[5] G. Zweig: An SU$_3$ model for strong interaction symmetry and its breaking; Version 1, Technical Report CERN-TH-401, CERN, Geneva (1964).

[6] S. Drell et al.: Massive Lepton Pair Production in Hadron-Hadron Collisions at High-Energies, Phys.Rev.Lett. **25** (1970) 316.

[7] S. Borsanyi et al. (Wuppertal-Budapest Collaboration): Is there still any T_c mystery in lattice QCD? Results with physical masses in the continuum limit III, JHEP **1009** (2010) 073, arXiv:1005.3508.

[8] A. Bazavov et al.: The chiral and deconfinement aspects of the QCD transition, Phys.Rev. **D85** (2012) 054503, arXiv:1111.1710.

[9] J. C. Collins et al.: Superdense Matter: Neutrons or Asymptotically Free Quarks?, Phys. Rev. Lett. **34(21)** (1975) 1353.

[10] E. V. Shuryak: Quantum Chromodynamics and the Theory of Superdense Matter, Phys.Rept. **61** (1980) 71.

[11] J. Aubert et al. (E598 Collaboration): Experimental Observation of a Heavy Particle J, Phys.Rev.Lett. **33** (1974) 1404.

[12] J. Augustin et al. (SLAC-SP-017 Collaboration): Discovery of a Narrow Resonance in e+ e- Annihilation, Phys.Rev.Lett. **33** (1974) 1406.

[13] A. Boyarski et al.: The Quantum Numbers and Decay Widths of the psi (3095), Phys.Rev.Lett. **34** (1975) 1357.

[14] S. Glashow et al.: Weak Interactions with Lepton-Hadron Symmetry, Phys.Rev. **D2** (1970) 1285.

[15] S. Jacobs et al.: Comparing the Schrodinger and Spinless Salpeter Equations for Heavy Quark Bound States, Phys.Rev. **D33** (1986) 3338.

[16] H. Satz: Colour deconfinement and quarkonium binding, J.Phys. **G32** (2006) R25, arXiv:hep-ph/0512217.

[17] S. Okubo: Consequences of Quark Line (Okubo-Zweig-Iizuka) Rule, Phys.Rev. **D16** (1977) 2336.

[18] T. Armstrong et al. (Fermilab E760 Collaboration): Observation of the radiative decay $J/\psi \to e^+e^-\gamma$, Phys.Rev. **D54** (1996) 7067.

[19] A. Spiridonov: Bremsstrahlung in leptonic onia decays: Effects on mass spectra arXiv:hep-ex/0510076.

[20] J. Beringer et al. (Particle Data Group Collaboration): Review of Particle Physics (RPP), Phys.Rev. **D86** (2012) 010001.

[21] F. Arleo et al.: Charmonium suppression in p-A collisions, Phys. Rev. C **61(5)** (2000) 054906.

[22] G. Abrams et al.: The Decay of psi (3700) into psi (3100), Phys.Rev.Lett. **34** (1975) 1181.

[23] D. Kharzeev et al.: Color confinement in hadron - nucleus collisions, Z.Phys. **C60** (1993) 389.

[24] A. Martin et al.: Parton distributions for the LHC, Eur.Phys.J. **C63** (2009) 189, arXiv:0901.0002.

[25] P. Faccioli et al.: Study of ψ' and χ_c decays as feed-down sources of J/ψ hadro-production, JHEP **0810** (2008) 004, arXiv:0809.2153.

[26] B. Abelev et al. (ALICE Collaboration): Measurement of prompt J/ψ and beauty

hadron production cross sections at mid-rapidity in pp collisions at $\sqrt{s} = 7$ TeV, JHEP **1211** (2012) 065, arXiv:1205.5880.

[27] B. Alessandro et al. (ALICE Collaboration): ALICE: Physics performance report, volume II, J.Phys. **G32** (2006) 1295.

[28] J. Bjorken: Highly Relativistic Nucleus-Nucleus Collisions: The Central Rapidity Region, Phys.Rev. **D27** (1983) 140.

[29] T. Alber et al. (NA49 Collaboration): Transverse energy production in Pb-208 + Pb collisions at 158-GeV per nucleon, Phys.Rev.Lett. **75** (1995) 3814.

[30] S. Adler et al. (PHENIX Collaboration): Systematic studies of the centrality and $\sqrt{s_{\mathrm{NN}}}$ dependence of the $\mathrm{d}E_T/\mathrm{d}\eta$ and $\mathrm{d}N_{\mathrm{ch}}/\mathrm{d}\eta$ in heavy ion collisions at mid-rapidity, Phys.Rev. **C71** (2005) 034908, arXiv:nucl-ex/0409015.

[31] S. Chatrchyan et al. (CMS Collaboration): Measurement of the pseudorapidity and centrality dependence of the transverse energy density in Pb-Pb collisions at $\sqrt{s_{\mathrm{NN}}} = 2.76$ TeV, Phys.Rev.Lett. **109** (2012) 152303, arXiv:1205.2488.

[32] C. Alt et al. (NA49 Collaboration): Bose-Einstein correlations of pi-pi- pairs in central Pb+Pb collisions at A-20, A-30, A-40, A-80, and A-158 GeV, Phys.Rev. **C77** (2008) 064908, arXiv:0709.4507.

[33] B. Abelev et al. (STAR Collaboration): Pion Interferometry in Au+Au and Cu+Cu Collisions at RHIC, Phys.Rev. **C80** (2009) 024905, arXiv:0903.1296.

[34] K. Aamodt et al. (ALICE Collaboration): Two-pion Bose-Einstein correlations in central Pb-Pb collisions at $\sqrt{s_{\mathrm{NN}}} = 2.76$ TeV, Phys.Lett. **B696** (2011) 328, arXiv:1012.4035.

[35] P. Braun-Munzinger et al.: (Non)thermal aspects of charmonium production and a new look at J/ψ suppression, Phys.Lett. **B490** (2000) 196, arXiv:nucl-th/0007059.

[36] L. Adamczyk et al. (STAR Collaboration): Observation of D^0 meson nuclear modifications in Au+Au collisions at $\sqrt{s_{\mathrm{NN}}} = 200$ GeV, Phys.Rev.Lett. **113** (2014) 142301, arXiv:1404.6185.

[37] B. Abelev et al. (ALICE Collaboration): J/ψ Production as a Function of Charged Particle Multiplicity in pp Collisions at $\sqrt{s} = 7$ TeV, Phys.Lett. **B712** (2012) 165, arXiv:1202.2816.

[38] F. Kramer: J/ψ Production in $\sqrt{s} = 7$ TeV pp Collisions, Ph.D. thesis, Goethe University Frankfurt, Frankfurt am Main (2012).

[39] T. Sjostrand et al.: A Multiple Interaction Model for the Event Structure in Hadron Collisions, Phys.Rev. **D36** (1987) 2019.

[40] C. Kom et al.: Pair Production of J/ψ as a Probe of Double Parton Scattering at LHCb, Phys.Rev.Lett. **107** (2011) 082002, arXiv:1105.4186.

[41] V. Khachatryan et al. (CMS Collaboration): Measurement of prompt J/ψ pair production in pp collisions at $\sqrt{s} = 7$ Tev, JHEP **1409** (2014) 094, arXiv:1406.0484.

[42] V. M. Abazov et al. (D0 Collaboration): Observation and studies of double J/ψ production at the Tevatron arXiv:1406.2380.

[43] M. Strikman: Transverse Nucleon Structure and Multiparton Interactions, Acta Phys.Polon. **B42** (2011) 2607, arXiv:1112.3834.

[44] L. Frankfurt et al.: Transverse nucleon structure and diagnostics of hard parton-parton processes at LHC, Phys.Rev. **D83** (2011) 054012, arXiv:1009.2559.

[45] E. Ferreiro et al.: High multiplicity pp events and J/ψ production at LHC, Phys.Rev. **C86** (2012) 034903, arXiv:1203.5936.

[46] J. Cronin et al.: Production of Hadrons with Large Transverse Momentum at 200 GeV, 300 GeV, and 400 GeV, Phys.Rev. **D11** (1975) 3105.

[47] J. Hufner et al.: Gluon Multiple Scattering and the Transverse Momentum Dependence of J/ψ Production in Nucleus Nucleus Collisions, Phys.Lett. **B215** (1988) 218.

[48] N. Brambilla et al.: Heavy quarkonium: progress, puzzles, and opportunities, Eur.Phys.J. **C71** (2011) 1534, arXiv:1010.5827.

[49] K. Eskola et al.: EPS09: A New Generation of NLO and LO Nuclear Parton Distribution Functions, JHEP **0904** (2009) 065, arXiv:0902.4154.

[50] H. De Vries et al.: Nuclear charge and magnetization density distribution parameters from elastic electron scattering, Atom.Data Nucl.Data Tabl. **36** (1987) 495.

[51] M. L. Miller et al.: Glauber modeling in high energy nuclear collisions, Ann.Rev.Nucl.Part.Sci. **57** (2007) 205, arXiv:nucl-ex/0701025.

[52] N. Armesto et al.: Charmonium suppression in lead-lead collisions: Is there a break in the J/ψ cross-section?, Phys.Rev. **C59** (1999) 395, arXiv:hep-ph/9807258.

[53] J. Huefner et al.: Time structure of anomalous J/ψ and psi-prime suppression in nuclear collisions, Phys.Lett. **B559** (2003) 193, arXiv:nucl-th/0208004.

[54] T. Lang et al.: Possibility for J/ψ suppression in high multiplicity proton-proton collisions at $\sqrt{s} = 7$ TeV, Phys.Rev. **C87(2)** (2013) 024907, arXiv:1302.0655.

[55] T. Matsui et al.: J/ψ Suppression by Quark-Gluon Plasma Formation, Phys.Lett. **B178** (1986) 416.

[56] E. Eichten et al.: Charmonium: The Model, Phys.Rev. **D17** (1978) 3090.

[57] F. Karsch et al.: Color Screening and Deconfinement for Bound States of Heavy Quarks, Z.Phys. **C37** (1988) 617.

[58] A. Mocsy et al.: Color screening melts quarkonium, Phys.Rev.Lett. **99** (2007) 211602, arXiv:0706.2183.

[59] M. Asakawa et al.: J/ψ and eta(c) in the deconfined plasma from lattice QCD, Phys.Rev.Lett. **92** (2004) 012001, arXiv:hep-lat/0308034.

[60] A. Adare et al. (PHENIX Collaboration): Measurement of Υ(1S+2S+3S) production in $p+p$ and Au+Au collisions at $\sqrt{s_{\mathrm{NN}}} = 200$ GeV arXiv:1404.2246.

[61] D. Kharzeev et al.: The Transverse momentum dependence of anomalous J/ψ suppression, Phys.Lett. **B405** (1997) 14, arXiv:hep-ph/9702273.

[62] R. L. Thews et al.: Enhanced J/ψ production in deconfined quark matter, Phys.Rev. **C63** (2001) 054905, arXiv:hep-ph/0007323.

[63] M. Floris: Hadron yields and the phase diagram of strongly interacting matter arXiv:1408.6403.

[64] H. Satz: Quarkonium Binding and Dissociation: The Spectral Analysis of the QGP, Nucl.Phys. **A783** (2007) 249, arXiv:hep-ph/0609197.

[65] R. Thews et al.: Momentum spectra of charmonium produced in a quark-gluon plasma, Phys.Rev. **C73** (2006) 014904, arXiv:nucl-th/0505055.

[66] Y. Liu et al.: J/ψ elliptic flow in relativistic heavy ion collisions, Nucl.Phys. **A834** (2010) 317C, arXiv:0910.0959.

[67] K. Zhou et al.: Medium Effects on Charmonium Production at ultrarelativistic energies available at the CERN Large Haron Collider, Phys.Rev. **C89** (2014) 054911, arXiv:1401.5845.

[68] S. Digal et al.: Charmonium Production and Corona Effect, Phys.Rev. **C85** (2012) 034906, arXiv:1111.4776.

[69] A. Andronic et al.: Statistical hadronization of heavy quarks in ultra-relativistic nucleus-nucleus collisions, Nucl.Phys. **A789** (2007) 334, arXiv:nucl-th/0611023.

[70] S. Afanasiev et al. (PHENIX Collaboration): Measurement of Direct Photons in Au+Au Collisions at $\sqrt{s_{NN}} = 200$ GeV, Phys.Rev.Lett. **109** (2012) 152302, arXiv:1205.5759.

[71] S. Chatrchyan et al. (CMS Collaboration): Study of W boson production in Pb-Pb and pp collisions at $\sqrt{s_{NN}} = 2.76$ TeV, Phys.Lett. **B715** (2012) 66, arXiv:1205.6334.

[72] (CMS Collaboration): Z boson production with the 2011 data in Pb-Pb collisions .

[73] B. Alessandro et al. (NA50 Collaboration): ψ' production in Pb-Pb collisions at 158 GeV/nucleon, Eur.Phys.J. **C49** (2007) 559, arXiv:nucl-ex/0612013.

[74] S. Chatrchyan et al. (CMS Collaboration): Indications of suppression of excited Υ states in Pb-Pb collisions at $\sqrt{s_{NN}} = 2.76$ TeV, Phys.Rev.Lett. **107** (2011) 052302, arXiv:1105.4894.

[75] S. Chatrchyan et al. (CMS Collaboration): Event activity dependence of Y(nS) production in $\sqrt{s_{NN}} =5.02$ TeV pPb and $\sqrt{s} =2.76$ TeV pp collisions, JHEP **1404** (2014) 103, arXiv:1312.6300.

[76] A. Adare et al. (PHENIX Collaboration): J/ψ suppression at forward rapidity in Au+Au collisions at $\sqrt{s_{NN}} = 200$ GeV, Phys.Rev. **C84** (2011) 054912, arXiv:1103.6269.

[77] E. Abbas et al. (ALICE Collaboration): J/ψ Elliptic Flow in Pb-Pb Collisions at $\sqrt{s_{NN}} = 2.76$ TeV, Phys.Rev.Lett. **111** (2013) 162301, arXiv:1303.5880.

[78] (CMS Collaboration): Measurement of the azimuthal anisotropy of prompt and non-prompt J/ψ in Pb-Pb collisions at $\sqrt{s_{NN}} = 2.76$ TeV .

[79] X. Zhao et al.: In-Medium Quarkonia at SPS, RHIC and LHC, Nucl.Phys. **A904-905** (2013) 611c, arXiv:1210.6583.

[80] L. Adamczyk et al. (STAR Collaboration): Measurement of J/ψ Azimuthal Anisotropy in Au+Au Collisions at $\sqrt{s_{\mathrm{NN}}}$ = 200 GeV, Phys.Rev.Lett. **111(5)** (2013) 052301, arXiv:1212.3304.

[81] F. Prino et al. (NA50 Collaboration): J/ψ azimuthal anisotropy relative to the reaction plane in Pb-Pb collisions at 158 GeV per nucleon, Eur.Phys.J. **C61** (2009) 853, arXiv:0906.5376.

[82] R. Arnaldi (NA60 Collaboration): J/ψ suppression in p-A and In In collisions, J.Phys. **G35** (2008) 104133.

[83] A. Adare et al. (PHENIX Collaboration): J/ψ Production in $\sqrt{s_{\mathrm{NN}}}$ = 200 GeV Cu+Cu Collisions, Phys.Rev.Lett. **101** (2008) 122301, arXiv:0801.0220.

[84] L. Evans et al.: LHC Machine, JINST **3** (2008) S08001.

[85] ALICE Collaboration: ALICE time projection chamber: Technical Design Report, Technical Design Report ALICE (2000).

[86] B. B. Abelev et al. (ALICE Collaboration): Performance of the ALICE Experiment at the CERN LHC, Int.J.Mod.Phys. **A29** (2014) 1430044, arXiv:1402.4476.

[87] B. Abelev et al. (ALICE Collaboration): Measurement of inelastic, single- and double-diffraction cross sections in proton–proton collisions at the LHC with ALICE, Eur.Phys.J. **C73** (2013) 2456, arXiv:1208.4968.

[88] B. B. Abelev et al. (ALICE Collaboration): Measurement of quarkonium production at forward rapidity in pp collisions at $\sqrt{s}$ = 7 TeV, Eur.Phys.J. **C74(8)** (2014) 2974, arXiv:1403.3648.

[89] van der Meer, S.: Calibration of the Effective Beam Height in the ISR, CERN-ISR-PO-68-31 .

[90] K. Aamodt et al. (ALICE Collaboration): The ALICE experiment at the CERN LHC, JINST **3** (2008) S08002.

[91] B. Abelev et al. (ALICE Collaboration): Technical Design Report for the Upgrade of the ALICE Inner Tracking System, J.Phys. **G41** (2014) 087002.

[92] B. Abelev et al. (ALICE Collaboration): Centrality determination of Pb-Pb collisions at $\sqrt{s_{\mathrm{NN}}}$ = 2.76 TeV with ALICE, Phys.Rev. **C88(4)** (2013) 044909, arXiv:1301.4361.

[93] ALICE Collaboration: The ALICE TPC, a large 3-dimensional tracking device with fast read-out for ultra-high multiplicity events, Technical Report ALICE-INT-2009-034V2 (2010), URL `https://edms.cern.ch/document/1049095/2`.

[94] P. Cortese (ALICE Collaboration): ALICE transition-radiation detector: Technical Design Report (**ALICE-TDR-9 ; CERN-LHCC-2001-021 ; LYCEN-2001-97**).

[95] R. Bailhache: Calibration of the ALICE Transition Radiation Detector and a study of Z0 and heavy quark production in pp collisions at the LHC, Ph.D. thesis, Darmstadt, Tech. U., Darmstadt (2008).

[96] J. Book: TRD Calibration Monitoring (2013), URL `http://www-alice.gsi.de/trd/trending/`.

[97] J. Book: TRD Reconstruction Monitoring (2014), URL `http://www-alice.gsi.de/trd/trendingQA/`.

[98] H. Beck et al.: TRD Performance Offline Monitoring (2014), URL `http://www-alice.gsi.de/trd/monitoring/`.

[99] ALICE dimuon forward spectrometer: Technical Design Report (**ALICE-TDR-5 ; CERN-LHCC-99-022**).

[100] P. Cortese (ALICE Collaboration): ALICE forward detectors: FMD, TO and VO : Technical Design Report (**ALICE-TDR-11 ; CERN-LHCC-2004-025**).

[101] R. Brun et al.: ROOT: An object oriented data analysis framework, Nucl.Instrum.Meth. **A389** (1997) 81.

[102] S. Bagnasco et al.: AliEn: ALICE Environment on the GRID, J.Phys.Conf.Ser. **119** (2008) 062012.

[103] I. Bird: Computing for the Large Hadron Collider, Ann.Rev.Nucl.Part.Sci. **61** (2011) 99.

[104] T. Sjostrand et al.: PYTHIA 6.4 Physics and Manual, JHEP **0605** (2006) 026, arXiv:hep-ph/0603175.

[105] T. Sjostrand et al.: A Brief Introduction to PYTHIA 8.1, Comput.Phys.Commun. **178** (2008) 852, arXiv:0710.3820.

[106] S. Roesler et al.: The Monte Carlo event generator DPMJET-III (2000), pp.

1033–1038, URL `http://inspirehep.net/record/538940?ln=de`.

[107] M. Gyulassy et al.: HIJING 1.0: A Monte Carlo program for parton and particle production in high-energy hadronic and nuclear collisions, Comput.Phys.Commun. **83** (1994) 307, arXiv:nucl-th/9502021.

[108] F. Ballarini et al.: Nuclear models in FLUKA: Present capabilities, open problems and future improvements, AIP Conf.Proc. **769** (2005) 1197.

[109] CERN Computing and Networkks Division: GEANT Detector Description and Simulation Tool, CERN Program Library Long Writeup W5013 (1993).

[110] S. Agostinelli et al.: Geant4a simulation toolkit, Nuclear Instruments and Methods in Physics Research Section A: Accelerators, Spectrometers, Detectors and Associated Equipment **506(3)** (2003) 250.

[111] ALICE Collaboration: The LEGO Train System, Technical Report ˜ (2014), URL `https://aliceinfo.cern.ch/Notes/node/342`.

[112] ALICE MonALISA: Run Condition Table (2009), URL `http://alimonitor.cern.ch/configuration/`.

[113] K. Aamodt et al. (ALICE Collaboration): Centrality dependence of the charged-particle multiplicity density at mid-rapidity in Pb-Pb collisions at $\sqrt{s_{\mathrm{NN}}} = 2.76$ TeV, Phys.Rev.Lett. **106** (2011) 032301, arXiv:1012.1657.

[114] S. Voloshin et al.: Flow study in relativistic nuclear collisions by Fourier expansion of Azimuthal particle distributions, Z.Phys. **C70** (1996) 665, arXiv:hep-ph/9407282.

[115] A. M. Poskanzer et al.: Methods for analyzing anisotropic flow in relativistic nuclear collisions, Phys.Rev. **C58** (1998) 1671, arXiv:nucl-ex/9805001.

[116] I. Selyuzhenkov et al.: Effects of non-uniform acceptance in anisotropic flow measurement, Phys.Rev. **C77** (2008) 034904, arXiv:0707.4672.

[117] J. Barrette et al. (E877 Collaboration): Proton and pion production relative to the reaction plane in Au + Au collisions at AGS energies, Phys.Rev. **C56** (1997) 3254, arXiv:nucl-ex/9707002.

[118] J.-Y. Ollitrault: On the measurement of azimuthal anisotropies in nucleus-nucleus collisions arXiv:nucl-ex/9711003.

[119] K. Aamodt et al. (ALICE Collaboration): Higher harmonic anisotropic flow

measurements of charged particles in Pb-Pb collisions at $\sqrt{s_{\mathrm{NN}}}$ =2.76 TeV, Phys.Rev.Lett. **107** (2011) 032301, arXiv:1105.3865.

[120] B. Abelev et al. (ALICE Collaboration): Suppression of high transverse momentum D mesons in central Pb-Pb collisions at $\sqrt{s_{\mathrm{NN}}} = 2.76$ TeV, JHEP **1209** (2012) 112, arXiv:1203.2160.

[121] S. Rosegger: Simulation and Calibration of the ALICE TPC including innovative Space Charge Calculations, Ph.D. thesis, Tech. Univ. Graz, Graz (2009), CERN-THESIS-2009-124.

[122] P. Crochet et al.: Investigation of background subtraction techniques for high mass dilepton physics, Nucl.Instrum.Meth. **A484** (2002) 564, arXiv:nucl-ex/0106008.

[123] D. Drijard et al.: Study of Event Mixing and Its Application to the Extraction of Resonance Signals, Nucl.Instrum.Meth. **A225** (1984) 367.

[124] J. Gaiser: Charmonium Spectroscopy From Radiative Decays of the J/ψ and ψ', Ph.D. thesis, Calif. Univ. Stanford, Stanford, CA (1982).

[125] D. Lange: The EvtGen particle decay simulation package, Nucl.Instrum.Meth. **A462** (2001) 152.

[126] E. Barberio et al.: PHOTOS: A Universal Monte Carlo for QED radiative corrections. Version 2.0, Comput.Phys.Commun. **79** (1994) 291.

[127] X.-N. Wang et al.: Gluon shadowing and jet quenching in A-A collisions at $\sqrt{s} = 200A$ GeV, Phys.Rev.Lett. **68** (1992) 1480.

[128] B. Abelev et al. (ALICE Collaboration): Inclusive J/ψ production in pp collisions at $\sqrt{s} = 2.76$ TeV, Phys.Lett. **B718** (2012) 295, arXiv:1203.3641.

[129] A. Adare et al. (PHENIX Collaboration): J/ψ production versus transverse momentum and rapidity in pp collisions at $\sqrt{s} = 200$ GeV, Phys.Rev.Lett. **98** (2007) 232002, arXiv:hep-ex/0611020.

[130] D. Acosta et al. (CDF Collaboration): Measurement of the J/ψ meson and $b-$hadron production cross sections in $p\bar{p}$ collisions at $\sqrt{s} = 1960$ GeV, Phys.Rev. **D71** (2005) 032001, arXiv:hep-ex/0412071.

[131] K. Aamodt et al. (ALICE Collaboration): Rapidity and transverse momentum dependence of inclusive J/ψ production in pp collisions at $\sqrt{s} = 7$ TeV, Phys.Lett.

B704 (2011) 442, arXiv:1105.0380.

[132] B. B. Abelev et al. (ALICE Collaboration): Centrality, rapidity and transverse momentum dependence of J/ψ suppression in Pb-Pb collisions at $\sqrt{s_{NN}}$ =2.76 TeV, Phys.Lett. **B734** (2014) 314, arXiv:1311.0214.

[133] R. Barlow: Systematic errors: Facts and fictions (2002) 134arXiv:hep-ex/0207026.

[134] K. Eskola et al.: The Scale dependent nuclear effects in parton distributions for practical applications, Eur.Phys.J. **C9** (1999) 61, arXiv:hep-ph/9807297.

[135] L. Adamczyk et al. (STAR Collaboration): J/ψ production at low p_T in Au+Au and Cu+Cu collisions at $\sqrt{s_{NN}}$ = 200 GeV at STAR, Phys.Rev. **C90** (2014) 024906, arXiv:1310.3563.

[136] (CMS Collaboration): J/ψ results from CMS in Pb-Pb collisions, with 150mub-1 data .

[137] A. Andronic et al.: The thermal model on the verge of the ultimate test: particle production in Pb-Pb collisions at the LHC, J.Phys. **G38** (2011) 124081, arXiv:1106.6321.

[138] Y. Liu et al.: J/ψ Transverse Momentum Distribution in High Energy Nuclear Collisions at RHIC, Phys.Lett. **B678** (2009) 72, arXiv:0901.2757.

[139] X. Zhao et al.: Medium Modifications and Production of Charmonia at LHC, Nucl.Phys. **A859** (2011) 114, arXiv:1102.2194.

[140] E. Ferreiro: Charmonium dissociation and recombination at LHC: Revisiting comovers, Phys.Lett. **B731** (2014) 57, arXiv:1210.3209.

[141] S. Chatrchyan et al. (CMS Collaboration): Event activity dependence of Y(nS) production in $\sqrt{s_{NN}}$ =5.02 TeV pPb and $\sqrt{s}$ =2.76 TeV pp collisions, JHEP **1404** (2014) 103, arXiv:1312.6300.

[142] F. Bossu et al.: Phenomenological interpolation of the inclusive J/ψ cross section to proton-proton collisions at 2.76 TeV and 5.5 TeV arXiv:1103.2394.

[143] A. Adare et al. (PHENIX Collaboration): Ground and excited charmonium state production in pp collisions at $\sqrt{s}$ = 200 GeV, Phys.Rev. **D85** (2012) 092004, arXiv:1105.1966.

[144] K. Aamodt et al. (ALICE Collaboration): Rapidity and transverse momentum

dependence of inclusive J/ψ production in pp collisions at $\sqrt{s} = 7$ TeV, Phys.Lett. **B704** (2011) 442, arXiv:1105.0380.

[145] V. Khachatryan et al. (CMS Collaboration): Prompt and non-prompt J/ψ production in pp collisions at $\sqrt{s} = 7$ TeV, Eur.Phys.J. **C71** (2011) 1575, arXiv:1011.4193.

[146] R. Aaij et al. (LHCb Collaboration): Measurement of J/ψ production in pp collisions at $\sqrt{s} = 2.76$ TeV, JHEP **1302** (2013) 041, arXiv:1212.1045.

[147] R. Aaij et al. (LHCb Collaboration): Measurement of J/ψ production in pp collisions at $\sqrt{s} = 7$ TeV, Eur.Phys.J. **C71** (2011) 1645, arXiv:1103.0423.

[148] R. Aaij et al. (LHCb Collaboration): Measurement of J/ψ polarization in pp collisions at $\sqrt{s} = 7$ TeV, Eur.Phys.J. **C73(11)** (2013) 2631, arXiv:1307.6379.

[149] R. Aaij et al. (LHCb Collaboration): Production of J/ψ and Υ mesons in pp collisions at $\sqrt{s} = 8$ TeV, JHEP **1306** (2013) 064, arXiv:1304.6977.

[150] B. Abelev et al. (ALICE Collaboration): J/ψ polarization in pp collisions at $\sqrt{s} = 7$ TeV, Phys.Rev.Lett. **108** (2012) 082001, arXiv:1111.1630.

[151] S. Chatrchyan et al. (CMS Collaboration): Measurement of the prompt J/ψ and ψ(2S) polarizations in pp collisions at $\sqrt{s} = 7$ TeV, Phys.Lett. **B727** (2013) 381, arXiv:1307.6070.

[152] J. Yoh et al.: Study of Scaling in Hadronic Production of Dimuons, Phys.Rev.Lett. **41** (1978) 684.

[153] L. Adamczyk et al. (STAR Collaboration): J/ψ production at high transverse momenta in pp and Au+Au collisions at $\sqrt{s_{\mathrm{NN}}} = 200$ GeV, Phys.Lett. **B722** (2013) 55, arXiv:1208.2736.

[154] S. Chatrchyan et al. (CMS Collaboration): Suppression of non-prompt J/ψ, prompt J/ψ, and Y(1S) in Pb-Pb collisions at $\sqrt{s_{\mathrm{NN}}} = 2.76$ TeV, JHEP **1205** (2012) 063, arXiv:1201.5069.

[155] Y. Liu et al.: Velocity dependence of charmonium dissociation temperature in high-energy nuclear collisions, Phys.Lett. **B724** (2013) 73, arXiv:1210.7449.

[156] M. Winn (ALICE Collaboration): Inclusive J/ψ and psi(2S) production in p-Pb collisions at $\sqrt{s_{\mathrm{NN}}} = 5.02$ TeV with ALICE at the LHC, Nucl.Phys. **A932** (2014) 472, arXiv:1404.1615.

[157] N. Borghini et al.: Azimuthally sensitive correlations in nucleus-nucleus collisions, Phys.Rev. **C70** (2004) 064905, arXiv:nucl-th/0407041.

[158] R. Arnaldi (ALICE Collaboration): J/ψ and Psi(2S) production in Pb-Pb collisions with the ALICE Muon Spectrometer at the LHC, Nucl.Phys. **A904-905** (2013) 595c, arXiv:1211.2578.

[159] M. Abreu et al. (NA50 Collaboration): Transverse momentum distributions of J/ψ, psi-prime, Drell-Yan and continuum dimuons produced in Pb Pb interactions at the SPS, Phys.Lett. **B499** (2001) 85.

[160] X. Zhao et al.: Charmonium in Medium: From Correlators to Experiment, Phys.Rev. **C82** (2010) 064905, arXiv:1008.5328.

[161] K. Zhou et al.: Quarkonium Production and Medium Effects in High Energy Nuclear Collisions arXiv:1309.7520.

Danksagung

Curriculum Vitae

Julian Book

Born: August 24, 1984
in Frankfurt am Main

EDUCATION

since 11/2009	Member of the Helmholtz Graduate School for Hadron and Ion Research (HGS-HIRe)
since 10/2009	Member of the Helmholtz Research School for Quark Matter Studies in Heavy Ion Collisions (H-QM)
since 10/2009	PhD student, Goethe-Universität Frankfurt am Main *Advisor:* Prof. Dr. Christoph Blume
2004 – 2009	Diploma in Physics, Goethe-Universität Frankfurt am Main *Advisor:* Prof. Dr. Christoph Blume *Thesis:* "Zentralitätsabhängigkeit der K_S^0-Produktion in relativistischen Schwerionenkollisionen"
1995 – 2004	University-entrance diploma (Abitur), Humboldtschule Bad Homburg v.d. Höhe

PUBLICATIONS

exp 2015	ALICE Collaboration, *target journal:* Physics Letters B "Inclusive, prompt and non-prompt J/ψ production at mid-rapidity in Pb-Pb collisions at $\sqrt{s_{\mathrm{NN}}} = 2.76$ TeV " ALICE Collaboration, *target journal:* Physics Letters B "Transverse momentum dependence of the inclusive J/ψ nuclear modification factor in p-Pb collisions at the LHC"
2014	J.Book et al., Nuclear Physics A, Special Issue, *In Press* "J/ψ Production in Pb-Pb Collisions at $\sqrt{s_{\mathrm{NN}}} = 2.76$ TeV " ALICE Collaboration, Physics Letters B734, 314-327, (2014) "Centrality, rapidity and transverse momentum dependence of J/ψ suppression in Pb-Pb collisions at $\sqrt{s_{\mathrm{NN}}} = 2.76$ TeV "

2012   J.Book et al., 2012 J. Phys.: Conf. Ser. 389 012028 "J/ψ Measurements with the ALICE Experiment at the LHC"

2010   J.Book et al., GSI Scientific Report 2009, 249, (2010) "Perspectives of J/$\psi \rightarrow$ e$^+$e$^-$ measurement in pp collisions at the LHC in ALICE"

                J.Book et al., GSI Scientific Report 2009, 250, (2010) "Development of Analysis Methods for J/$\psi \rightarrow$ e$^+$e$^-$ with the ALICE central barrel detectors"

                J.Book et al., GSI Scientific Report 2009, 342, (2010) "Calibration of the ALICE Transition Radiation Detector with the First Proton Beam Data"

                J.Book et al., GSI Scientific Report 2009 "Centrality dependence of K$_S^0$ production in Pb-Pb collisions at the CERN SPS"

PRESENTATIONS

05/2014   Quark Matter Conference 2014, Darmstadt,
                "J/ψ Production in Pb-Pb Collisions at $\sqrt{s_{\mathrm{NN}}} = 2.76$ TeV "

03/2014   DPG Frühjahrstagung 2014, Frankfurt,
                "J/ψ Production in Pb-Pb Collisions at $\sqrt{s_{\mathrm{NN}}} = 2.76$ TeV "

03/2013   DPG Frühjahrstagung 2013, Dresden,
                "Elliptic Flow of J/ψ in Pb-Pb Collisions at $\sqrt{s_{\mathrm{NN}}} = 2.76$ TeV with the ALICE Experiment"

04/2012   Winter Workshop on Nuclear Dynamics, Dorado del Mar, Puerto Rico,
                "J/ψ Measurements with the ALICE Experiment at the LHC"

03/2012   DPG Frühjahrstagung 2012, Mainz,
                "J/ψ Production as a Function of Charged Particle Multiplicity in pp Collisions at $\sqrt{s} = 7$ TeV "

12/2009   IKF-Seminar, Frankfurt,
                "Centrality Dependence of K$_S^0$ Production in Relativistic Heavy Ion Collisions at the CERN Super Proton Synchrotron"

03/2009   DPG Frühjahrstagung 2009, Bochum,
                "Centrality Dependence of K$_S^0$ Production in Pb-Pb Collisions"